FLOW BOILING OF WATER IN PIN-FIN ENHANCED MICROGAP

A Dissertation
Presented to
The Academic Faculty

by

Xuefei Han

In Partial Fulfillment
of the Requirements for the Degree
Doctor of Philosophy in the
George W. Woodruff School of Mechanical Engineering

Georgia Institute of Technology
May 2017

FLOW BOILING OF WATER IN PIN-FIN ENHANCED MICROGAP

Approved by:

Dr. Yogendra Joshi, Advisor
School of Mechanical Engineering
Georgia Institute of Technology

Dr. Peter A. Kottke
School of Mechanical Engineering
Georgia Institute of Technology

Dr. Cyrus K. Aidun, Co-Advisor
School of Mechanical Engineering
Georgia Institute of Technology

Dr. Muhannad S Bakir
School of Electrical and Computer Engineering
Georgia Institute of Technology

Dr. Andrei G. Fedorov
School of Mechanical Engineering
Georgia Institute of Technology

Date Approved: Jan. 05, 2017

ACKNOWLEDGEMENTS

I would like to express my sincere gratitude to my advisor Prof. Yogendra Joshi for his insightful guidance and generous support to my studies. His understanding, patience and advice always helped me. I would also like to express my deepest appreciation to my co-advisor Prof. Cyrus Aidun, who always sent me feedbacks and valuable advices on my work. I would also like to thank all my other dissertation committee members, Prof. Andrei Fedorov, Prof. Muhannad S Bakir and Dr. Peter Kottke, for their comments on my research. I am really thankful to Xuchen Zhang, who fabricated test samples for me so I am able to fulfil my research work. I am grateful to my current and previous colleagues in the Microelectronic and Emerging Technologies Thermal Laboratory (METTL) for their help. I also deeply acknowledge my parents, my husband and my son for their support and understanding.

Table of Contents

LIST OF TABLES

LIST OF FIGURES

LIST OF SYMBOLS AND ABBREVIATIONS

$A_{b,sp}$	Single phase region base area, m^2
$A_{b,tp}$	Two phase region base area, m^2
A_c	Single pin fin cross-section area, m^2
$A_{c,min}$	Minimum channel cross-section area, m^2
A_f	Single pin fin surface area, m^2
A_h	Total heated area, m^2
$A_{h,sp}$	Single phase heated area, m^2
$A_{h,tp}$	Two phase heated area, m^2
C	Empirical constant in two phase multiplier
C_p	Specific heat capacity, J/kg·K
D	Pin diameter, m
F	Two phase heat transfer coefficient correlation parameter
f	Friction factor
$f_{sp,i}$	Friction factor

G	Mass flux, kg/m^2·s
G_{max}	Maximum mass flux, kg/m^2·s
H_g	Microgap height, m
H_f	Fin height, m
h	Heat transfer coefficient, W/m^2·K
h_{avg}	Average heat transfer coefficient, W/m^2·K
h_{sp}	Local single phase heat transfer coefficient, W/m^2·K
h_{tp}	Local two phase heat transfer coefficient, W/m^2·K
I	Current, A
k_{Si}	Thermal conductivity of silicon, W/m·K
k_{SiO_2}	Thermal conductivity of silicon dioxide, W/m·K
M	Total number of data points
MAE	Mean absolute error
m	Fin efficiency parameter
$\dot{m}$	Mass flow rate, kg/s
N_{sp}	Total number of pins in single phase region

N_t	Total row number of pins
N_{tot}	Total number of pin fins
N_{tp}	Total number of pins in two phase region
N_{tr}	Row number of pins where single phase region transitions to two phase region
Nu_{sp}	Single phase Nusselt number
P_f	Pin fin perimeter, m
P_{in}	Inlet pressure, kPa
P_{out}	Outlet pressure, kPa
Pr	Prandtl number
P_{sat}	Saturation pressure, kPa
P_{total}	Total power, W
$P_{tp,0}$	Pressure at where single phase region transitions to two phase region, kPa
Q_{loss}	Heat loss, W
$q_{eff}"$	Effective heat flux, W/cm^2
R_{heater}	Heater resistance, Ω
Re	Reynolds number

RTDs	Resistance temperature detectors
S_T	Transverse pitch, m
S_L	Longitudinal pitch, m
T	Temperature, ℃
T_f	Fluid temperature, ℃
T_h	Heater temperature, ℃
T_{heater}	Heater temperature, ℃
T_{in}	Inlet fluid temperature, ℃
T_{max}	Maximum wall temperature, ℃
T_{sat}	Saturation temperature, ℃
$T_{sat,o}$	Saturation temperature evaluated at device outlet pressure, ℃
T_w	Wall temperature, ℃
t_{Si}	Heat sink base thickness, m
t_{SiO_2}	Silicon dioxide thickness, m
V	Voltage, V
VFR	Volume flow rate, mL/min

W_g	Microgap width, m
X	Martinelli parameter
X_{vv}	Martinelli parameter for viscous liquid phase and viscous vapor phase
x	Exit vapor quality

Greek symbols

α	Void fraction
α_H	Homogeneous void fraction
η_f	Fin efficiency
ΔP	Pressure drop, kPa
ΔP_{meas}	Experimentally measured pressure drop, kPa
ΔP_{pred}	Predicted pressure drop using correlations, kPa
ΔP_{sub}	Subcooled single phase liquid pressure drop, kPa
ΔP_{tp}	Two phase pressure drop, kPa
$\Delta P_{tp,a}$	Accelerational two phase pressure drop due to, kPa
$\Delta P_{tp,f}$	Frictional two phase pressure drop, kPa
ϕ_l^2	Two phase multiplier

ζ	Two phase heat transfer coefficient correlation parameter
λ	Two phase pressure drop correlation parameter
μ	Dynamic viscosity, kg/m-s
μ_l	Liquid phase dynamic viscosity, kg/m-s
μ_v	Vapor phase dynamic viscosity, kg/m-s
$\rho_{fluid,v}$	Fluid vapor phase density, kg/m-s
$\rho_{HFE7200,v}$	HFE-7200 vapor phase density, kg/m-s
$\rho_{water,v}$	Water vapor phase density, kg/m-s
ρ_l	Liquid phase density, kg/m^3
ρ_v	Vapor phase density, kg/m^3

SUMMARY

This study experimentally investigated flow boiling of water in a closed flow loop system at reduced pressure with a wide range of heat fluxes, mass fluxes, and inlet fluid temperatures. Two microgaps with the same height of 200 μm, one with sparse pin fins, and the other with dense pin fins, were studied and compared. The transverse and longitudinal pitches were both 400 μm for the microgap with sparse pin fins, and were both 200 μm for the one with dense pin fins. The pins were circular with a diameter of 150 μm for both microgaps. The pin fins were arranged in a staggered way, and covered an area of 1 cm × 1 cm. New two phase heat transfer and pressure drop correlations were proposed based on the current study. Two phase flow instabilities were observed under certain conditions and were discussed. High speed visualization was utilized to characterize two phase flow patterns. Effects of spatially non-uniform surface heating on two phase flow were studied. The heat transfer and pressure drop performance of dielectric liquid HFE-7200 was tested and compared with water. Two phase heat transfer coefficient and pressure drop correlations were also developed for HFE-7200.

CHAPTER 1. INTRODUCTION

Flow boiling in micro scale systems was studied intensively in the past two decades and is still attracting the interest of many researchers [1-5]. Possible improvement in heat transfer over single phase flow at the same mass flux, due to latent heat of vaporization makes it a promising thermal management method for high power dissipation electronics. Moreover, two phase flow may offer better temperature uniformity than single phase flow, if dryout and instabilities can be mitigated. A block diagram of a closed loop forced flow two phase microfluidic cooling system for electronic devices is shown in Figure 1. The system generally consists of a pump to drive fluid flow, microscale heat sink for heat removal from the chip via two-phase flow, heat exchanger to reject heat to the ambient and condense the vapor, and reservoir to supply sufficient fluid for circulation. Filters with micro scale pore size, and pressure regulating valves are also common components in these systems.

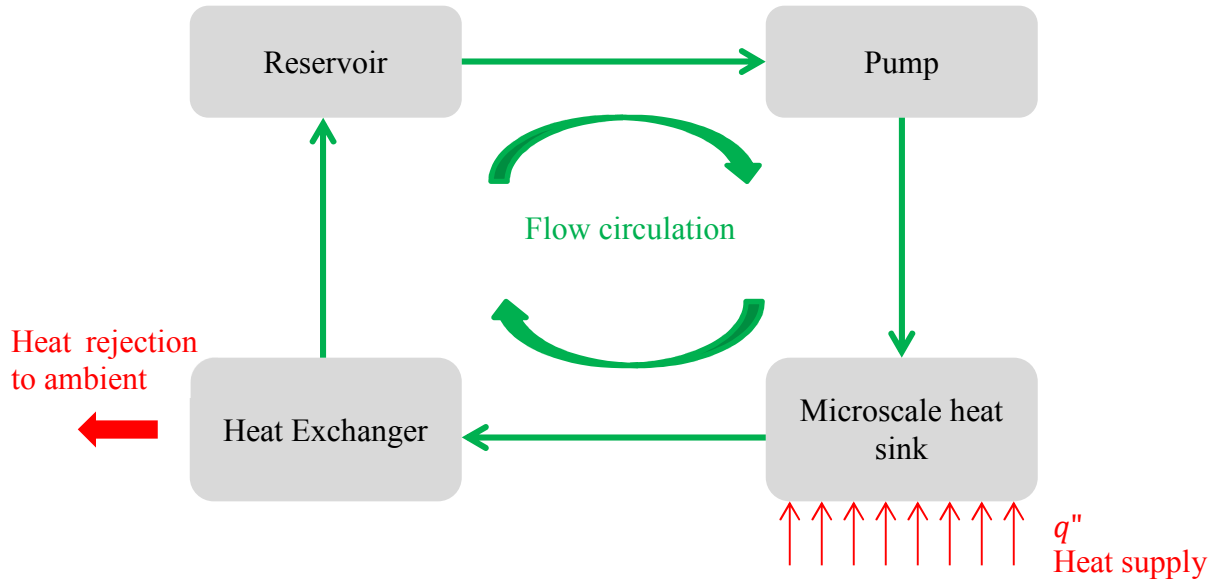

Figure 1 Schematic of closed loop microfluidic cooling system

Thermodynamic and transport properties of six typical coolants, FC-72, water, HFE-7200, R-123, R-134a and R-245fa, all of which have been frequently used for flow boiling experiments, are listed in Table 1. These properties are obtained from the software Engineering Equation Solver (Water, R-123, R-134a, R-245fa and FC-72) [6], and from their manufacturer 3M company (FC-72 and HFE-7200). Water is the most attractive coolant among these because of its good thermal conductivity, large specific heat and latent heat of vaporization, which enable absorption of considerable amount of heat during both sensible heating and boiling. However, saturation temperature of water at atmospheric pressure is 100 ℃, which may be unacceptably high for continuous operation of complementary metal oxide semiconductor (CMOS) electronic devices. Water is also not as chemically and electrically inert as other coolants in Table 1, but is the most environmentally friendly. The liquid to vapor density ratio of water is also the largest among the six coolants, which can result in very large void fraction at relatively low vapor quality. Void fraction is the fraction of the cross-sectional area of the channel that is occupied by the vapor, and quality is the vapor mass fraction. The high density ratio also results in relatively large accelerational pressure drop associated with convective boiling flow in microgeometries. The dynamic viscosity of water is in the middle range among these coolants, resulting in relatively small single phase pressure drop with smallest density compared to others.

Dielectric coolants, FC-72 and refrigerants, are of great interest because they are chemically and electrically inert, and have low saturation temperature at atmospheric pressure, making them more suitable for electronics cooling. Some refrigerants, such as R-134a need to operate at high saturation pressures at the temperatures relevant to operating electronics devices, adding extra structural strength requirement to the flow system. Some dielectric coolants

contribute to ozone depletion and global warming. Hydrofluoroethers (HFEs) are a better option due to their nearly zero stratospheric ozone depletion, and relatively low global warming potential [7]. HFEs (HFE-7200, for instance) also have lower boiling point compared to water.

Table 1 Sample flow boiling coolant thermodynamic and transport properties (FC-72, Water, HFE-7200 and R-123 properties evaluated at T_{sat}, R-134a and R-245fa properties evaluated at P_{sat})

	T_{sat} (°C) @ 1 atm	C_P (kJ/kg-K)	h_{vap} (kJ/kg)	ρ_l (kg/m3)	ρ_v (kg/m3)	k_l (W/m-K)	$\mu_l \cdot 10^3$ (kg/m-s)	P_{sat} (kPa) @ 25 °C
FC-72	56.3	1.141	83.41	1602	13.28	0.05384	0.351	30.2
Water	100	4.217	2257	958.4	0.5975	0.6651	0.2819	3.2
HFE-7200	76	1.306	113.0	1300.7	9.47	0.0614	0.345	35.24
R-123	27.8	1.039	170.6	1457	6.474	0.07649	0.4044	91.5
R-134a	-26.1	1.425	177.8	1207	32.37	0.08323	0.1944	665.8
R-245fa	15.19	1.322	190.3	1339	8.525	0.06703	0.2152	147.8

Reviews of flow boiling in microchannels (single microchannel and parallel microchannels) have been performed by Garimella and Sobhan [1], Thome [2], and recently by Tibirica et al. [3]. To compliment these works, a review of experimental work on flow boiling in plain and surface enhanced microgaps is presented in the following section. Representative

geometries are shown in Figure 2. The details of geometry, experimental conditions, and studied parameters in each reviewed paper are summarized in Table 2.

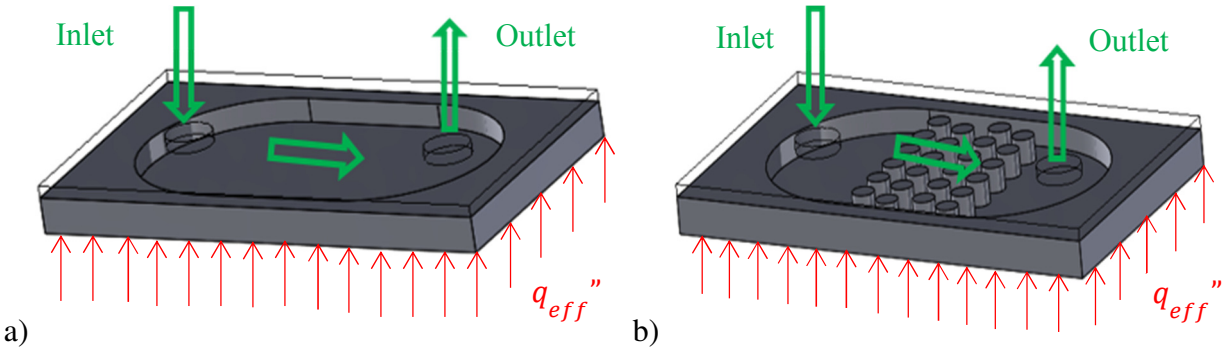

Figure 2 a) Plain microgap, b) microgap with pin fin surface enhancement

Table 2 Descriptions of flow boiling in microgap and microgap with surface enhancement

Author	Year	Geometry, Gap area, Gap height, Pin dimension (mm)	Fluid	Material	q'' (W/cm^2)	G (kg/m^2s)	P (kPa)	T_{in} (℃)	x	Studied parameters
Lee et al. [8]	2001	Minigap and microgap, 20x300, H = 2, 1, 0.4	R-113	Stainless steel	Up to 1.5	50 - 200	-	-	0.15 – 0.75	h_{tp}, ΔP, h_{tp} correlation
Yang et al. [9]	2004	Minigap and microgap, 20x100, H = 2, 1, 0.5, 0.2	R-113	Copper	0.2 - 9	20 - 500	118	-	-	Flow patterns, effects of gap height
Kosar et al. [10]	2006	Microgap with circular pin-fin, 1.8x10, staggered, H = 0.243, D = 99.5	R123	Silicon	3.5 – 65.5	351 - 887	-	-	-	Boiling inception, ΔP, boiling instabilities
Kosar et al. [11]	2007	Microgap with hydrofoil pin-fin, 1.8x10, staggered, H = 0.243	R-123	Silicon	19 - 312	976 - 2349	-	-	Up to 1	h_{tp}, CHF, flow pattern and flow map

Lie et al. [12]	2007	Microgap with square pin-fin, 20x150, H = 5, H_f = 0.07, S = 0.2, 0.1	FC-72	Silicon	0.1 - 10	287 - 431	101	-	-	h_{sp}, h_{tp}, bubble departure diameter and frequency
Krishnamurthy et al. [13]	2008	Microgap with circular pin-fin, staggered, 1.8x10, H = 0.25, , D = 0.1	D.I. water	Silicon	20 - 350	346 - 794	101	-	up to 0.17	h_{sp}, h_{tp}, h_{tp} correlation, flow regime map
Sheehan et al. [14]	2009	Microgap, 30x34, H = 0.26	FC - 72	copper	3.2	35	-	-		Wall temperature
Qu et al. [15]	2009	Microgap with square pin-fin, staggered, 10x33.8, H = 0.67, S = 0.2	D.I. water	Copper	23.7 – 248.5	183 – 420	103 – 108	30, 60, 90	up to 0.27	h_{tp} correlation
Ma et al. [16]	2009	Plain microgap and microgap with square pin-fin, W_{CH} = 30, H = 5, H_f = 0.06, 0.12, S = 0.03	FC-72	Silicon	Up to 150	0.5,1,2 m/s	-	T_{sub}= 15,25, 35	-	Boiling curve, CHF, effects of pin-fins and pin-fin heights
Yuan et al. [17]	2009	Plain microgap and microgap with square pin-fin, W_{CH} = 30, H = 5, S = 0.05, H_f = 0.06, 0.12	FC-72	Silicon	Up to 145	0.5, 1, 2m/s	101	T_{sub}= 15,25, 35	-	Boiling curve, CHF, effects of pin-fins and pin-fin heights

Kim et al. [18, 19]	2008, 2010	Microgap, 10x37, H = 0.11, 0.21, 0.5	FC - 72	Copper	Up to 20	55 - 1270	-	25	Up to 0.99	Flow regime map, h_{tp}, ΔP, T_w profile
Sheehan et al. [20]	2010	Microgap, 35x10, H = 0.21	FC - 72	copper	10.3 - 26	195.2	-	-	Up to > 0.9	Wall temperature fluctuations
Alam et al. [21]	2011	Microgap and microchannel, 12.7x12.7, H = 0.2 – 0.4	D.I. water	Silicon	0 - 100	400 -1000	-	86		Wall temperature gradient, comparison of microgap and micro channel
Morshed et al. [22]	2011	Microgap, 5×26, H = 0.36	D.I. water	Copper	0 - 60	45.9 - 143.8	104	22 - 80	-	h_{tp}, flow instabilities, nanowires on wall surface
Guo et al. [23]	2011	Microgap with square pin-fin, 10x10, S = 0.03, 0.05, H_f = 0.06, 0.12	FC-72	Silicon	Up to 150	0.5, 1, 1.5 m/s	-	T_{sub} = 25, 35	-	Effects of subcooling and jet impingement
Alam et al. [24]	2012	Microgap, 12.7x12.7, H = 0.19, 0.285, 0.381	D.I. water	Silicon	0 - 110	420, 690, 970	-	86	-	Gap heights, h_{tp}, ΔP
Alam et al. [25]	2012	Microgap, 12.7x12.7, H = 0.08 - 1	D.I. Water	Silicon	0 - 71	382 - 905	101	90 - 91	-	Flow regime, effects of gap heights, h_{tp}, ΔP

Morshed et al. [26]	2012	Microgap H = 372	D.I. water	Copper	Up to 60	45.5, 82	101	21	-	h_{sp}, Effects of grooves and nano particles
Isaacs et al. [27, 28]	2012, 2013	Microgap with staggered circular pin-fin, 10x10, H = 0.2, D = 0.15	R245fa	Silicon	Up to 40	598 - 1639	-	T_{sub}= 10, 13	Up to 0.1	h_{tp}, x, bubble nucleation, two phase flow pattern
Alam et al. [29]	2013	Microgap, 12.7x12.7, H = 0.2, 0.3, and 0.5, R = 0.6, 1.0 and 1.6 μm	D.I. water	Silicon	0 - 85	390, 650	101	91	-	The influences of surface roughness on flow boiling heat transfer, pressure drop and instability in microgap.
Alam et al. [30]	2013	Microgap and microchannel. 12.7x12.7, H = 0.19	D.I. water	Silicon	0 - 85	400 - 1000	101	86	-	h_{tp}, ΔP, pressure instabilities, comparison of microgap and micro channel
Dai et al. [31]	2013	Microgap with copper mesh, mesh thickness = 0.16, 5.5x26, H =0.34	D.I. water	Copper	Up to 311	Up to 1300	-	-	-	Flow separation
Reeser et al. [32]	2014	Microgap with square pin-fin, inline and staggered, 9.6x28.8, H = 0.305, S=0.153	HFE-7200 /	Copper	1 – 36 / 10 – 110	200 – 600 / 400 – 1300	101	70 / 95	up to 0.9 /	h_{sp}, h_{tp}, ΔP_{tp} and their correlations

			D.I. water						up to 0.22	
David et al. [33]	2014	Microgap with staggered square pin-fin, 10x10, S = 0.35, H_f = 1	R134a	Copper	30 - 170	230–380	101	<30	0.2 – 0.75	h_{tp}, x, effects of time-varying heat flux
Ong et al. [34]	2014	Microgap with circular pin-fin, staggered (45 º and 27º), radial quadrant microgap with circular pin-fin, H = 0.12, D = 0.08	R1234ze	Silicon	Up to 99.5	Up to 0.00083 kg/s	-	T_{sub} up to 10 ℃	Up to 0.93	h_{tp}, x, f, flow instability, flow patterns
Yang and Schultz et al. [35, 36]	2015	radial quadrant microgap with circular pin-fin, 20.25x20.25, D = 0.08	R1234ze	Silicon	Up to 2100	Up to 0.0042 kg/s	590	27.5	Up to 0.72	Nonuniform heating, local hot spot
Tamanna et al. [37, 38]	2015	Microgap, 12.7x12.7, inlet height 0.2, outlet height 0.2, 0.3, 0.46	D.I. water	Silicon	0 - 80	400 - 1000	101	91	-	Effects of expanding in gap height
Woodcock et al. [39]	2015	Microgap with staggered Piranha Pin Fin, 2.4x22.5, H = 0.2, D = 0.15	HFE7000	Silicon	Up to 700	1200-7000	140, 280	-	Up to 0.2	Piranha pin fin, h_{sp}, h_{tp}, ΔP, x

1.1 Review of Experimental Studies on Flow Boiling in Plain Microgap

Lee et al. [8] and Yang et al. [9] studied flow boiling of R-113 in minigap and microgap with gap heights ranging from 2 mm to 0.2 mm. Lee et al. [8] developed a two phase heat transfer coefficient correlation for minigap and microgap flows. Their pressure drop data agreed well with a correlation obtained with adiabatic water air two phase flow in a microgap [40]. Flow patterns such as bubbly, intermittent, wavy, and annular were observed, and gap height was found to impact flow patterns and heat transfer characteristics [9]. As gap height decreased, annular flow was dominant, and intermittent and wavy flow diminished.

Sheehan et al. investigated wall temperature during flow boiling of FC-72 in a microgap using infrared (IR) imaging technique [14, 20]. Wall temperature fluctuations were reported, and ascribed to local dryout and re-wetting during film evaporation. They found that both the flow regime and heat flux influence the wall temperature fluctuations. Kim et al. studied subcooled flow boiling of FC-72 in a microgap as a cooling strategy for high power light emitting diode (LEDs) [18, 41]. The LEDs were mounted directly on the microgap cooler, and the peak heat fluxes measured was 20 W/cm^2. Three microgap heights, 110 μm, 210 μm and 500 μm, were studied for both single phase and two phase flow. The two phase heat transfer coefficients were found to be higher than for single phase flow. Generally, the two phase heat transfer coefficients were higher in shorter microgaps than in taller ones, ranging from 10 kW/m^{2}K to 7.5 kW/m^{2}K for 110 μm and 500 μm microgaps, respectively. Averaged two phase heat transfer coefficients were also compared with correlations of Chen [42] and Shah [43]. Closer agreement with Shah's correlation at lower quality, and with Chen's prediction at higher quality was found.

Alam et al. studied local flow boiling heat transfer and pressure drop characteristics in a silicon microgap heat sink using deionized (D.I.) water [24]. The microgap had an area of 1.27 cm × 1.27 cm, and an array of 5 × 5 heating elements and temperature sensors. Three gap heights were investigated, 180 μm, 285 μm and 381 μm. The experiments were conducted with three mass fluxes, 420 kg/m^{2}s, 690 kg/m^{2}s and 970 kg/m^{2}s, and effective heat flux ranging from 0 to 110 W/cm^2. Confined slug flow/annular flow were observed after onset of nucleate boiling as heat flux increased. At fixed mass flux and heat flux, smaller gap tended to have confined annular flow while larger gap tended to have confined slug flow. Thin liquid film evaporation was the main heat transfer mechanism in confined annular flow, resulting in higher heat transfer coefficients in smaller gap than in larger gap. This also agreed with Kim et al.'s work [18, 41]. Pressure drop increased with heat flux in smaller gap, but was independent of heat flux in larger gap. Wall temperatures were almost uniform along flow direction after boiling occurred for all gap heights.

Alam et al. studied the effects of surface roughness on flow boiling in microgap [29]. The device also had an area of 1.27 cm × 1.27 cm, and an array of 5 × 5 heating elements and temperature sensors. They tested three gap heights of 500 μm, 300 μm and 200 μm, and three surface roughness levels of 0.6 μm, 1.0 μm, and 1.6 μm. Lower wall superheat was sufficient to initiate boiling in microgap with higher surface roughness. Rougher surface also increased nucleation density, wall temperature uniformity and local two phase heat transfer coefficients. No significant effect on pressure drop was observed in microgap with different surface roughness. However, increased surface roughness showed an adverse effect on pressure instability and higher amplitude in pressure oscillations were observed. Using the same test setup, Alam et al. compared the ability of minimizing temperature gradient and mitigating hotspot of microgap and

microchannel [21, 30]. Tested microgap height was from 200 μm to 400 μm, and the 200 μm high microgap was compared with a microchannel with a channel pitch of 200 μm in [21]. Tested microgap height was 190 μm, and microchannel width was 208 μm and height was 386 μm in [30]. For uniform heating, at the same mass flux of 690 kg/m^{2}s and heat flux range from 0 – 60 W/cm^2, microgap cooled device demonstrated a smaller temperature gradient and smaller amplitude of pressure and temperature oscillation than microchannel [21]. Reducing gap heights suppressed flow oscillation as well. When a hotspot was activated, microgap also showed better temperature uniformity than microchannel, and smaller gap height lowered wall temperature compared to higher gap height. Microgap gave better heat transfer performance at high heat flux due to confined slug/annular flow was dominant, and microchannel performed better at low heat flux due to early occurrence of slug/annular flow [30]. At lower mass flux, microgap outperformed microchannel as well.

Alam et al. further studied the effects of microgap heights on two phase flow regimes, heat transfer coefficient and pressure drop [25]. They studied microgap heights from 80 μm to 1,000 μm. They found that for microgap heights smaller than 500 μm, confined slug flow was the dominant flow pattern at low heat flux, while confined annular flow was the dominant flow pattern at higher heat flux; for microgap heights larger than 700 μm, bubbly flow was dominant at lower heat flux while slug/annular flow was dominant at higher heat flux, which agreed with the findings in [4]. Thus they concluded that confinement occurred in microgap heights smaller than 500 μm, and effect of confinement was negligible for microgap heights larger than 700 μm. The microgap of heights from 100 μm to 500 μm among the tested height range presented best performance in terms of maintaining uniform and low wall temperatures and achieving high heat transfer

coefficients. Smaller microgap heights assisted in suppressing pressure and wall temperature oscillations as well.

Morshed et al. compared two phase heat transfer in a microgap with bare copper base surface, and copper base surface with electrochemically grown nanowires [22] using D.I. water. They studied mass fluxes ranging from 45.9 kg/m^2s to 143.8 kg/m^2s, heat fluxes ranging from 0 to 60 W/cm^2, and inlet temperatures ranging from 22 ℃ to 80 ℃. Their results indicated that the microgap with nanowires improved two phase heat transfer coefficient by up to 56%, with a pressure drop increase of 20%, and improved single phase heat transfer coefficient by up to 25%. The nanowires also reduced the wall superheat by up to 12 ℃ to initiate boiling. Morshed et al. also compared a microgap with bare copper surface with four square cross-grooves of 0.5 mm × 0.5 mm, and copper surface with four nano particle deposited cross-grooves [26]. The grooves increased both single phase and two phase heat transfer coefficients by up to 50%, increased critical heat flux (CHF) by 15%, and lowered the boiling incipience temperature. The nano particles deposited grooves could further lower boiling incipience temperature, however showed no evidence of heat transfer coefficient improvement.

1.2 Review of Experimental Studies on Flow Boiling in Microgap with Micro Pin-Fin Surface Enhancement

Kosar and Peles studied flow boiling of R-123 from a staggered circular micro pin-fin array [10] and staggered hydrofoil shaped micro pin-fin array [11] within a microchannel of 1.8 mm width, 1 cm length, and 243 μm height. While not a microgap, this configuration with relatively large length to width ratio, involves the use of surface enhancement features. The diameter of

circular pins in [10] was 99.5 μm. The near zero contact angle of R-123a on silicon resulted in deactivation of large nucleation sites, and high superheat as boiling initiated. At certain conditions, a slight increase in heat flux caused a sudden increase in boiling and flow oscillations, as well as pressure and temperature oscillations.

The microchannel in [11] contained an array of 20 by 12 or 13 (in tandem) staggered hydrofoil pin fins with a wetted perimeter of 1,030 μm and chord thickness of 10 μm. They tested heat flux range from 19 to 312 W/cm^2, and a mass flux range from 976 to 2,349 kg/m^{2}s. The heat transfer coefficient was found to increase with increasing heat flux until a maximum was reached, and then decreased monotonically with increasing heat flux until critical heat flux (CHF). The increasing trend at low quality was ascribed to nucleate boiling, and the decreasing trend at high quality to dominance of convective boiling heat transfer mechanism.

Krishnamurthy et al. studied flow boiling of water in a 1.8 mm wide, 1 cm long and 250 μm deep microchannel with staggered circular pin-fins of diameter of 100 μm and pitch-to-diameter ratio of 1.5 [13]. The authors tested heat flux ranging from 20 W/cm^2 to 350 W/cm^2, and mass flux ranging from 346 kg/m^{2}s to 794 kg/m^{2}s. The outlet of the device was maintained at atmospheric pressure. They found that two-phase heat transfer coefficient was moderately dependent on mass flux, and independent of heat flux, for the range of mass flux and heat flux tested. They developed a correlation to predict heat transfer coefficient using a superposition model based on Reynolds analogy. They also constructed a flow pattern map using gas and liquid Reynolds numbers defined using superficial velocities, and found good agreement with the flow map constructed for adiabatic micro-scale systems developed using D.I. water and nitrogen [44].

Lie et al investigated heat transfer coefficients and bubble characteristics in flow boiling of FC-72 in a microgap with inline square pin-fins with pin side length of 200 μm and 100 μm, pin height of 70 μm, and both transverse and longitudinal pitches same as pin side length [12]. They studied mass flux ranging from 287 – 431 kg/m^{2}s, and heat flux ranging from 0.1 – 10 W/cm^2. The flow pattern was mostly bubbly flow. Two phase heat transfer coefficients were found to be relatively independent of mass flux, and to increase with heat flux. The micro pin-fins improved bubble departure frequency and two phase heat transfer coefficients. Bubble departure diameter and active nucleation site density decreased with mass flux, while bubble departure frequency increased with mass flux. The departing bubbles at higher heat flux were significantly larger than those at lower heat flux.

Qu et al. studied flow boiling heat transfer of water in an array of staggered square micro-pin fins [15]. The pin fins covered an area of 3.38 cm length by 1 cm width. The cross-section area of a single pin was 200 μm by 200 μm, and height was 670 μm. Their tests were performed for inlet temperatures of 90 ℃, 60 ℃ and 30 ℃, with six mass fluxes in the range from 183 - 420 kg/m^2s for each inlet temperature. The outlet pressure ranged from 103 to 108 kPa, and heat flux ranged from 23.7 to 248.5 W/cm^2. They observed that the two phase heat transfer coefficient decreased with increasing heat flux at low quality, and was fairly constant at quality greater than 0.15. The two phase heat transfer coefficient was also independent of mass flux at quality greater than 0.15. The mean absolute error of their results was beyond $\pm 30\%$ when compared with the previously mentioned correlations developed by Krishnamurthy et al [13].

Subcooled flow boiling of FC-72 on a micro-pin-finned silicon chip was studied by Ma et al. [16] and Yuan et al. [17], respectively. They studied heat flux up to 150 W/cm^2, with three inlet

velocities, 0.5, 1, and 2 m/s. The micro-pin fins of sizes less than 100 μm were relatively small compared to channel width 30 mm and channel height 5 mm in both studies. Micro-pin-finned surface showed significant improvement in heat transfer, compared to smooth surface in terms of heat transfer coefficient and critical heat flux (CHF). CHF was also increased at higher subcooling, and the enhancement was more noticeable over the micro-pin-finned surfaces. With a similar test setup, Guo et al. conducted subcooled flow boiling of FC-72 on a micro pin fin silicon chip with jet impingement [23] to achieve enhanced heat transfer and delayed CHF. As jet velocity increased, increase in mixing and turbulence in stagnation area improved heat transfer significantly.

Isaacs et al. [27, 28] investigated flow boiling of R-245fa in staggered circular pin-fin enhanced microgap. The fined area was 1 cm × 1 cm and the circular pins had a pin diameter, height, and pitch of 150 μm, 200 μm and 225 μm, respectively. The tested mass flux ranged from 598 to 1639 kg/m^{2}s, heat flux up to 40 W/cm^2, and inlet subcooling of 10 ℃ and 13 ℃. By flow visualization, triangular shaped vapor wakes were observed after nucleation points.

A passive flow separation technique was proposed and tested by Dai et al. using a copper microgap of 5 mm (W) × 26 mm (L) × 0.34 mm (H) [31]. A 2-layer copper mesh of thickness 160 μm was present on copper surface. A portion of incoming fluid was routed to an opening of diameter 0.8 mm located in the center of microgap, and entered microgap from the opening. It was a passive flow separation because the fraction of liquid going through the center opening was purely determined by pressure force balance between microgap inlet and the opening during fluid flow. This flow separation was found to enhance mixing and reduce temperature gradient in single phase flow, as well as to suppress bubble growth and flow instabilities in two phase flow.

Reeser et al. recently studied heat transfer and pressure drop characteristics of HFE-7200 and D.I. water in inline and staggered micro pin fin arrays [32]. The arrays had a 0.96 × 2.88 cm footprint area and square pin fin width and height of 153 and 305 μm. For HFE-7200 and D.I. water, the mass flux ranged from 200 to 600 kg/m^2s and 400 to 1300 kg/m^2s, respectively, and heat fluxes ranged from 1 to 36 W/cm^2, and 10 to 110 W/cm^2, respectively. They achieved high exit quality up to 0.9 for HFE-7200. Heat transfer coefficients behavior differed significantly for HFE-7200 and D.I. water due to different properties of both working fluids. They also found that pressure drop correlation developed by Qu et al. [15] and heat transfer coefficient correlation developed by Krishnamurthy et al. [13] showed poor accuracy in prediction for their work and these correlations needed to be modified.

Ong et al. studied flow boiling of R1234ze in a radial hierarchical fluid network [34]. The concept was to introduce fluid inlet at the center of test device, and fluid was then directed radially to outlets located on the edge of test device. They utilized different sizes of orifices at inlet to distribute fluid flow to subsection of the test devices. The radial quadrant microgap with circular pin-fin mitigated the pressure gradients and reduced temperature gradient as well. They also studied microgap with staggered pin-fin (27° and 45°), but the results were not compared with radial quadrant test device. The observed two phase flow instabilities and believed two phase flow instabilities were related to the degree of inlet subcooling. Schultz and Yang et al. also tested a radial microgap with embedded pin arrays using the same fluid [35, 36]. The test device was 20.25 mm × 20.25 mm, and had 8 core heaters and 16 hotspot heaters, and they studied the effects of local hotspot. They found that 50% increase in mass flow rate only resulted in 8% increase in two phase heat transfer coefficients. Increase in mass flow rate did not necessarily help to mitigate

temperature nonuniformity. Using R-134a in an open loop, David et al. studied effects of transient heat load on two phase heat transfer coefficients in a microgap with staggered square pin fins [33]. Their results indicated that temperature was maintained near uniform under both steady state and transient heating. Higher heat transfer coefficient was achieved under transient heating than steady state heating. Heat transfer coefficient varied with vapor quality, and a peak was observed for vapor quality of 0.55.

Tamanna et al. investigated the effect of expanding the microgap height on flow boiling heat transfer and pressure drop characteristics [37, 38]. The microgap was formed with silicon base and polycarbonate cover with the inlet height of 200 μm for all gaps, and the outlet height increasing from 200 μm to 300 μm and to 460 μm. A delay of partial dryout was observed in the 200 – 460 μm microgap at a heat flux of 79 W/cm^2, compared to the straight 200 – 200 μm microgap at a heat flux of 61 W/cm^2. The expanding microgap with outlet height of 300 μm gives the smallest pressure drop, by providing room for the vapor expansion without excessive flow acceleration, and best wall temperature uniformity of all three tested heights. Further expansion of outlet height 460 μm increased pressure drop due to unstable boiling and vapor acceleration. The fluctuations in temperature caused by unstable boiling in microgap were found to be independent of fluid quality and heat fluxes [20].

Woodcock et al. developed a Piranha Pin Fin (PPF) structure in a micro gap [39]. They investigated flow boiling of HFE-7000 in PPF enhanced micro channel, and achieved heat flux as high as 700 W/cm^2. Tested mass fluxes ranged from 1200 kg/m^{2}s to 7000 kg/m^{2}s. A staggered array of PPFs, each of diameter 150 μm and with a 300 μm long tail, was used. The PPFs had open mouths on leading edges, with wall thickness of 30 μm, and fluid flow could come inside the PPFs

and be extracted from the bottom fluid passage of each PPF. This way heat transfer was significantly enhanced in single phase and two phase conditions.

In summary, the review on flow boiling in plain microgap and microgap with pin fin surface enhancement revealed the ability of this promising strategy as thermal management method for high heat flux removal. However, fundamental research is still needed to understand the physics of boiling in microgap and especially in microgap with pin fin surface enhancement. The dependencies of boiling mode, two phase heat transfer coefficient and pressure drop on inlet temperature, heat flux and mass flux are still unclear and require further investigation.

1.3 Research Objectives

The objective of this work is to study heat transfer and pressure drop characteristics of flow boiling of water in pin fin enhanced microgap, and to discuss possible application for electronics cooling. There are a few heat transfer coefficient and pressure drop correlations available in literature for flow boiling in microgap with pins, and generally the correlations developed by one author are not able to predict other authors' data satisfactorily. This is possibly caused by the fact that these correlations were developed from different tested geometry, such shapes and arrangement of pin fins, different tested working fluid, and different testing operation conditions, such as mass flux range, heat flux range, inlet fluid temperature, and system pressure. This work examines available correlations of heat transfer coefficient and pressure drop, and also proposes new heat transfer coefficient and pressure drop correlations based on current data. High speed visualization is utilized to understand physics of boiling, flow regimes, and heat transfer characteristics in different flow regimes. Since the boiling point of water at atmospheric pressure is 100 °C, which is too high for continuous operation of electronic devices, the system pressure is

reduced to lower water saturation temperature. To the best of the author's knowledge, flow boiling of water in pin fin enhanced microgap at reduced pressure was rarely studied in previous literature. The effects of spatially nonuniform heating on flow boiling of water in pin fin enhanced microgap were rarely seen in previous literature as well, which are also studied in this work. This can assist in designing of the pin fin enhanced microgap in application for electronics cooling, and the locations of heat source. This work also performs experimental study of flow boiling of HFE-7200 in pin fin enhanced microgap, and compares the heat transfer and pressure drop characteristics with water. Testing different working fluid reveals the effects of fluid properties on boiling. Two phase heat transfer coefficient and pressure drop correlations developed for water are examined with HFE-7200 data, and new correlations are proposed.

CHAPTER 2. EXPERIMENTAL SETUP AND DATA REDUCTION

This chapter introduces the experimental apparatus utilized for the flow boiling experiment. All the components are reported in detail. The design of tested devices is described. Data reduction and measurement uncertainty are also explained in this chapter.

2.1 General Experimental Apparatus

The experiment was performed in a closed flow loop as shown in Figure 3. It consists of gear pump (Micropump GAF Series), inline 2 μm particulate filter (Swagelok SS-4F-2), flow meter (Omega FLR1008ST-D, Key Instruments 6G06 R3), preheater, test section, heat exchanger (LYTRON LL520G12) and fluid reservoir (Swagelok 316L-HDF4-300). These components are connected using stainless steel tubing. The Omega flow meter was utilized to measure flow rates ranging from 20 – 200 mL/min, and the Key Instruments flow meter was utilized to measure flow rates below 20 mL/min. The preheater is a resistance heater wrapped on the outer surface of tubing upstream of test section using nickel ribbon resistance wire to control fluid temperature at test device inlet. Two-phase flow from the exit of test section is condensed in the heat exchanger, which is cooled by a thermostatic bath circulator (LabCompanion RW-1025G). Pressure and temperature are measured at multiple locations in the loop, as marked in Figure 3. Strain gauge pressure transducers (Omega PX219-300G-5V) and T-type thermocouples with diameter of 1/16 inch (Omega HTQSS-116G-12) are utilized for these measurements. A pressure regulating valve is provided to control test section inlet pressure, and prevent reverse flow and two phase instabilities, as suggested by previous researchers [9-12]. Data were collected using Agilent 34970A data acquisition unit. Two phase flow was visualized using Vision Research v211 high

speed camera with a frame rate of up to 300,000 frames per second (fps). One available lens is Infinity InfiniProbe TS-160, which enables viewing an adjustable relatively large area. The other lens used is OPTEM 399510-309 with 70X, magnification which enables examination of boiling behavior around a single pin. SCHOTT KL 2500 LED Fiber Optic Light Source is used to illuminate boiling area for flow visualization.

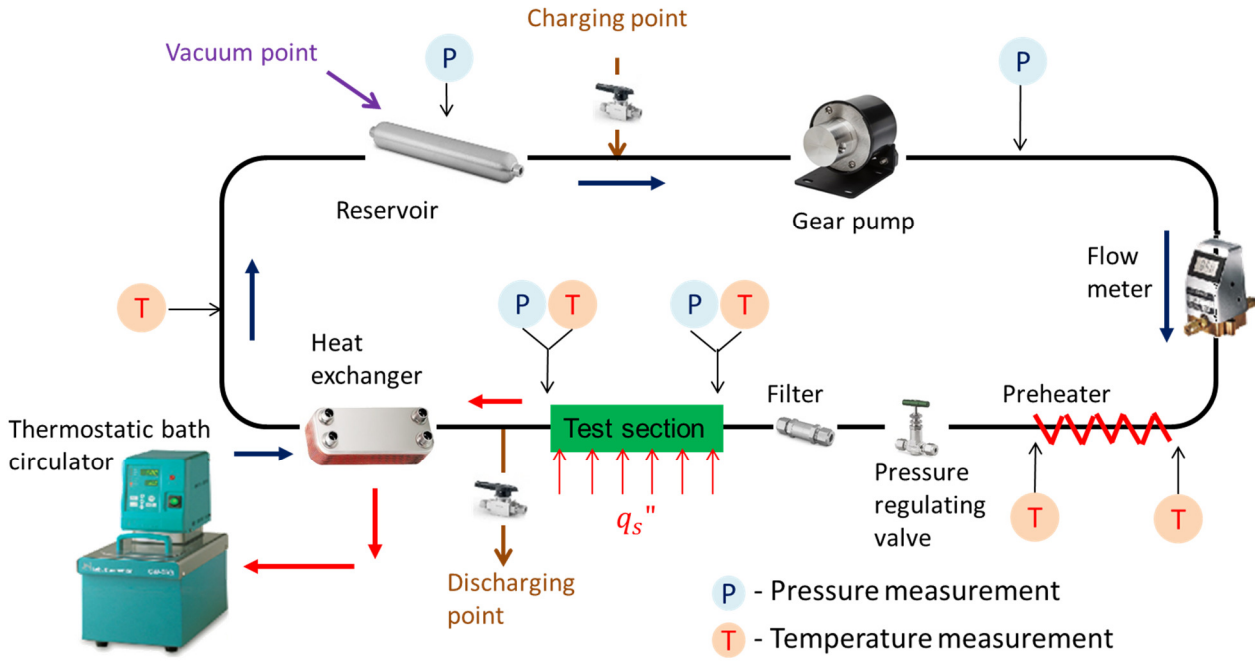

Figure 3 Flow loop schematic

2.2 Test Section

Figure 4 illustrates the schematic of the test section. The staggered pin-fin enhanced microgap was micro-fabricated from silicon, and was anodically bonded to Pyrex to form a closed channel that enables flow visualization. The device was sandwiched between the printed circuit board (PCB) and package, which were affixed with screws and nuts. The device was taped to PCB using double-sided high temperature Kapton tape and electrically connected to the PCB by

wirebonding. The package was designed to connect the device to the flow loop, and to enable local inlet and outlet pressure and temperature measurements. Thermocouples were inserted into inlet and outlet fluid plenums inside package, so inlet and outlet fluid temperatures can be measured at locations that were only 8 mm away from the device. O-rings were used to seal between the device and the package.

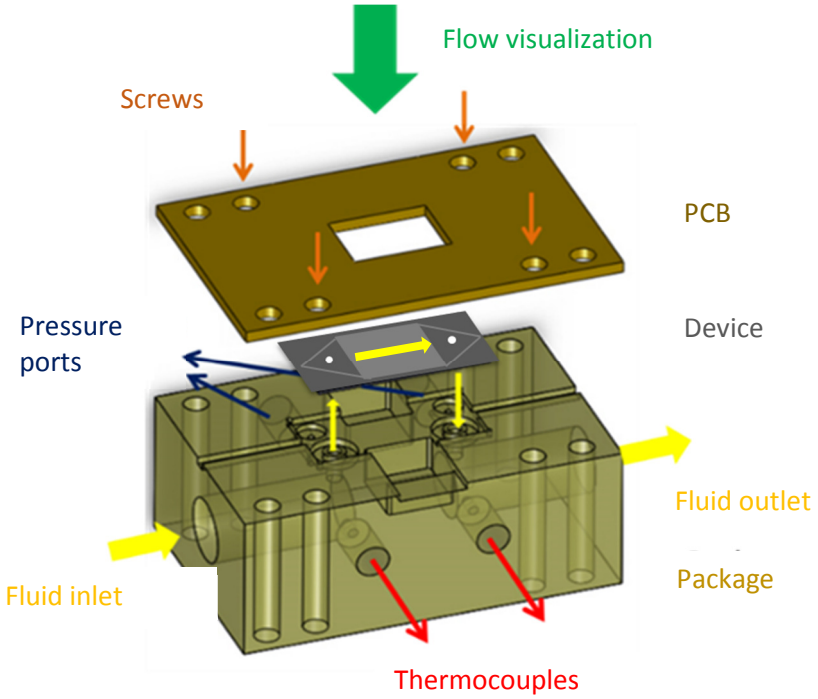

Figure 4 Test section

Figure 5 shows the CAD drawing of the device. The staggered pin-fins cover an area of 1 cm × 1 cm. Cylindrical support pins in the inlet and outlet plenums are to add structural strength. There are four row of oval shape pins upstream of the staggered pin-fin arrays to redistribute fluid flow to obtain better velocity uniformity. Pressure taps are placed upstream and downstream of the staggered pin-fin arrays, as seen in Figure 5 a). Figure 5 b) shows the heater side of the device. Four serpentine platinum resistance heaters are deposited on this side, also covering an area of 1

cm × 1 cm right on the opposite side of the pin-fin array. The heaters also work as resistance temperature detectors (RTDs) due to the fact that the resistance of platinum varies with temperature nearly linearly over the tested temperature range. A representative heater resistance versus temperature calibration curve is shown in Figure 6. The size of device is 28 mm (length) × 13.5 mm (width) × 1.2 mm (thickness).

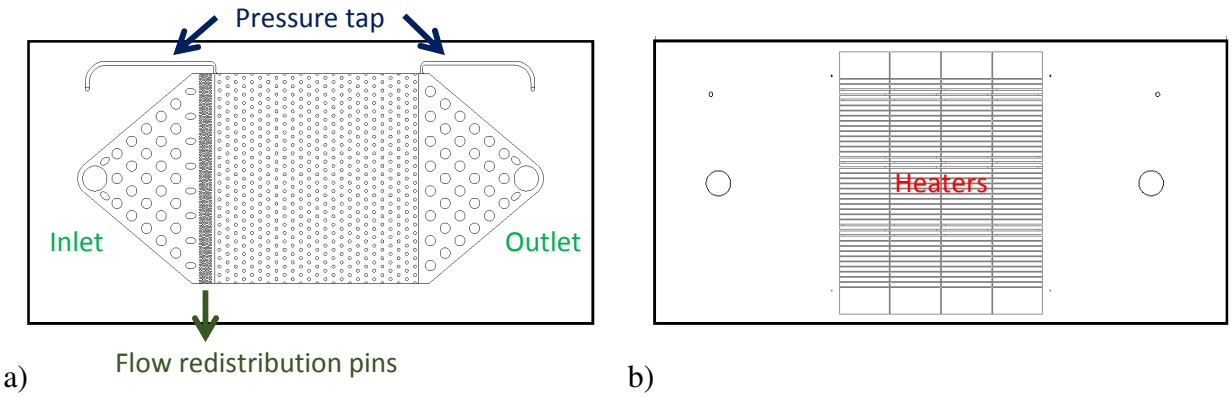

Figure 5 Device schematic: a) heat sink side with micro pin-fins; b) heater side with four microfabricated resistance heaters

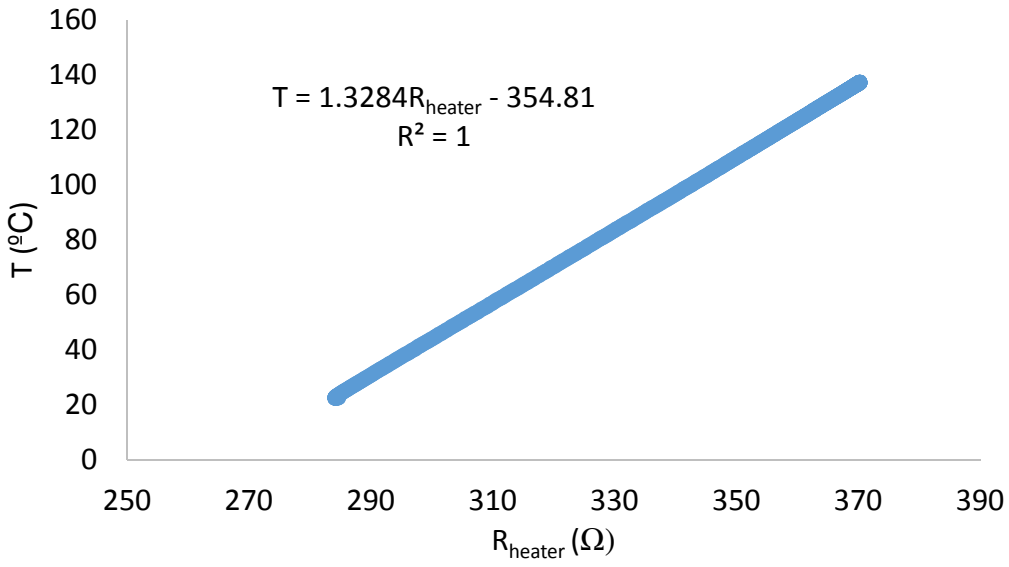

Figure 6 Heater calibration curve

Two pin fin configurations were studied, as shown in Figure 7. Both the sparse device and dense device have the same pin diameter of 150 µm and pin height of 200 µm which is also the microgap height. Transverse pitch S_T and longitudinal S_L are both 400 µm for sparse device, and 200 µm for dense device. The total number of circular pins in sparse and dense devices are 625 and 2450, respectively. These two configurations increased surface area to 1.48 and 2.88 times the plain surface, respectively.

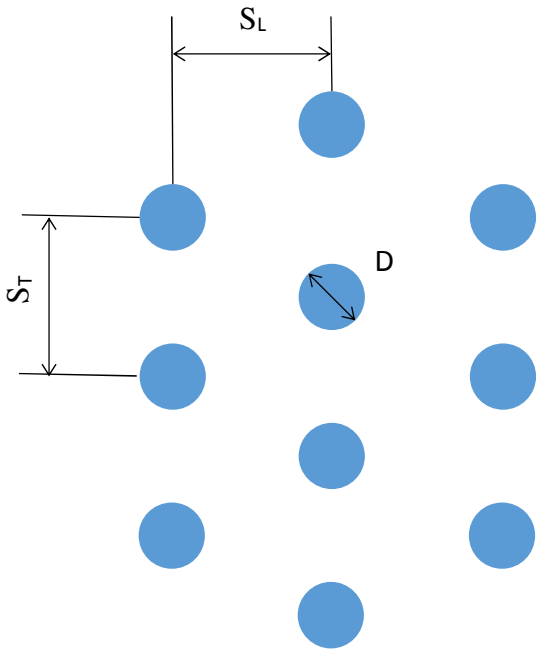

	Sparse Device	Dense Device
S_T (µm)	400	200
S_L (µm)	400	200
D (µm)	150	150
H_f (µm)	200	200
N_{tot}	625	2450

Figure 7 Pin fin dimensions

2.3 Data Reduction

Heat loss was estimated before two phase experiments. The devices were powered in vacuumed flow system until steady state temperatures were reached, to obtain the power and temperature calibration curve. Since the power supplied to the device was completely lost to ambient, the resulting curves, as shown in Figure 8, are the heat loss versus temperature curves

and are used for heat loss estimation in two phase experiment data reduction. The heat loss is less than 5% for all experiments.

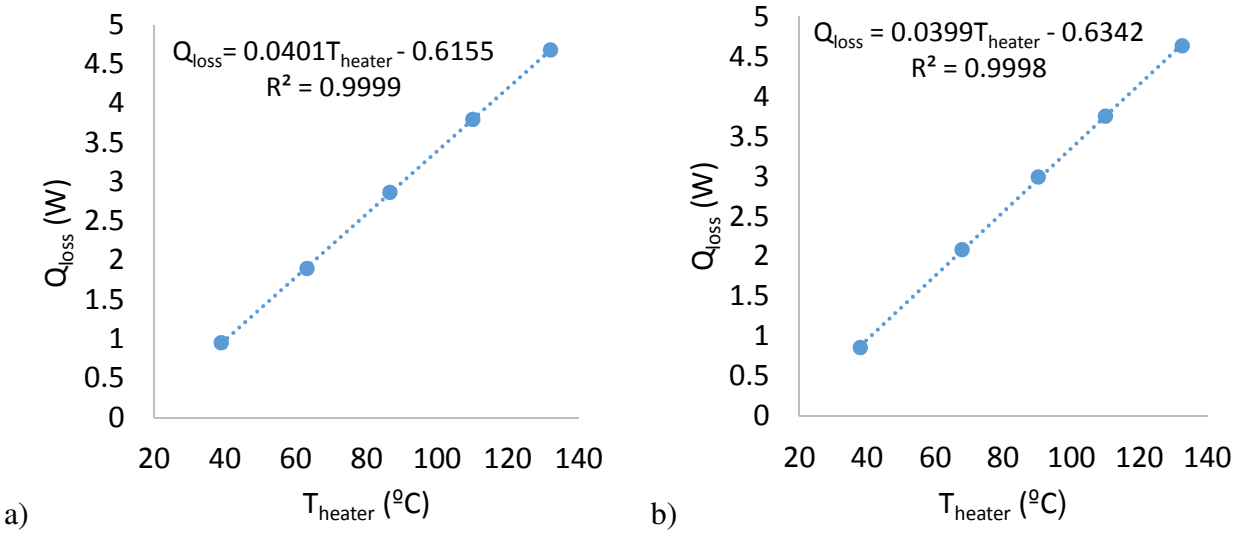

a) b)

Figure 8 Heat loss vs T_{heater}: a) Sparse device; b) Dense device

The effective heat flux is

$$q_{eff}" = \frac{P_{total} - Q_{loss}}{A_h} \tag{1}$$

where P_{total} is the total applied power, Q_{loss} is the heat loss, and A_h is the heater area.

Mass flux is defined as

$$G_{max} = \frac{\dot{m}}{A_{c,min}} \tag{2}$$

$A_{c,min}$ is minimum cross-section area of the microgap, and thus

$$A_{c,min} = \left(W_g - \frac{W_g}{S_T} D\right) H_g \tag{3}$$

The local two phase heat transfer coefficient h_{tp} was calculated using fin efficiency, and solved from

$$q_{eff}"A_{h,tp} = h_{tp}(A_{b,tp} - N_{tp}A_c)(T_w - T_{sat}) + h_{tp}\eta_f N_{tp} A_f (T_w - T_{sat}) \tag{4}$$

where $A_{b,tp}$ is base area of two phase region, A_f is a single pin fin surface area exposed to fluid, and A_c is the cross-section area of a single pin fin. N_{tp} is total number of pin fins in two phase region. Assuming that fin tip was insulated, fin efficiency η_f can be calculated using

$$\eta_f = \frac{\tanh(mH_f)}{mH_f} \tag{5}$$

where $m = \sqrt{\frac{h_{tp}P_f}{k_{Si}A_c}}$, P_f is pin fin perimeter, and k_{Si} is the thermal conductivity of silicon.

Wall temperature T_w was calculated by assuming one dimensional conduction in silicon heat sink base and the silicon dioxide passivation layer,

$$T_w = T_h - q_{eff}"\left(\frac{t_{Si}}{k_{Si}} + \frac{t_{SiO_2}}{k_{SiO_2}}\right) \tag{6}$$

The thickness of silicon base and silicon dioxide passivation layer are 300 μm and 2 μm, respectively.

T_{sat} was evaluated using local two phase pressure. The pressure at the row of pins where single phase region transitions to two phase region is

$$P_{tp,0} = P_{in} - \Delta P_{sub} \tag{7}$$

where ΔP_{sub} is the pressure drop of single phase region. ΔP_{sub} was estimated using similar format of equation used by Qu and Siu-Ho [45]

$$\Delta P_{sub} = \sum_{i=1}^{N_{tr}} f_{sp,i} \frac{G_{max}^2}{2\rho_l} \tag{8}$$

and N_{tr} is the row number where single phase region transitions to two phase region. $f_{sp,i}$ is single phase friction factor. The single phase frictional factor was determined from hydraulic tests of the sparse and dense device, and

$$f_{sp,i} = 30 \left(\frac{S_T}{D}\right)^{-1.18} \left(\frac{S_L}{D}\right)^{-1.18} Re_{D,max}^{-0.449} \tag{9}$$

$Re_{D,max} = \frac{G_{max} D}{\mu}$, is single phase Reynolds number.

The local two phase pressure was evaluated by adopting the assumption that the pressure gradient is constant in two phase region, which is the same as Qu and Siu-Ho [15].

The exit vapor quality is calculated from

$$x = \frac{q_{eff}"A_h - \dot{m}C_P\left(T_{sat,o} - T_{in}\right)}{h_{vap}\dot{m}} \tag{10}$$

where $T_{sat,o}$ is saturation temperature evaluated at device outlet pressure.

Local single phase heat transfer coefficient h_{sp} was calculated in single phase region using

$$q_{eff}"A_{h,sp} = h_{sp}\left(T_w - T_f\right)\left(\eta_f A_f N_{sp} + A_{b,sp} - N_{sp}A_c\right) \tag{11}$$

where $A_{h,sp}$ and N_{sp} were heated area and number of pin fins both associated with single phase region. Fluid temperature T_f was evaluated from

$$T_f = T_{in} + \frac{q_{eff}"A_{h,sp}/(\dot{m}C_P)}{2} \tag{12}$$

2.4 Uncertainty Analysis

Data directly collected from data acquisition unit, such as fluid temperature, pressure, and flow rate, are averaged using 10 measurements at steady state and standard deviation was calculated. The flow meters, thermocouples, and pressure transducers were calibrated to an uncertainty of ± 0.6 mL/min, ± 0.3 ℃, and $\pm 1\%$, respectively. $\pm 1\%$ uncertainty in pressure measurement results in an uncertainty of $\pm 0.3\%$ in saturation temperature. The uncertainty in voltage and current measurement are both 0.1%.

The measurement uncertain estimation follows Kline-McClintock method [46]. The uncertainty of effective heat flux is

$$\delta q_{eff}" = \sqrt{\left(\frac{I}{A_h}\delta V\right)^2 + \left(\frac{V}{A_h}\delta A\right)^2 + \left(\frac{1}{A_h}\delta Q_{loss}\right)^2} \tag{13}$$

The uncertainty of mass flux is calculated from

$$\delta G_{max} = \sqrt{\left(\frac{1}{A_{c,min}}\dot{m}\right)^2} \tag{14}$$

The uncertainty of two phase heat transfer coefficient is

$$\delta h_{tp} = \sqrt{\left(\frac{A_{h,tp}}{C_0(T_w - T_{sat})}\delta q_{eff}"\right)^2 + \left(\frac{q_{eff}"A_{h,tp}}{C_0^2(T_w - T_{sat})^2}\delta T_w\right)^2 + \left(\frac{q_{eff}"A_{h,tp}}{C_0^2(T_w - T_{sat})^2}\delta T_{sat}\right)^2} \tag{15}$$

where $C_0 = A_{b,tp} - N_{tp}A_c + \eta_f N_{tp}A_f$.

Similarly, the uncertainty in single phase heat transfer coefficient is calculated from

$$\delta h_{sp} = \sqrt{\left(\frac{A_{h,sp}}{C_0(T_w - T_f)}\delta q_{eff}"\right)^2 + \left(\frac{q_{eff}"A_{h,sp}}{C_0^2(T_w - T_f)^2}\delta T_w\right)^2 + \left(\frac{q_{eff}"A_{h,sp}}{C_0^2(T_w - T_f)^2}\delta T_f\right)^2} \tag{16}$$

The uncertainty of exit quality is

$$\delta x = \sqrt{\left(\frac{A_h}{h_{vap}\dot{m}}\delta q_{eff}{}''\right)^2 + \left(\frac{C_p}{h_{vap}}\delta T_{sat}\right)^2 + \left(\frac{C_p}{h_{vap}}\delta T_{in}\right)^2 + \left(\frac{q_{eff}{}''A_h}{h_{vap}\dot{m}^2}\delta\dot{m}\right)^2} \quad (17)$$

The uncertainty in fluid temperature T_f is calculated from

$$\delta T_f = \sqrt{(\delta T_{in})^2 + \left(\frac{A_{h,sp}}{2\dot{m}C_p}\delta q_{eff}{}''\right)^2 + \left(\frac{q_{eff}{}''A_{h,sp}}{2C_p\dot{m}^2}\delta\dot{m}\right)^2} \quad (18)$$

CHAPTER 3. FLOW BOILING OF WATER IN PIN FIN ENHANCED MICROGAP AT REDUCED PRESSURE

This chapter studies pressure drop and heat transfer characteristics of flow boiling of water in pin fin enhanced microgaps at reduced pressure. The studied mass flux ranges from 120 to 865 kg/m^{2}s, heat flux from 10 to 300 W/cm^2, and inlet fluid temperatures from 30 to 80 ºC. Existing two phase heat transfer coefficient and pressure drop correlations are compared with current data, and new two phase heat transfer coefficient and two phase pressure drop correlations are developed based on current data. Observed two phase flow instabilities are discussed. Flow visualization observations are analyzed, and utilized to explain heat transfer performance.

3.1 Experiment procedure

Before starting the experiments, deionized (D.I.) water was boiled for 20 minutes to remove dissolved air, and the cooled in a sealed container to room temperature. The resulting dissolved oxygen in D.I. water was measured to be 2.8 ppm (Fisher Scientific oxygen meter 13-636-AP84). The effects of dissolved air on boiling can be neglected when dissolved oxygen is less than 5.6 ppm, as reported by Steinke and Kandlikar [47]. The flow loop was first evacuated use vacuum pump and then charged with degassed D.I. water. For each mass flux, heat flux was increased by 10 W/cm^2 each time to collect data, until heater temperature reached 130 ºC, or critical heat flux was reached.

The mass flux and inlet fluid temperature test conditions are listed in Table 3. Inlet pressure, outlet pressure, saturation temperatures at inlet and outlet pressures when heater power was not

supplied are also listed in Table 3. Three volume flow rates with subcooled and saturated inlet temperature conditions are studied. For the dense device at volume flow rate of 52 ml/min (G_{max} = 1730 kg/m^{2}s), no boiling in the pin fin array was observed for all three inlet temperatures of 30 ºC, 55 ºC and 80 ºC before heater temperature reached 130 ºC. Each set of data was repeated 2-3 times and they showed good agreement within measurement uncertainty.

Table 3 Test conditions

Device	VFR (mL/min)	G_{max} (kg/m^{2}s)	T_{in} (ºC)	P_{in} (kPa)	T_{sat} @ P_{in} (ºC)	P_{out} (kPa)	T_{sat} @ P_{out} (ºC)	Inlet Fluid Condition
Sparse	9	120	30	15.3	54.39	13.1	51.20	Subcooled
Sparse	9	120	55	17.0	56.6	13.5	51.82	Saturated
Sparse	26	346	30	16.5	55.97	14.3	53	Subcooled
Sparse	26	346	55	19.1	59.08	14.7	53.56	Near Saturated
Sparse	26	346	80	46.5	79.54	40.7	76.29	Saturated
Sparse	52	692	30	27.8	67.37	19.1	59.08	Subcooled
Sparse	52	692	55	27.6	67.21	22.4	62.54	Near Saturated
Sparse	52	692	80	47.8	80.22	45	78.74	Saturated
Dense	9	300	30	20.1	60.18	13.2	51.36	Subcooled

Dense	9	300	55	29.0	68.34	16.7	56.23	Near Saturated
Dense	26	865	30	44.6	78.52	16.2	55.59	Subcooled
Dense	26	865	55	41.8	76.94	18.6	58.51	Near Saturated
Dense	26	865	80	55.3	83.87	34.5	72.36	Saturated

The measurement uncertainties are estimated in Table 4.

Table 4 Measurement uncertainty

Variable	Uncertainty
P	1.3 %
T_f	$\pm$0.5 ºC
T_w	$\pm$0.8 ºC
q_{eff}"	0.25%
G_{max}	1.5%
h_{tp}	18 - 22 %
h_{sp}	15 %
x	2.2%

3.2 Results and Discussion

3.2.1 Flow Visualization

Flow direction is from left side to right side for all flow visualizations in this section. Figure 9 illustrates two phase flow for the sparse device at G_{max} = 120 kg/m^{2}s, T_{in} = 30 ºC, with multiple heat fluxes. Single phase liquid flow images are shown in first row for comparison. The discoloration in background in the single phase images are on the bottom wall, not due to fluid phase change. The left column illustrates the larger boiling area, and the right column illustrates zoomed in area. The boiling area is one big bubble, and as heat flux increased, vapor front moves towards inlet of microgap as seen from large area pictures. At low heat flux q_{eff}" = 18.4 W/cm^2, liquid films are attached on circular pin fins. These liquid films hold circular shapes by surface tension. At certain locations, liquid films of adjacent pins are connected. As heat flux increased to q_{eff}" = 37.5 W/cm^2, boiling area covers more than half of the pin fin array. A zoomed in image reveals that bubbles nucleate inside the liquid film attached to circular pin fins at the rear side of pin fin, and liquid films surrounding pin fins are separated. As heat flux increased to q_{eff}" = 57.6 W/cm^2, liquid films become thinner compared to the case when q_{eff}" = 18.4 W/cm^2, and liquid wakes show two sharp tails due to shear from accelerated vapor phase. Local dryout is observed when heat flux is further increased.

At q_{eff}" = 76.9 W/cm^2, boiling area covers 3/4 of the pin fin array, and local dryout is seen in the zoomed in image. At q_{eff}" = 94.8 W/cm^2, larger dryout area is seen and small liquid droplets from upstream are observed to pass the dryout region occasionally. Further increase of heat flux by a small increment leads to dramatic rise in heater temperature, which indicates critical heat flux condition is reached. This type of flow patterns are also observed for cases where G_{max} = 120

kg/m^{2}s, T_{in} = 55 ℃, and G_{max} = 346 kg/m^{2}s, T_{in} = 30 ℃. This results in the increasing and then decreasing trend of two phase heat transfer coefficients against heat flux.

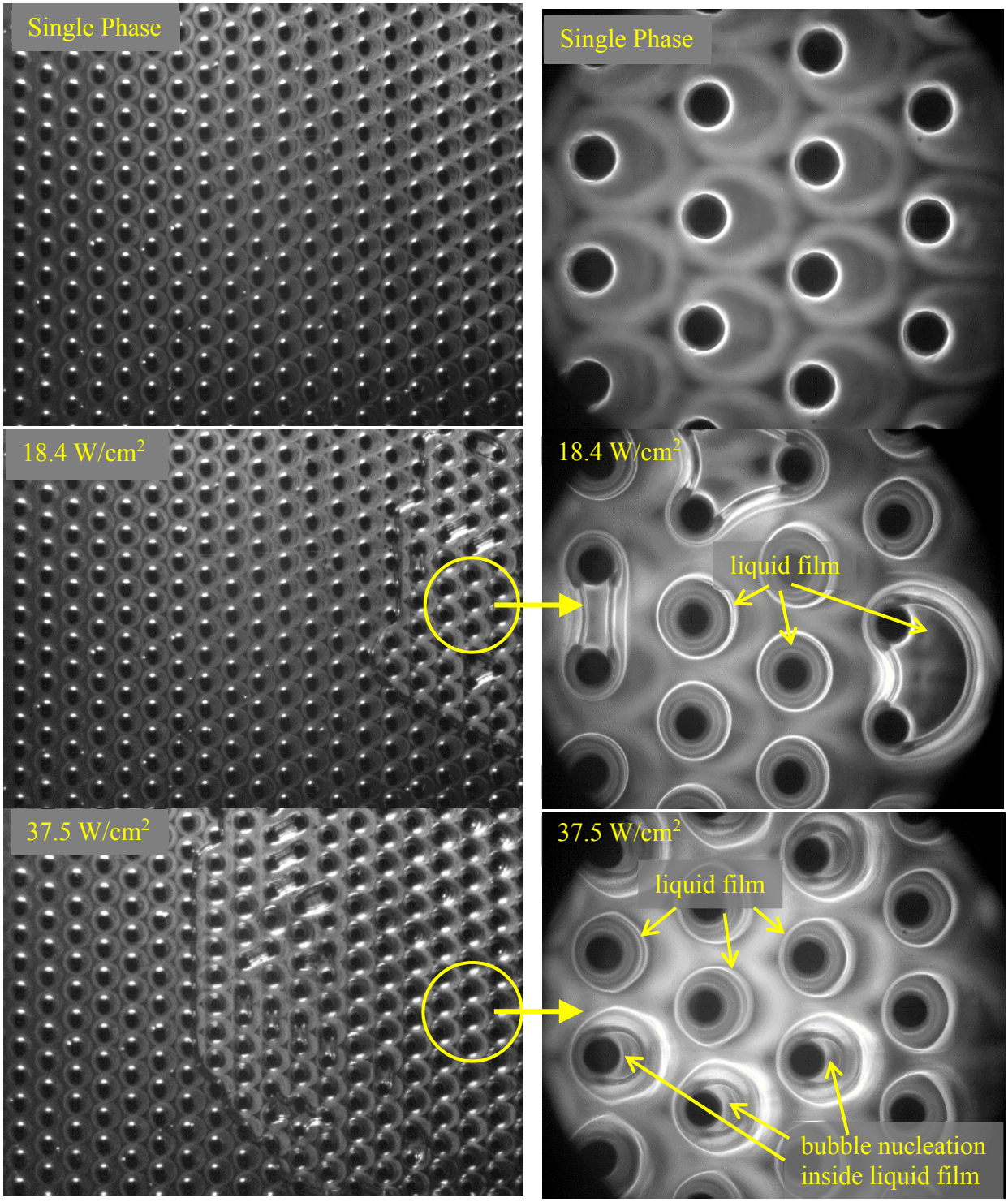

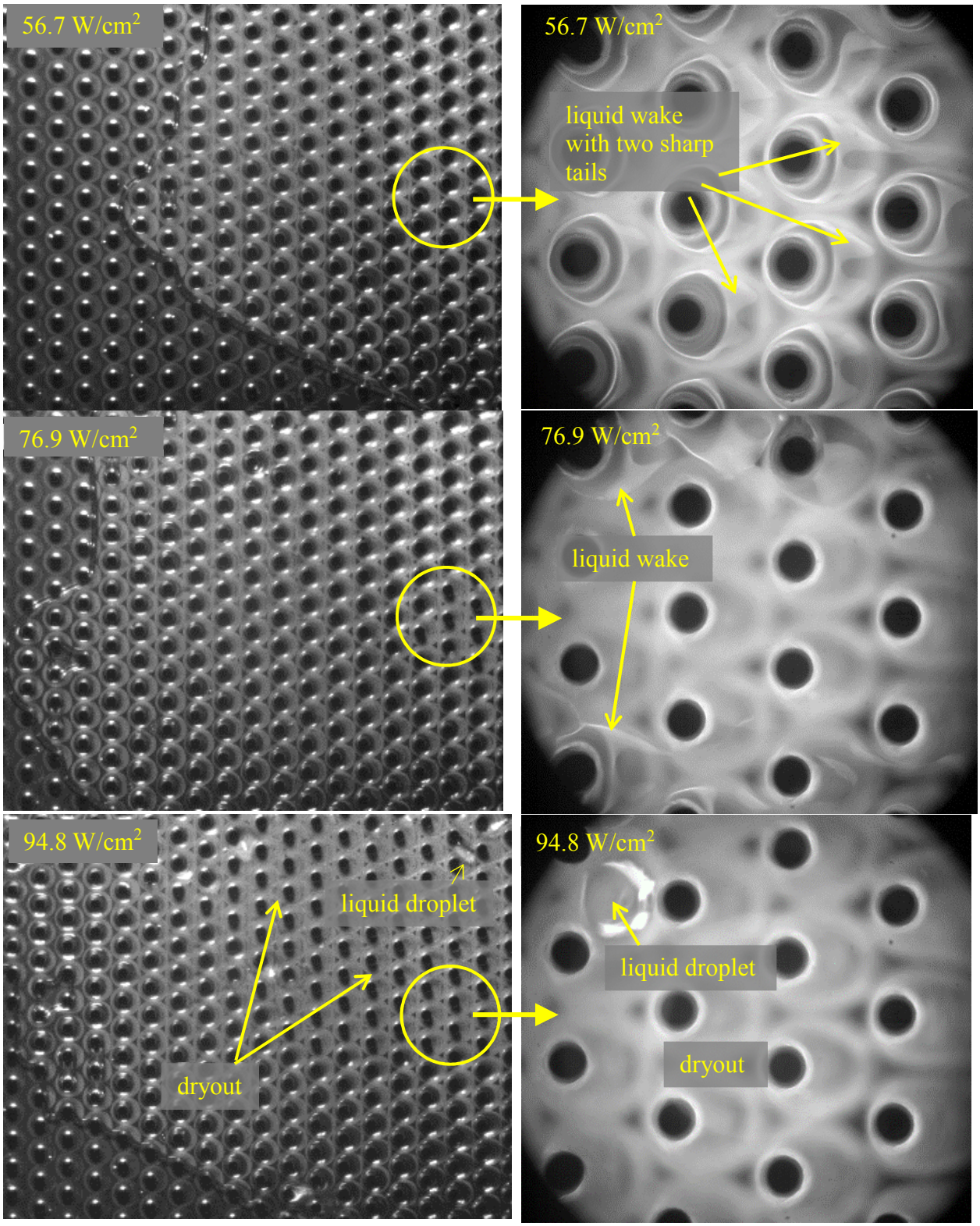

Figure 9 Flow visualization of sparse device at G_{max} = 120 kg/m^{2}s, T_{in} = 30 °C

Figure 10 shows flow visualization for the case where G_{max} = 346 kg/m^{2}s, and T_{in} = 55 ºC. At q_{eff}" = 96.4 W/cm^2, liquid films are seen to surround the circular pin pins, and bubble nucleation inside liquid film at the rear side of pin fin is also observed. There are also liquid films attached on some area of the bottom wall as seen in the zoomed in picture. At q_{eff}" = 155.1 W/cm^2, liquid wakes are stretched to sharp tails due to shear from vapor phase acceleration similarly as the case where G_{max} = 120 kg/m^{2}s, T_{in} = 30 ºC. Unlike the previous case, the two sharp tails merge to one sharp tail because mass flux is higher for this case, and stronger shear causes the two sharp tails to merge. Bubble nucleation inside liquid wakes is also seen at this heat flux condition. At the highest heat flux achieved for this case q_{eff}" = 195.7 W/cm^2, flow pattern is similar to the case q_{eff}" = 155.1 W/cm^2 with liquid wakes being sharp liquid tails and bubble nucleation inside liquid wakes. This set of flow visualization reveals that flow patterns do not have a significant change, and this indicates less dependence of local two phase heat transfer coefficients on heat flux compared to the case in Figure 9.

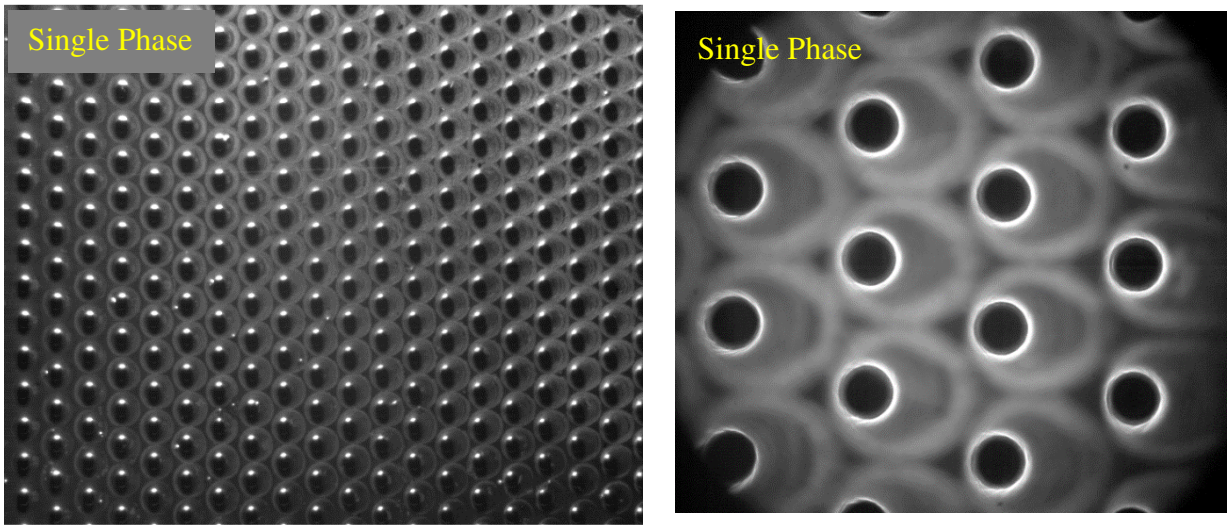

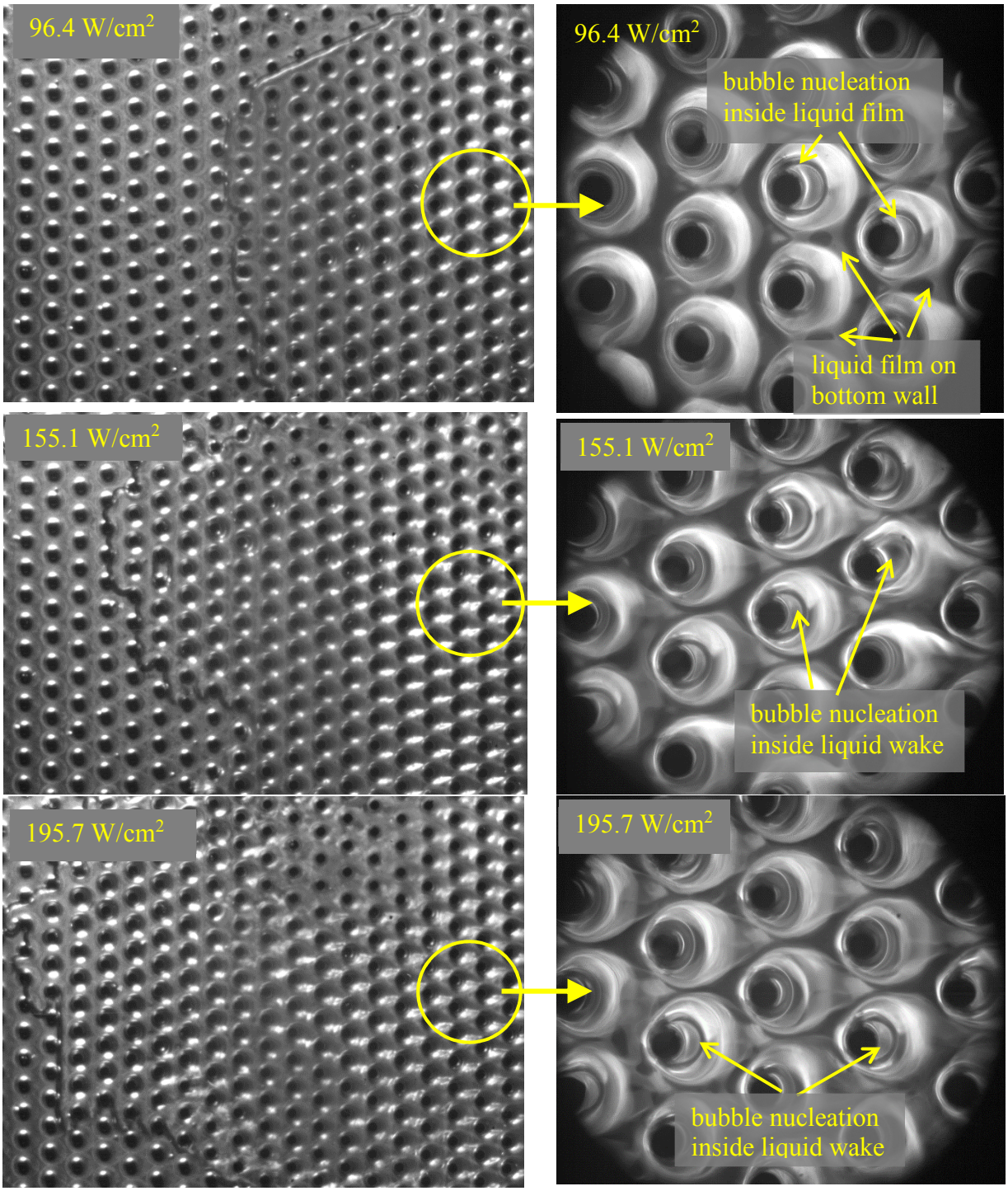

Figure 10 Flow visualization of sparse device at G_{max} = 346 kg/m^{2}s, T_{in} = 55 ^{o}C

Flow patterns at different time instances for q_{eff}" = 116.2 W/cm^2 are shown in Figure 11. At t = 0 ms, two phase mixture without a distinct liquid vapor interface occupies the boiling area.

At t = 1.46 ms, liquid wakes with two sharp tails become clear, and at t = 1.95 ms, bubbles nucleated inside liquid wakes are clearly seen. At t = 9.51 ms, two phase mixture without distinct interface coming from upstream and flushes away the liquid wakes with bubbles inside, and at t = 10.73 ms, liquid wakes with sharp tails start to show again. This happens periodically.

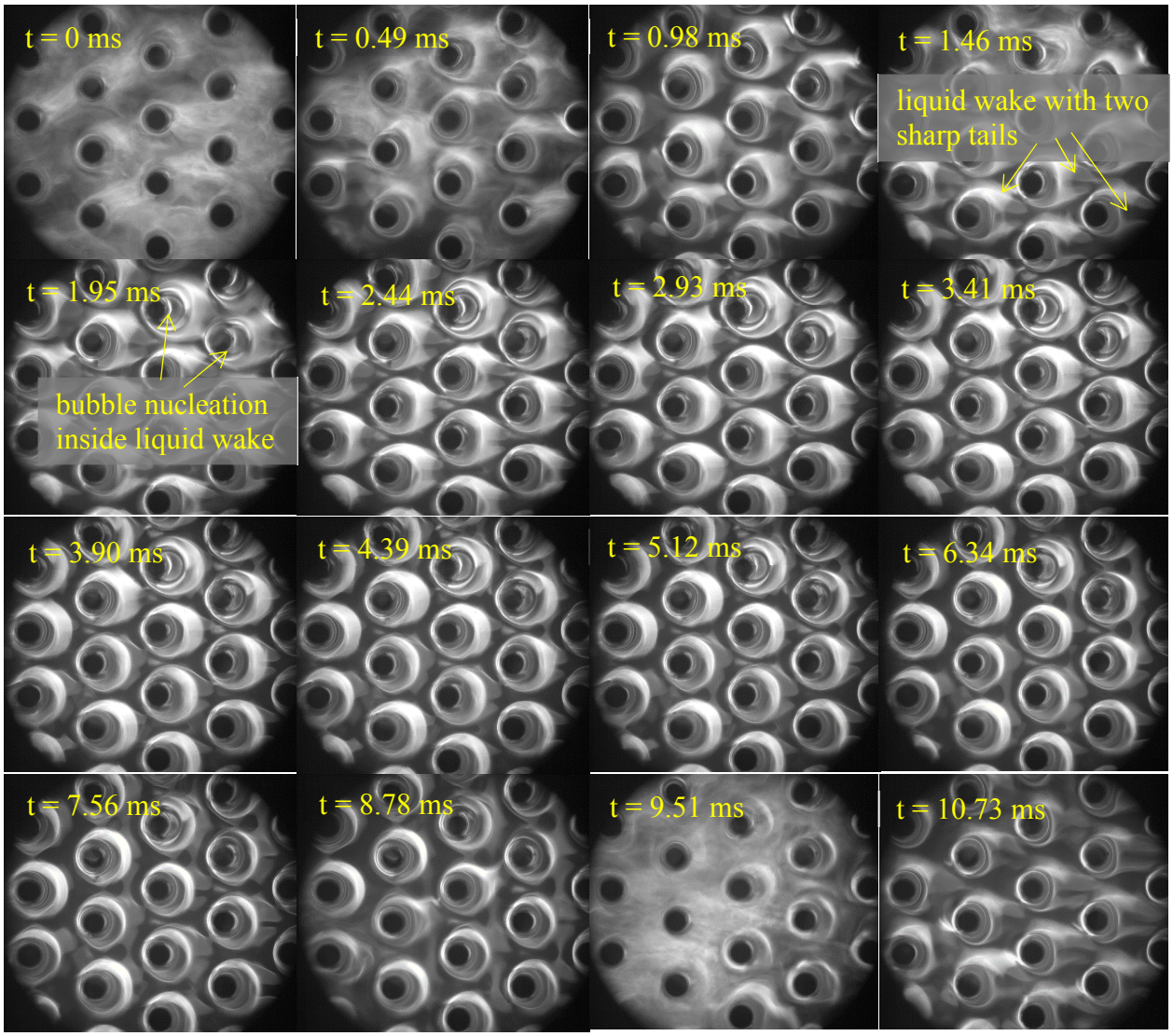

Figure 11 Flow visualization of sparse device at G_{max} = 346 kg/m^{2}s, T_{in} = 55 °C, q_{eff}" = 116.2 W/cm^2

Flow visualization at test condition of G_{max} = 346 kg/m^{2}s, T_{in} = 80 ºC, q_{eff}"=165.3 W/cm^2, and G_{max} = 692 kg/m^{2}s, T_{in} = 80 ºC, q_{eff}"=174.2 W/cm^2 are shown in Figure 12 and Figure 13, respectively. The heat fluxes are the highest achieved for these two cases. Both cases show stretched liquid wakes attached to pin fin and possible bubble nucleation inside liquid wakes. At a certain time instant, these flow patterns are present inside the pin fin arrays, and after a short period of time, two phase mixture without an obvious liquid vapor interface coming from upstream flushes the liquid wakes and bubbles inside. Then the stretched liquid wakes with bubble nucleation inside flow pattern start to reappear. This temporal behavior is true for all the tested cases.

For the case in Figure 12 with a lower mass flux G_{max} = 346 kg/m^{2}s, most of the time the stretched liquid wakes with bubble nucleation inside flow pattern occupies the pin fin array, as in images of t = 0 ms, 2.44 ms, 7.32 ms, 9.76 ms, 11.46 ms, 16.10 ms, 17.32 ms, 21.46 ms, 26.34 ms and 30.73 ms, and the two phase mixture with no obvious interface only happens occasionally and lasts for about 0.5 ms, as in images of t = 4.63 ms, 10.73 ms, 13.17 ms, 14.88 ms and 19.02 ms. At increased mass flux of G_{max} = 692 kg/m^{2}s as shown in Figure 13, the two phase mixture occupies the pin fin array most of the time, as in images of t = 0 ms, 1.95 ms, 4.39 ms, 6.83 ms, 9.27 ms, 10.49 ms, 12.93 ms, 14.39 ms, 18.78 ms, 20.49 ms, 24.63 ms and 25.85 ms, and the stretched liquid wakes with bubble nucleation inside flow pattern only appear occasionally and lasts for about 0.3 ms, as in images of t = 3.17 ms, 15.85 ms, 17.32 ms and 23.17 ms.

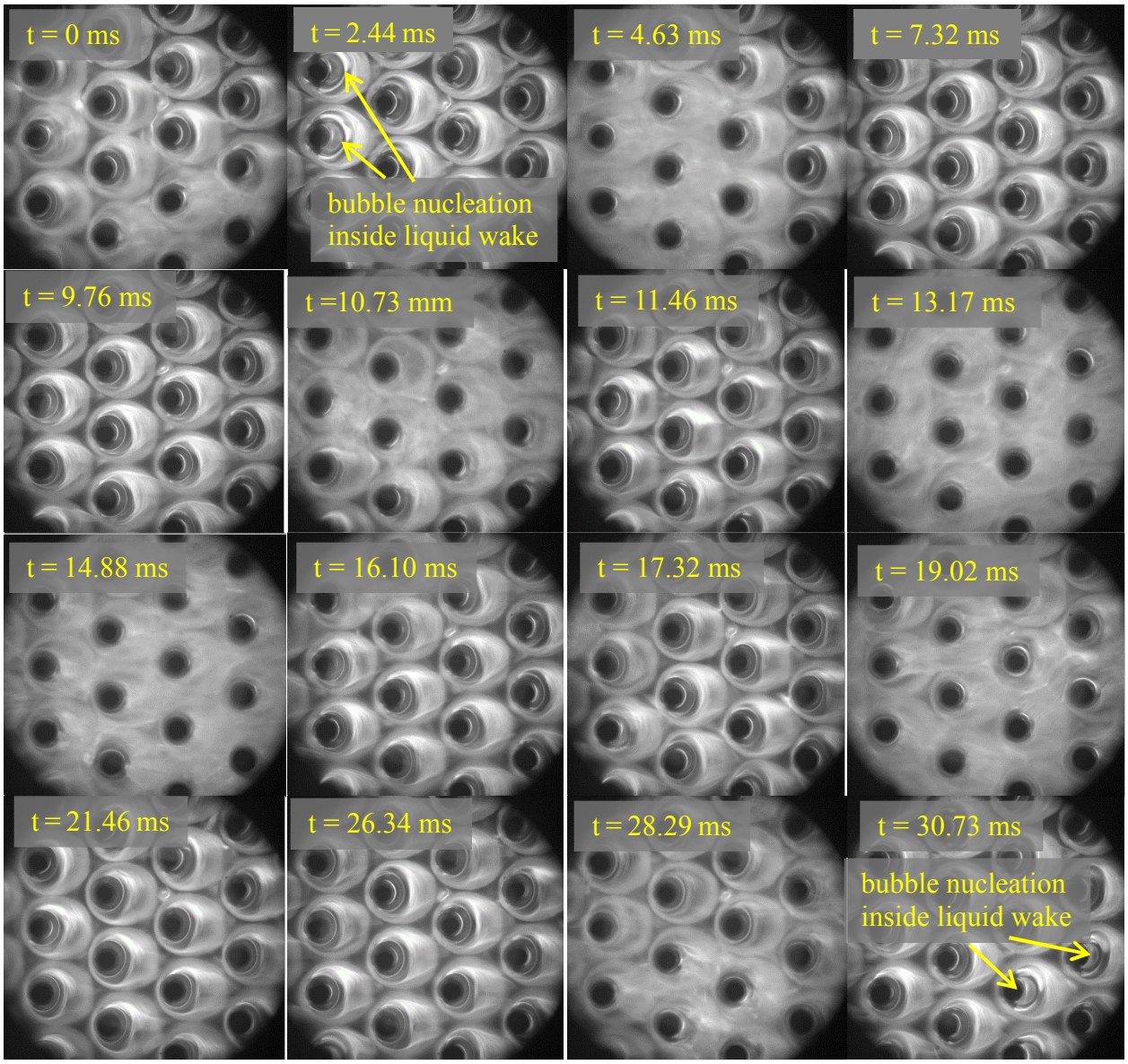

Figure 12 Flow visualization of sparse device at G_{max} = 346 kg/m^{2}s, T_{in} = 80 °C, q_{eff}" = 165.3 W/cm^2

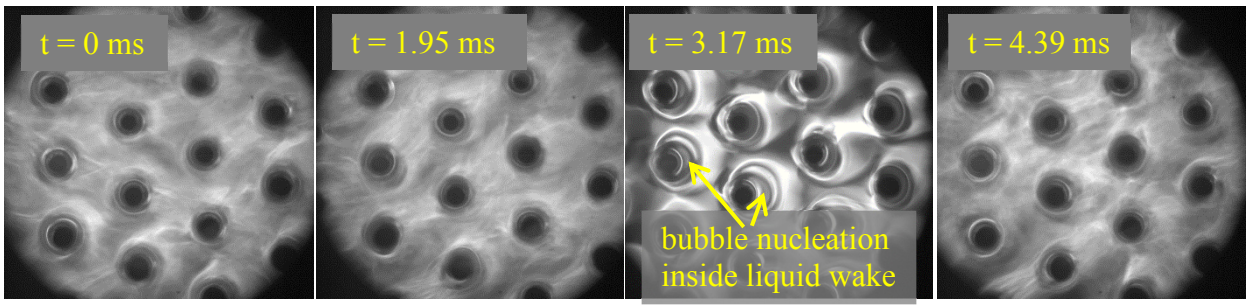

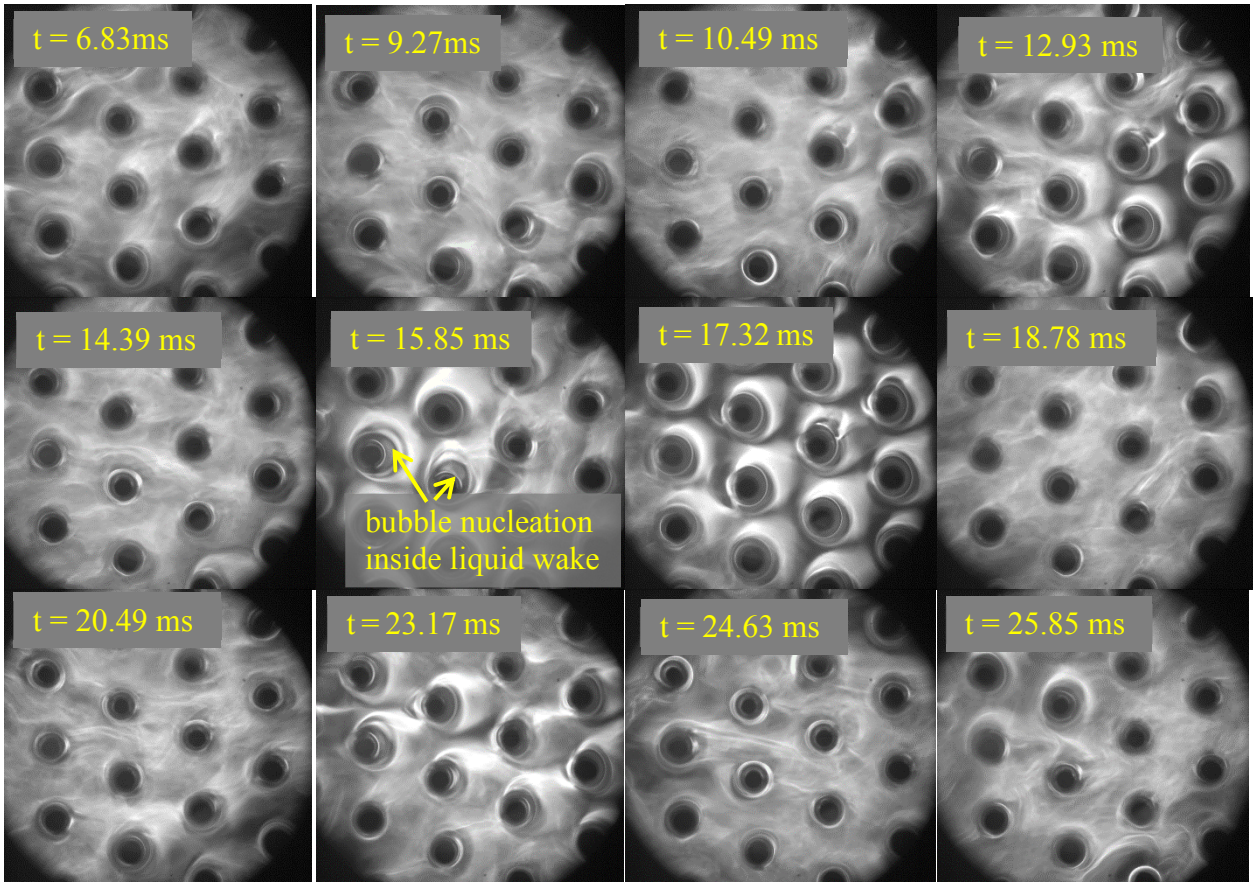

Figure 13 Flow visualization of sparse device at G_{max} = 692 kg/m^{2}s, T_{in} = 80 ºC, q_{eff}" = 174.2 W/cm^2

Figure 15 shows flow visualization of dense device at G_{max} = 300 kg/m^{2}s, and T_{in} = 55 ºC. The boiling region moves towards inlet of pin fin array as heat flux increases. At q_{eff}" = 9.9 W/cm^2, two phase flow covers less than half of the whole pin fin array at the downstream side. Large regions of liquid are seen in zoomed in images, or liquid film attached to adjacent pin fins are connected at certain locations. At upstream of boiling area, nucleated bubbles expand in transverse direction because it is easier for bubble to expand into larger gap than to squeeze through smaller gap between pin fins along flow direction, as seen in Figure 14. At q_{eff}" = 28.9 W/cm^2, liquid films surround circular pin fins uniformly as seen in the zoomed in images, and the boiling region covers

more than half of the pin fin array. Liquid film is thinner compared to the case q_{eff}" = 9.9 W/cm^2 with large regions of liquid, resulting in increase in two phase heat transfer coefficient. Separated bubbles at upstream are no longer seen.

At q_{eff}" = 57.8 W/cm^2, the liquid films surrounding pin fins offset to downstream side, or liquid film is thicker at the rear side of circular pin than at the front side of circular pin. At q_{eff}" = 77.3 W/cm^2, local dryout is observed. Further increase in heat flux leads to critical heat flux condition. Similar flow pattern is observed for dense device when G_{max} = 300 kg/m^{2}s, T_{in} = 30 ºC. This results in first increasing and then decreasing trend of local two heat transfer coefficient against heat flux. Unlike flow patterns observed in sparse device, no liquid wakes with sharp tails or bubble nucleation inside liquid wakes are seen in confined space in dense device. Bubbles nucleated upstream expand and move in transverse direction, instead of passing downstream due to limited gap size between pin fins.

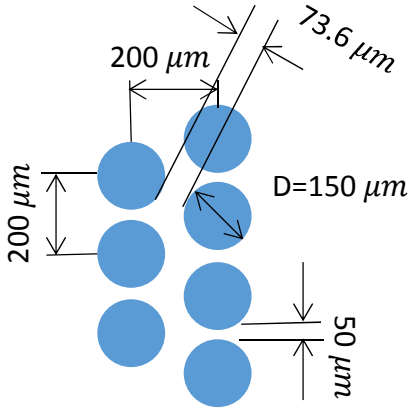

Figure 14 Dense device gap size

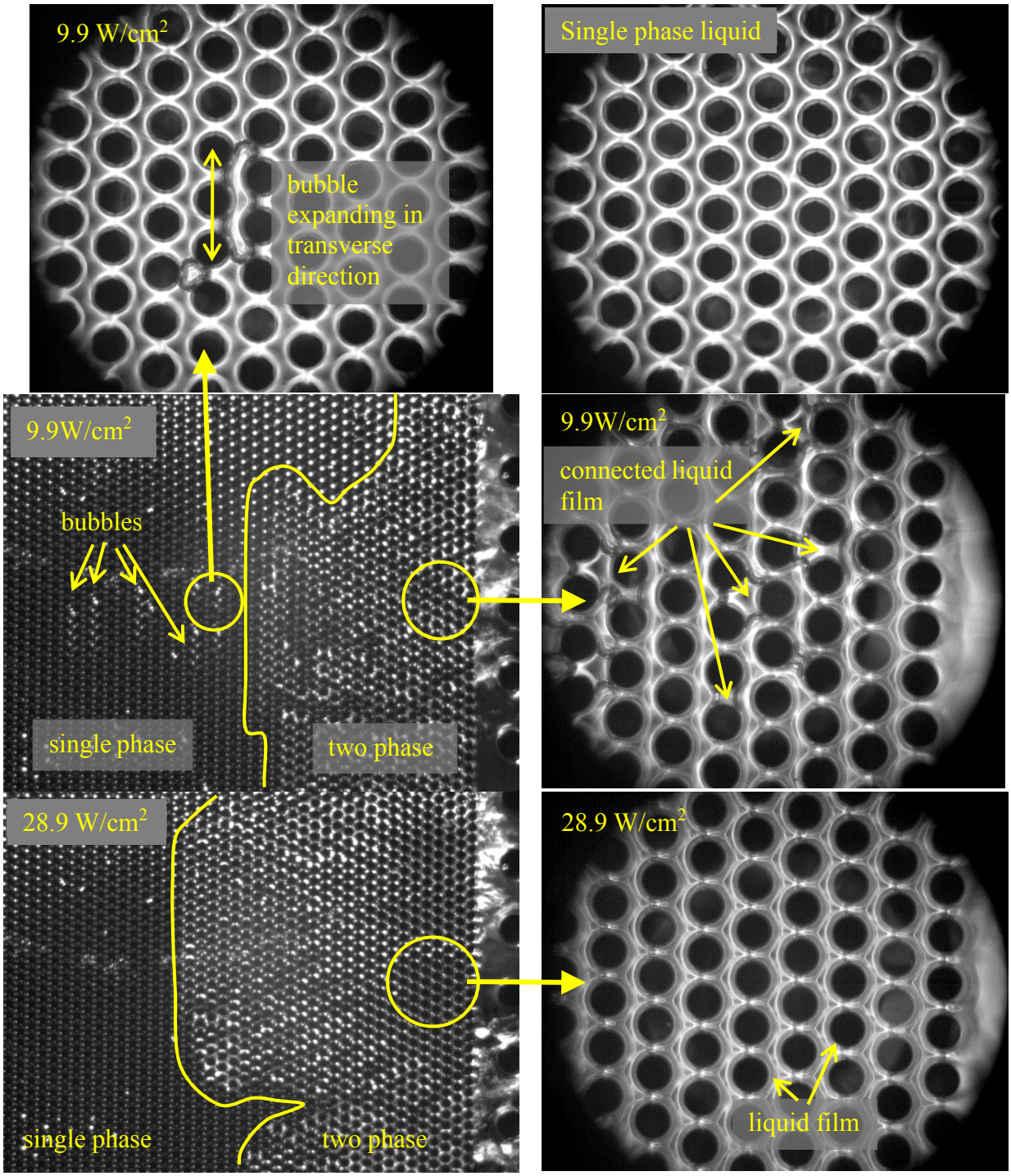
9.9 W/cm2
bubble expanding in transverse direction
Single phase liquid
9.9W/cm2
bubbles
single phase
two phase
9.9W/cm2
connected liquid film
28.9 W/cm2
single phase
two phase
28.9 W/cm2
liquid film

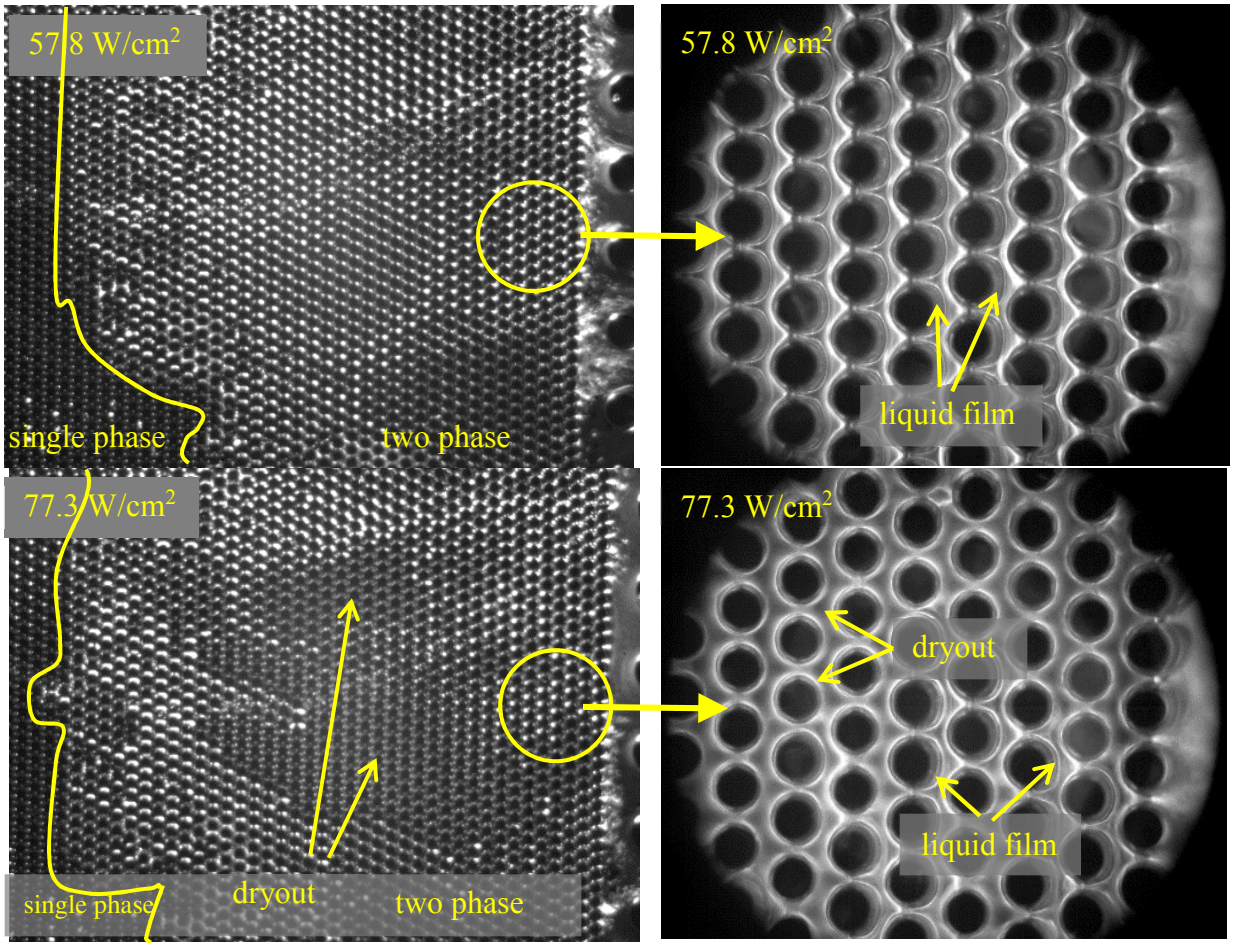

Figure 15 Flow visualization of dense device at G_{max} = 300 kg/m²s, T_{in} = 55 °C

Figure 16 illustrates how upstream bubbles expand and move spanwise. Bubble 1 starts to appear at t = 0.73 ms, and travels in transverse direction until t = 2.44 ms. At t = 3.65 ms, Bubble 1 shows tendency to merge with the bubble in the adjacent downstream row, which occurs from t = 4.39 ms to t = 5.13 ms. A tiny bubble is left after the two bubbles merge as seen from t = 5.61 ms to t = 7.32 ms. Bubble 2 starts to travel in transverse direction at t = 21.22 ms. At t = 23.90 ms, Bubble 2 is elongated and starts to break. At t = 24.39 ms, Bubble 2 breaks into two short bubbles, and one of them travels in transverse direction until out of range of the lens scope at t = 27.32 ms. Other bubbles also move or expand in transverse direction, like Bubble 3 and Bubble 4.

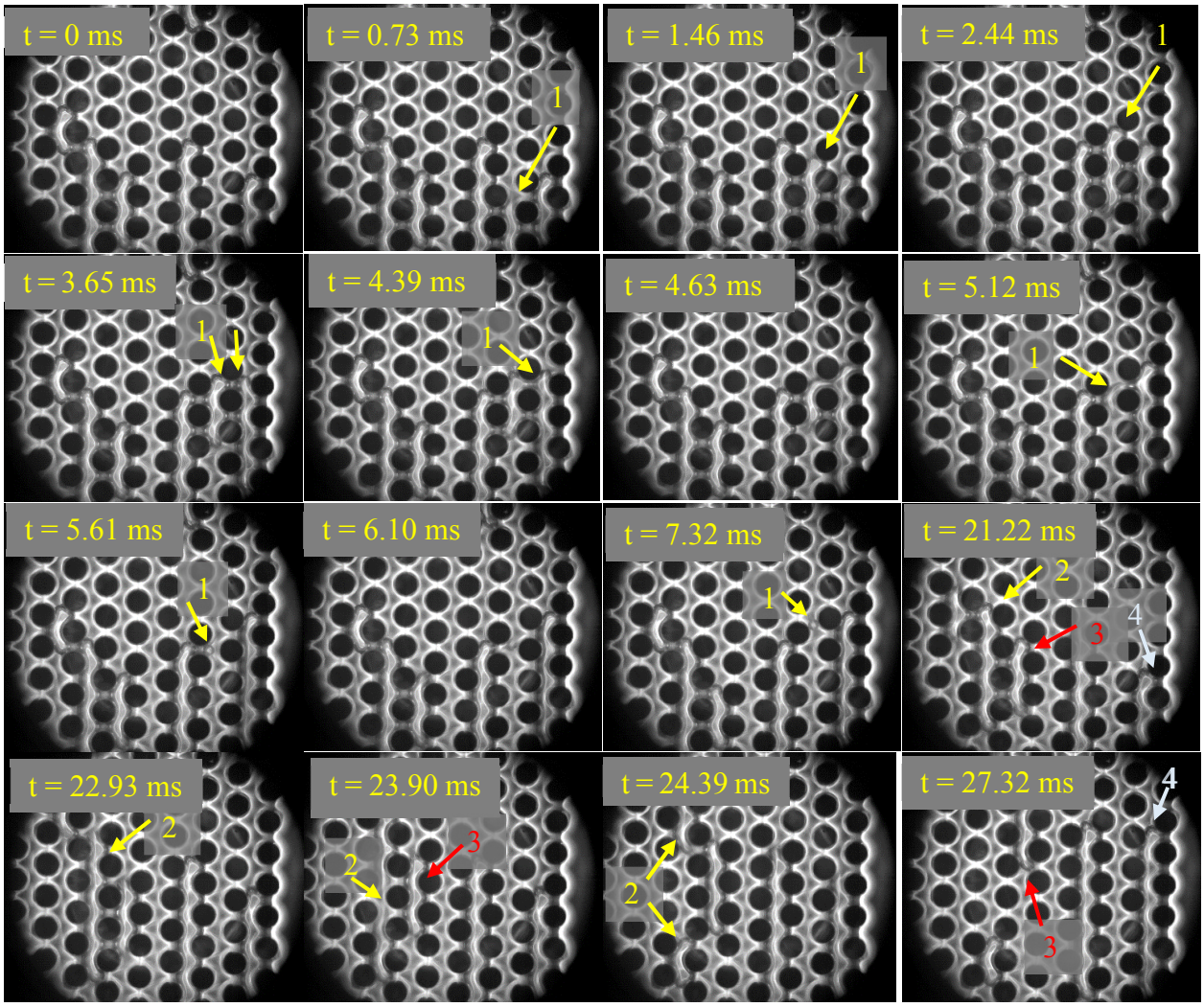

Figure 16 Flow visualization of dense device at G_{max} = 300 kg/m^{2}s, T_{in} = 30 ºC, q_{eff}" = 9.9 W/cm^2

Figure 17 shows flow visualization of dense device at G_{max} = 865 kg/m^{2}s, and T_{in} = 80 ºC. Liquid surrounding circular pins is seen in the zoomed in images for all heat flux conditions, which indicates no change in flow pattern in the tested heat fluxes range. Similar flow patterns are observed for testing conditions when G_{max} = 865 kg/m^{2}s, T_{in} = 30 and 55 ºC. This results in a weak dependence of local two phase heat transfer coefficients on heat flux.

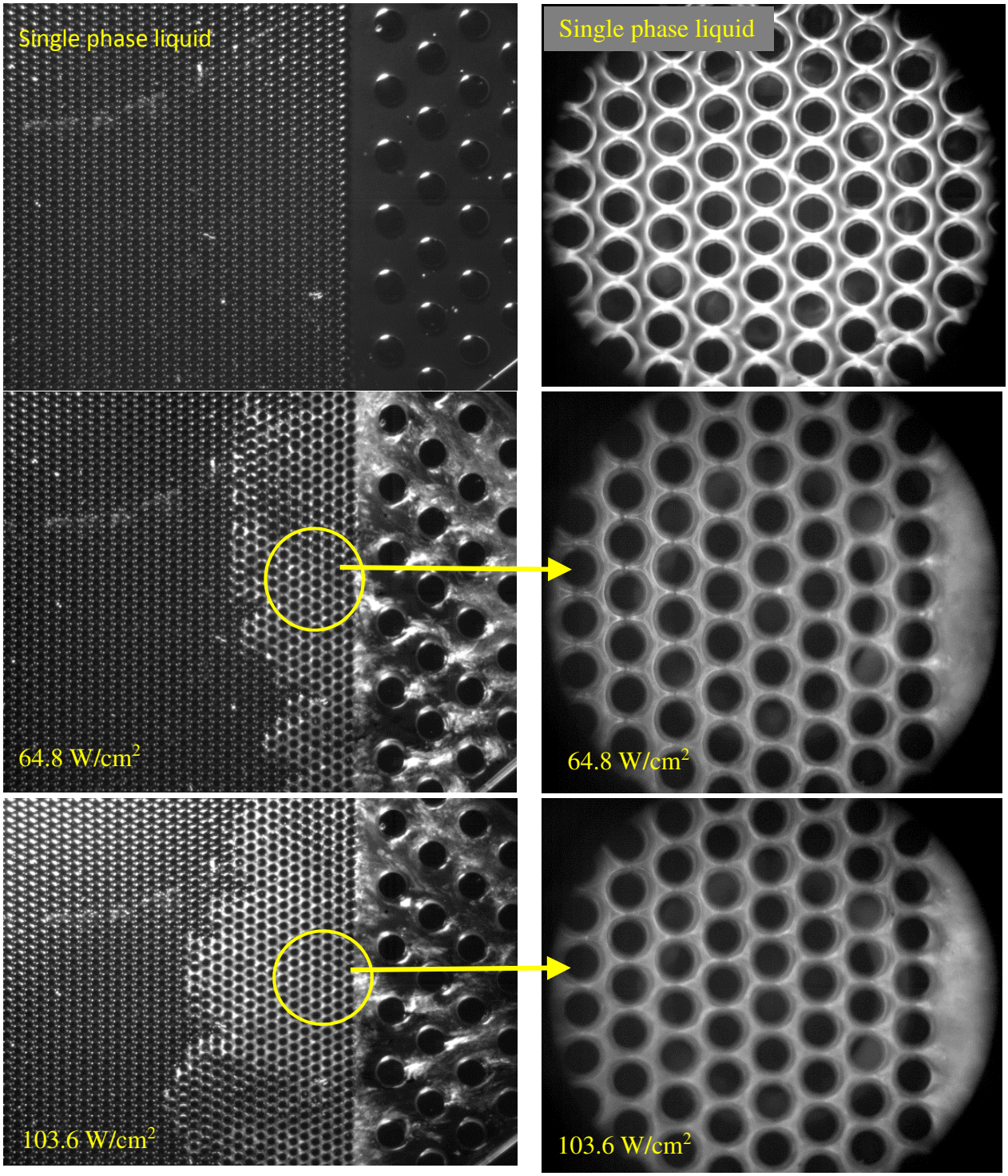
Single phase liquid
Single phase liquid
64.8 W/cm2
64.8 W/cm2
103.6 W/cm2
103.6 W/cm2

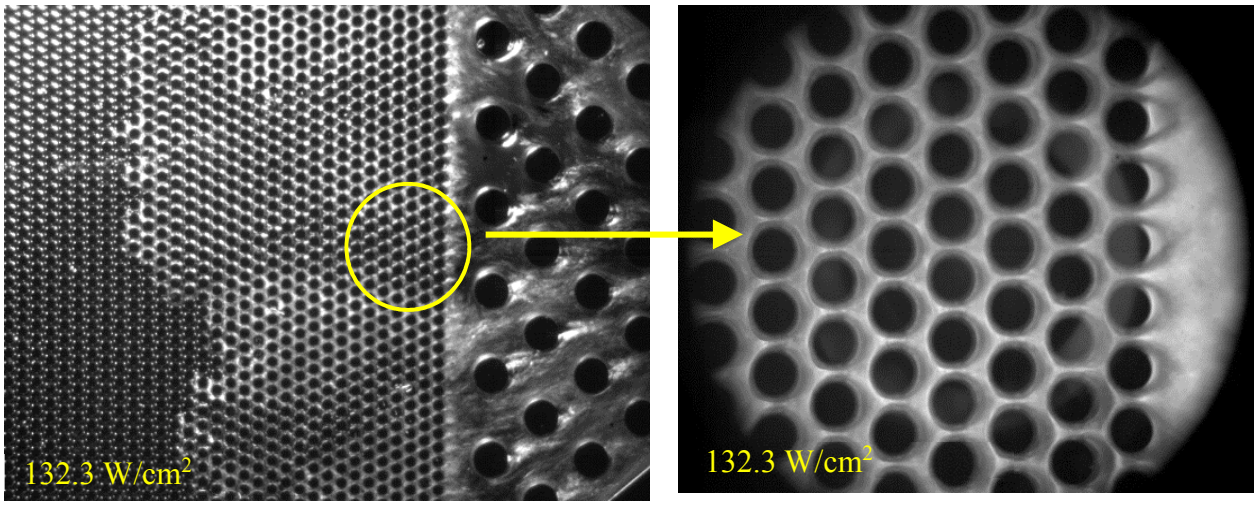

Figure 17 Flow visualization of dense device at G_{max} = 865 kg/m^{2}s, T_{in} = 80 °C

At the same mass flux, and the same heat flux, higher inlet fluid temperature yields a larger boiling area. For dense device with G_{max} = 865 kg/m^{2}s and q_{eff} "= 136 W/cm^2, Figure 18 compares boiling area when inlet fluid temperature is 55 °C and 80 °C. The boiling area for T_{in} = 80 °C is almost twice that for T_{in} = 55 °C.

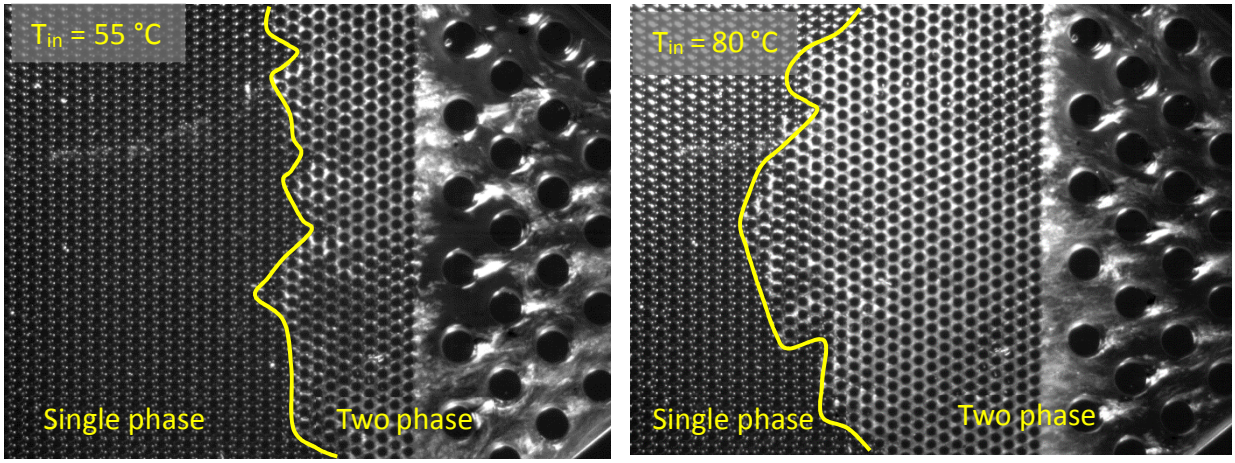

Figure 18 Flow visualization of dense device at G_{max} = 865 kg/m^{2}s, q_{eff} "= 136 W/cm^2

3.2.2 Flow Regime Map

As discussed in previous section, unlike traditional macro scale two phase flow patterns, bubbly flow, slug flow, or annular flow are not observed from flow visualization. Boiling occurs in a concentrated area close to microgap outlet, and boiling area becomes large and expands to microgap inlet as heat flux increases. The zoomed in images reveal that liquid films always surround pin fins, which are inside boiling area unless dryout occurs. For both sparse and dense devices, liquid films of adjacent pin fins can be connected at low heat flux, and become separated liquid films as heat flux increases. For sparse device, bubbles nucleated inside liquid films at rear side of pin fins are observed when heat flux is further increased. The liquid films are also stretched to wakes with sharp tails. For dense device, bubble nucleation inside liquid films and wakes with sharp tails are not observed due to confined space. Liquid films are offset to downstream at increased heat flux although wakes with sharp tails are not able to form.

A flow regime map is developed in Figure 19 using Re_l and Re_v, as in [13]. Re_l and Re_v are liquid and vapor phase Reynolds number which are defined as

$$Re_l = \frac{G_{max}(1-x)D}{\mu_l} \tag{19}$$

$$Re_v = \frac{G_{max}xD}{\mu_v} \tag{20}$$

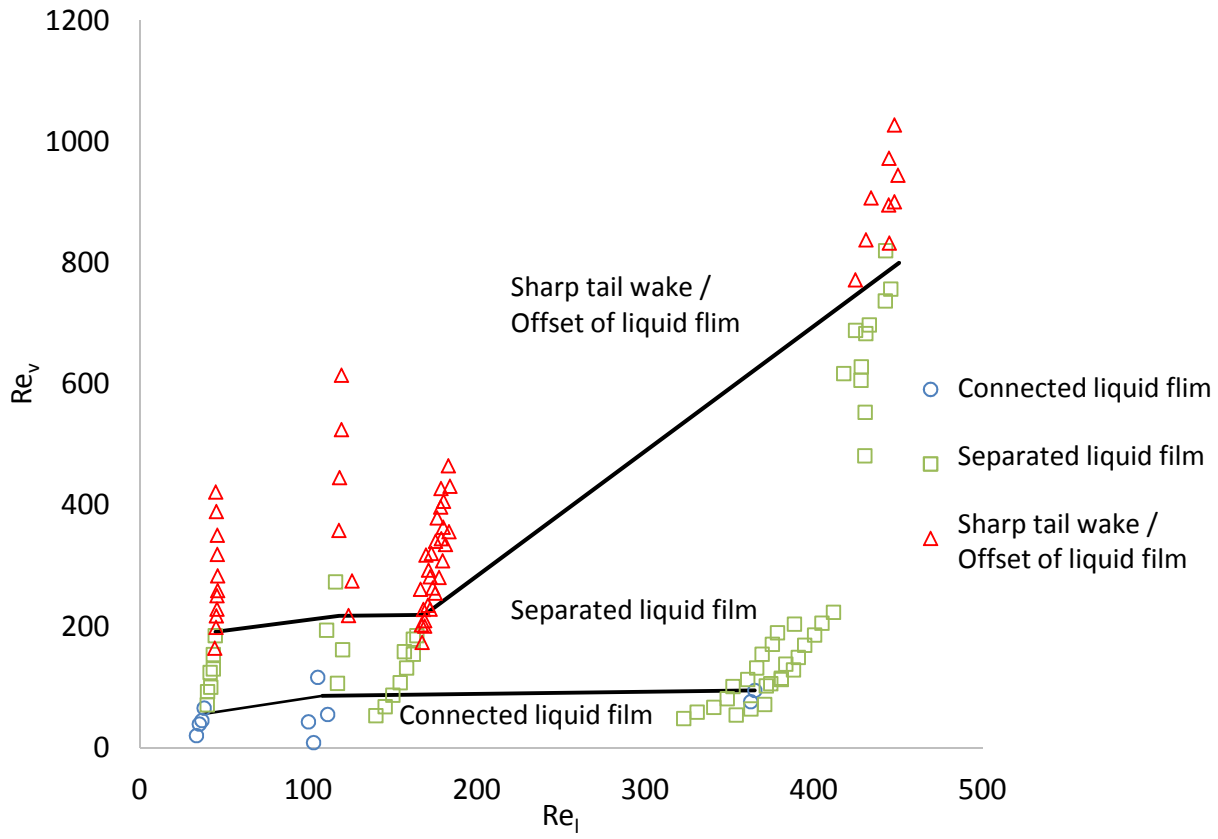

Figure 19 Flow regime map

3.2.3 Two Phase Flow Results

For certain mass flux and heat flux conditions, unstable boiling was observed. The results reported in this section are for conditions when stable two phase flow was observed inside the pin fin area. Figure 20 and Figure 21 present the pressure drop for sparse device and dense device, respectively. Pressure drop generally increased with heat flux and vapor quality. At the same vapor quality, higher mass flux yields higher pressure drop. For sparse device at the same mass flux, subcooled inlet fluid temperature yields higher pressure drop than near saturated or saturated inlet conditions at the same vapor quality due to the fact that lower fluid temperature results in higher dynamic viscosity in both liquid and vapor phases. For dense device, higher inlet fluid temperature

results in higher pressure drop. The boiling area is larger for higher inlet fluid temperature, causing higher frictional pressure drop in vapor phase.

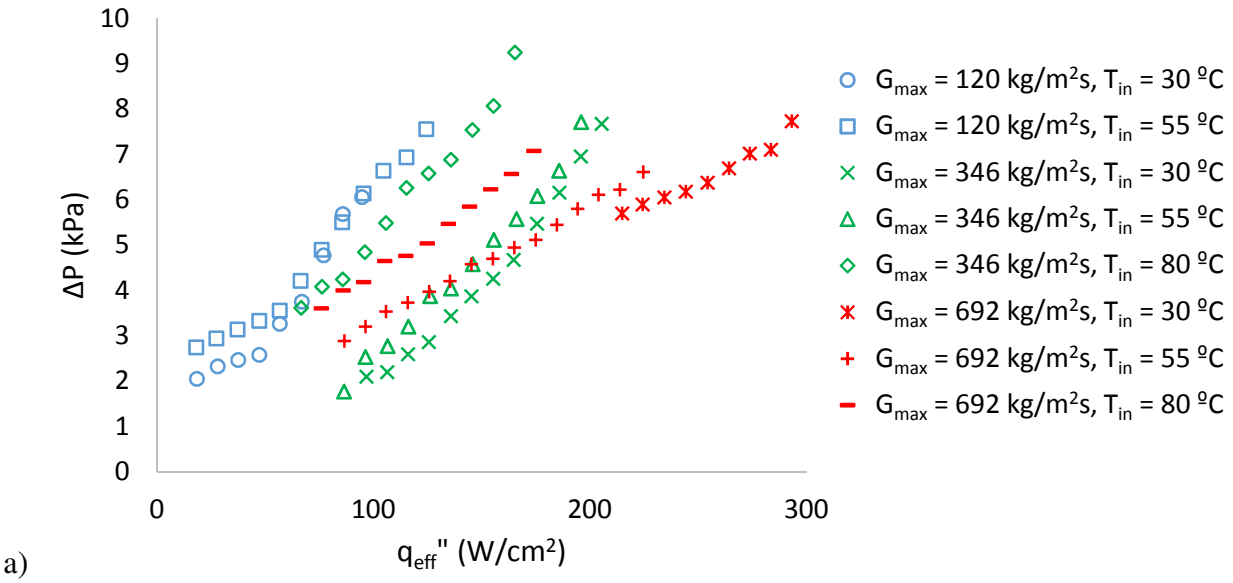

a)

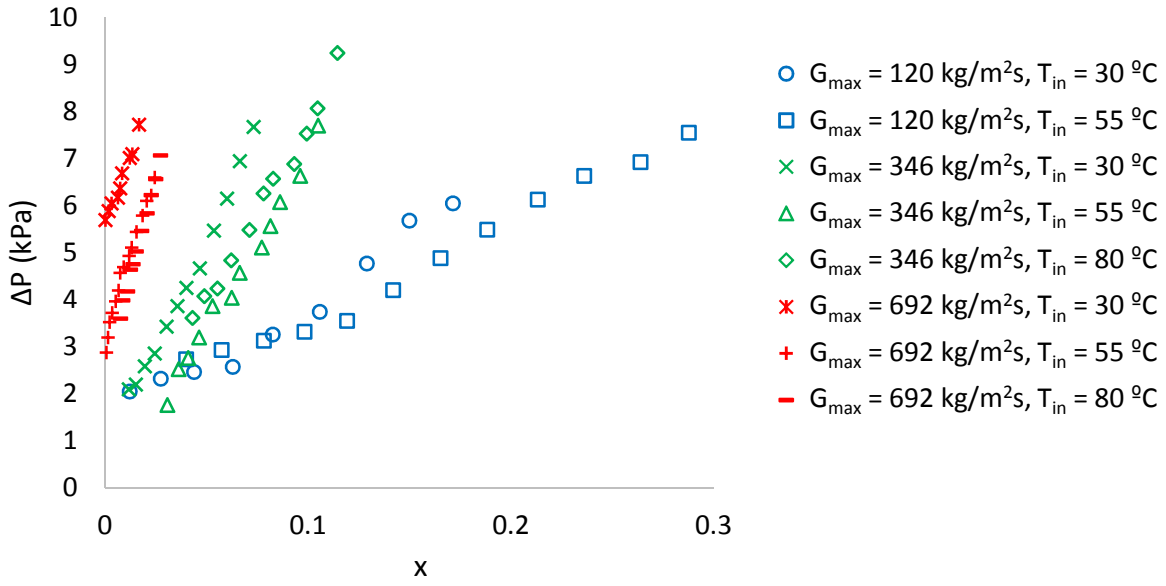

b)

Figure 20 Sparse device: a) pressure drop vs heat flux; b) pressure drop vs. exit vapor quality

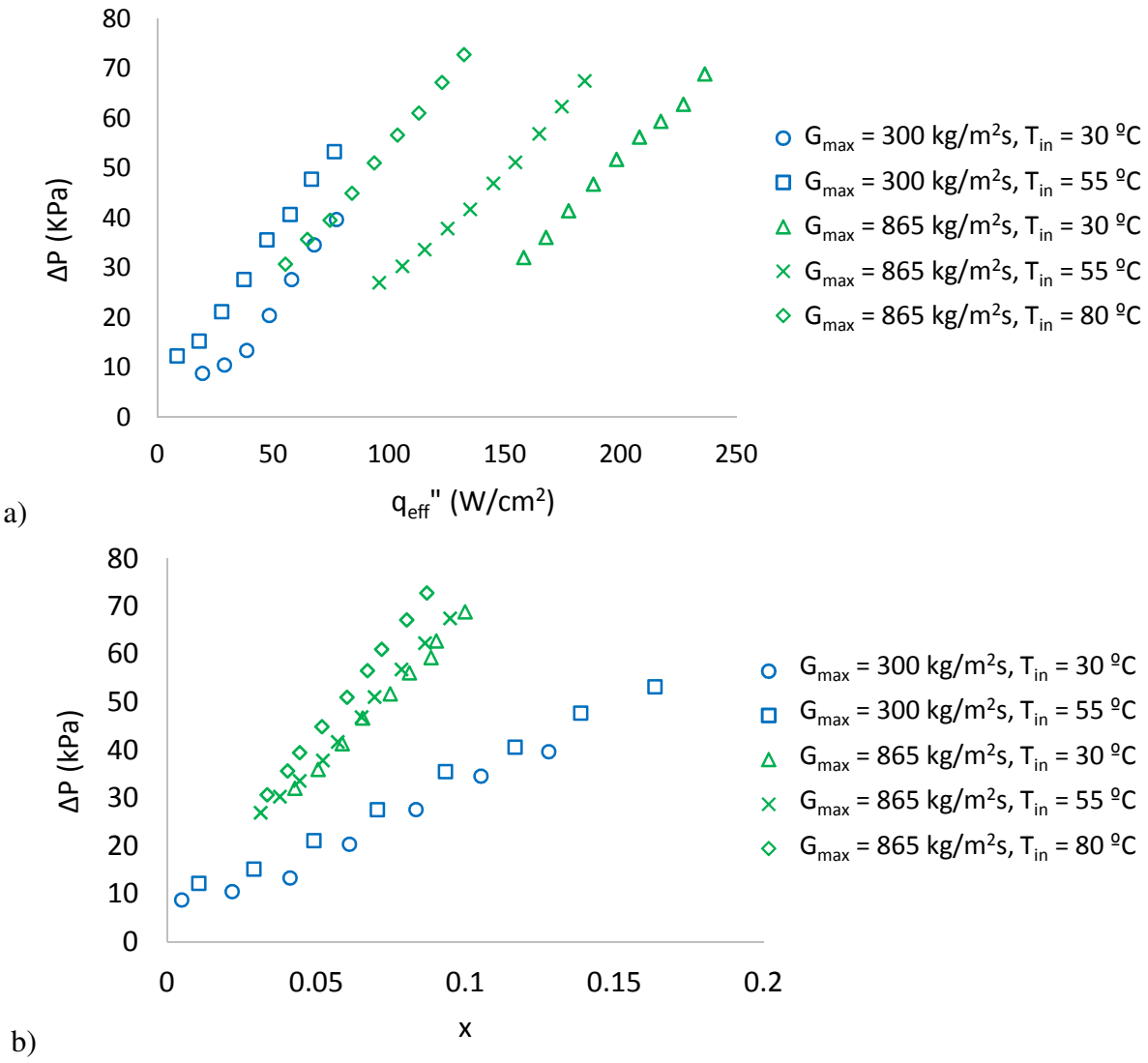

Figure 21 Dense device: a) pressure drop vs heat flux; b) pressure drop vs. vapor quality

Device exit pressure increases with heat flux because increased pressure drop along tubing between device exit and condenser due to increased vapor quality and vapor phase acceleration. Condenser pressure is nearly fixed because the temperature of coolant supplied by thermostatic bath circulator is nearly fixed, and condensed fluid temperature is in the range of 10 ºC to 20 ºC. The condenser saturation pressure variation due to the variation in fluid temperature is negligible. Figure 22 shows the saturation pressure in the last quarter of pin fin array close to device exit.

Although exit pressure started below atmospheric pressure, it eventually increased to as high as 150 kPa. Higher inlet fluid temperature results in higher saturation pressure for same mass flux.

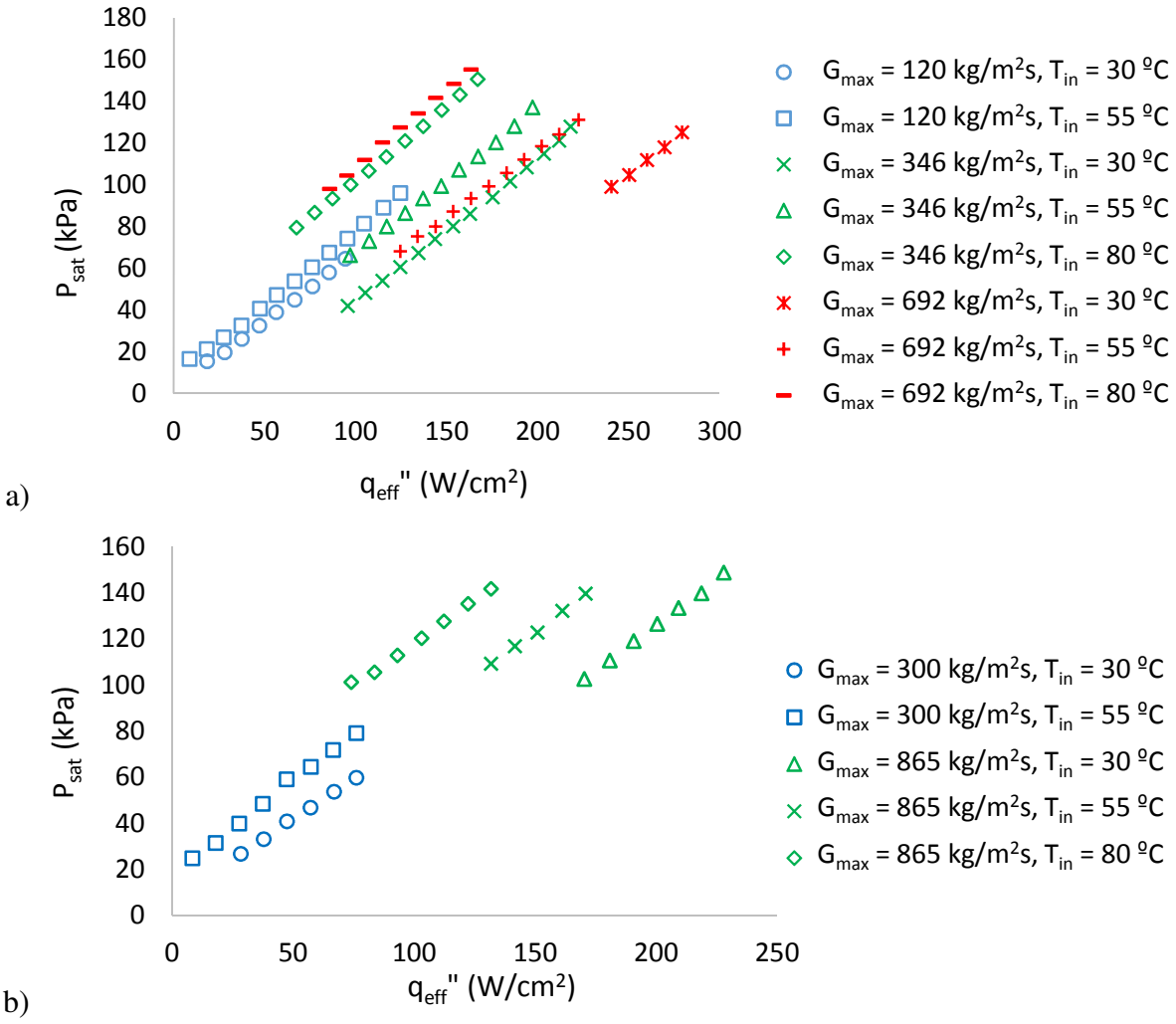

Figure 22 Saturation pressure: a) sparse device; b) dense device

Figure 23 shows exit vapor quality for both devices at all tested conditions. The highest exit vapor quality achieved for sparse device and dense device are 0.28 and 0.18 at lowest tested mass flux, respectively. Higher inlet fluid temperature results in higher exit vapor quality, because there is less sensible heating for higher inlet fluid temperature. Exit vapor quality decreases with mass flux at same heat flux which is expected.

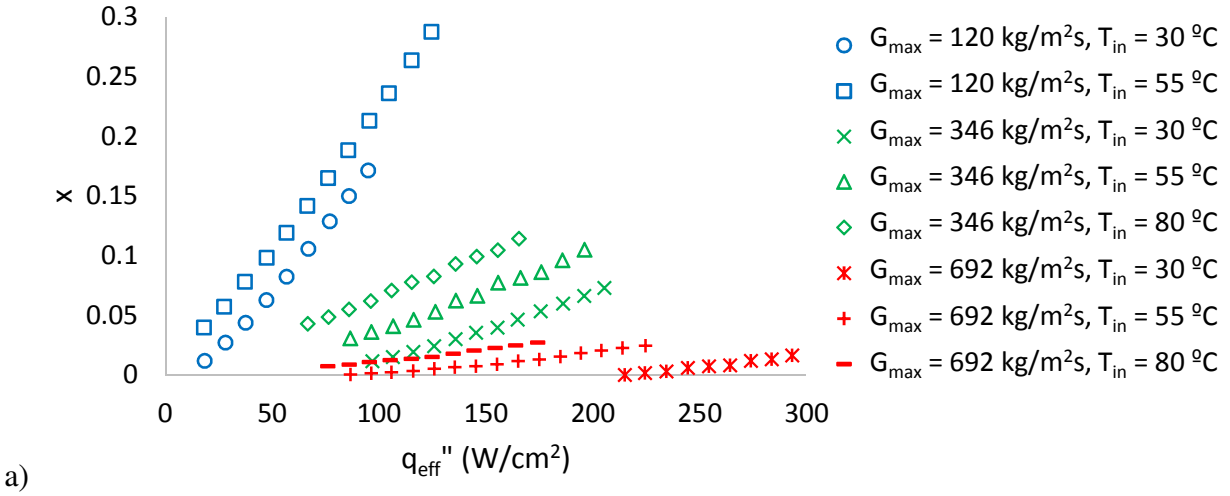

a)

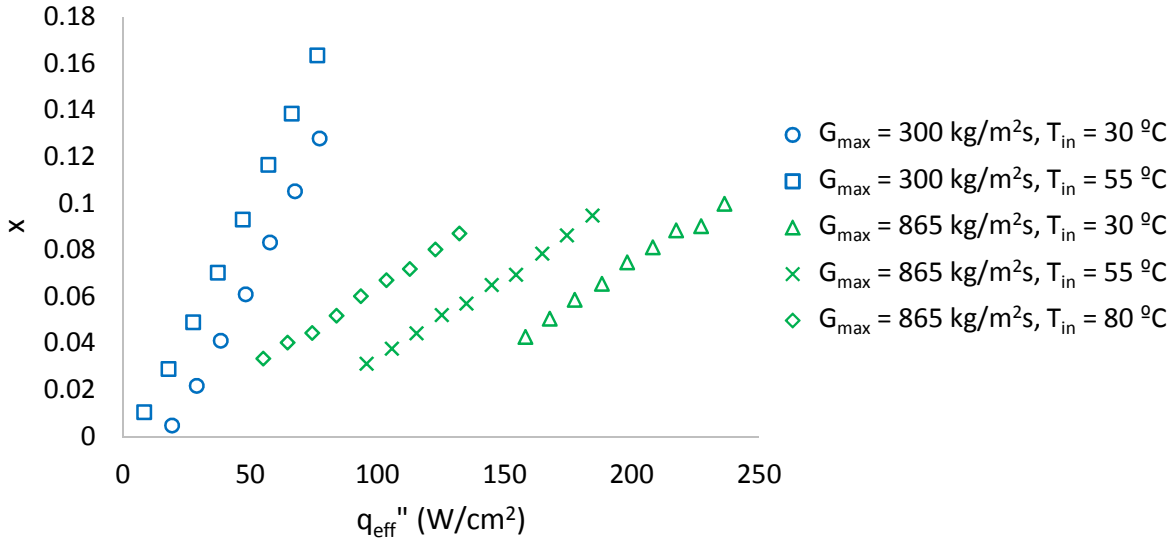

b)

Figure 23 Exit vapor quality: a) sparse device; b) dense device

Wall temperatures in the last quarter of pin fin array close device exit when two phase flow completely covers this area are plotted in Figure 24. For both sparse and dense devices at their lowest mass fluxes, and sparse device at G_{max} = 346 kg/m^{2}s and T_{in} = 30 ºC, local dryout was observed. This leads to a slight change of slope in the $T_{w,tp}$ vs. q_{eff}" curve, as shown in Figure 24. For other mass flux and inlet fluid temperature conditions of both sparse and dense devices, wall temperature in two phase region increases with heat flux linearly and at approximately the same

slope. This indicates two phase flow under these conditions is in the same flow regime, as discussed in previous section. There is a noticeable slope change in boiling curves for conditions when dryout was observed, as shown in Figure 25. Critical heat flux was reached for both sparse and dense devices at their lowest mass fluxes. For other test conditions, no critical heat fluxes were observed before heater temperatures reached 130 ºC.

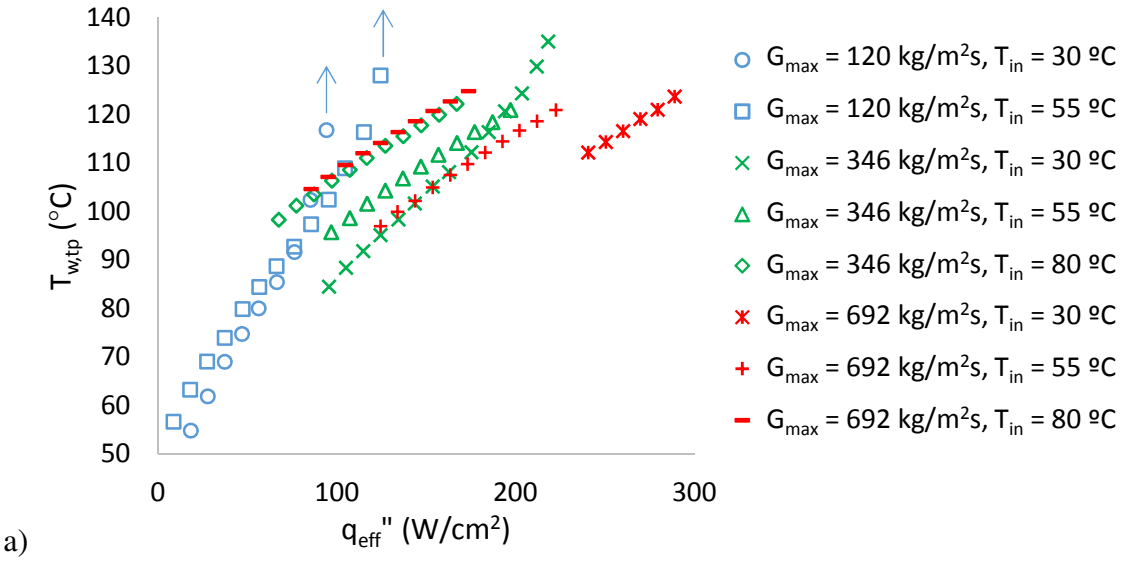

a)

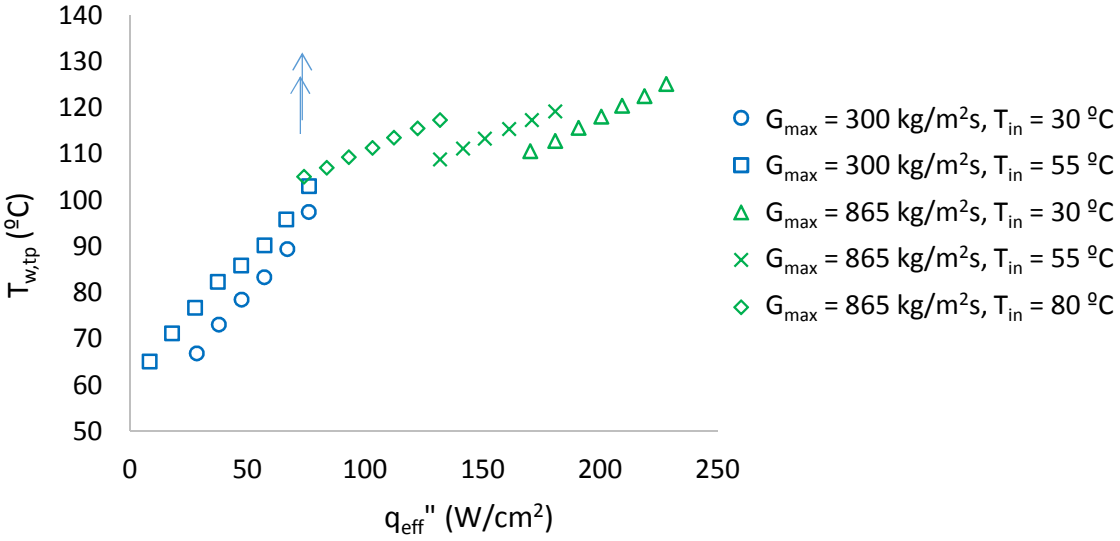

b)

Figure 24 Wall temperature: a) sparse device; b) dense device

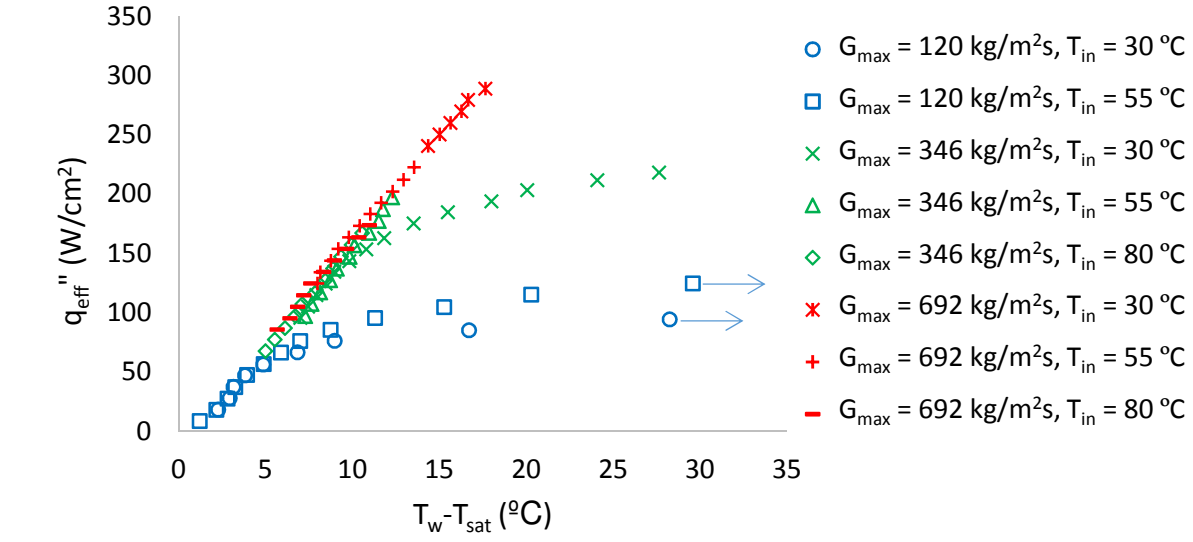

a)

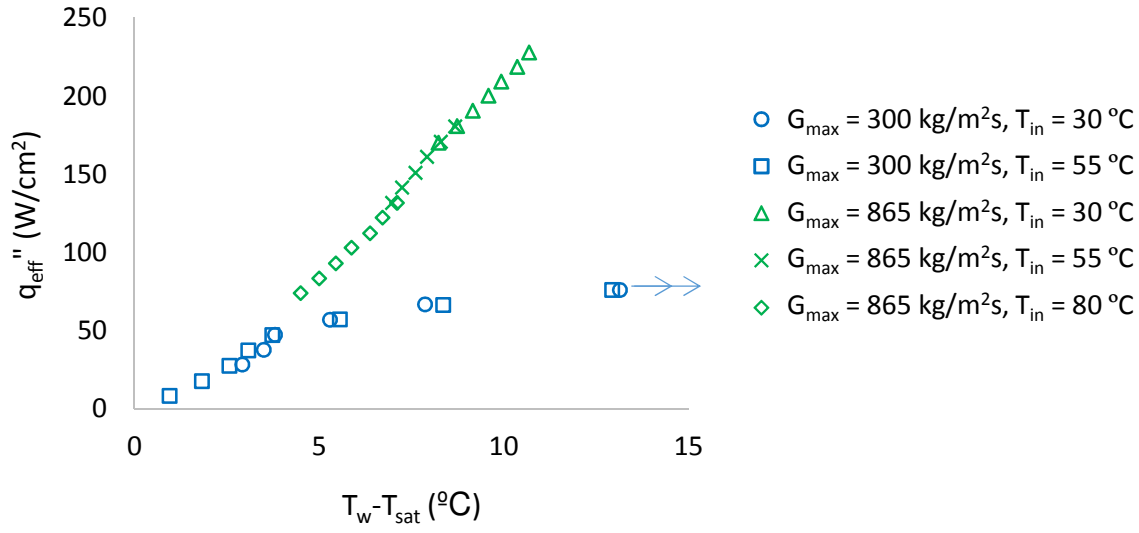

b)

Figure 25 Boiling curve: a) sparse device; b) dense device

Local wall temperatures are compared for both devices at volume flow rate of 26 mL/min in Figure 26, which yields a mass flux of 120 kg/m^{2}s for sparse device, and 300 kg/m^{2}s for dense device. The wall temperatures are evaluated at the location of the last heater close to device exit. At the same heat flux, wall temperatures are in the same range for both devices, except the case T_{in} = 30 °C for sparse device when dryout is observed. However, the averaged wall temperature

evaluated with all four heaters of sparse device is higher than that of dense device at the same heat flux. Two examples are given in Figure 27. Figure 27 shows wall temperatures at all heater locations, when VFR = 26 mL/min, and at highest heat fluxes achieved for T_{in} = 30 °C and 55 °C. The average wall temperatures are 122.7 °C and 115.6 °C for sparse and dense devices, respectively, for T_{in} = 55 °C, and are 123.0 °C and 108.8 for sparse and dense devices, respectively, for T_{in} = 30 °C. Thus dense device outperforms sparse device in terms of wall temperatures. The wall temperature difference along flow direction of sparse device is smaller than that of dense device, as seen in Figure 27. In other words, sparse device provides better wall temperature uniformities than dense device. The wall temperature difference of sparse device and dense device are 12 °C and 33 °C, respectively, for T_{in} = 55 °C, and are 30 °C and 49 °C, respectively, for T_{in} = 30 °C. Higher inlet fluid temperature also results in better wall temperature uniformity. Therefore, at the same mass flow rate and heat flux, dense device offers lower average wall temperature, and sparse devise offers better wall temperature uniformity. Besides, the pressure drop of sparse device is lower than that fo dense device, as discussed earlier.

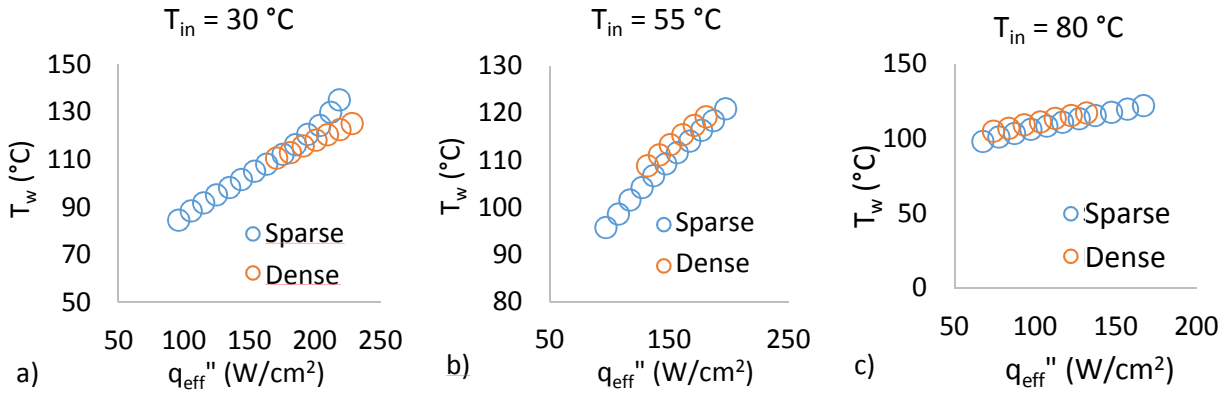

Figure 26 Comparison of wall temperature of sparse and dense devices at VFR = 26 mL/min: a) T_{in} = 30 °C; b) T_{in} = 55 °C; and c) T_{in} = 80 °C

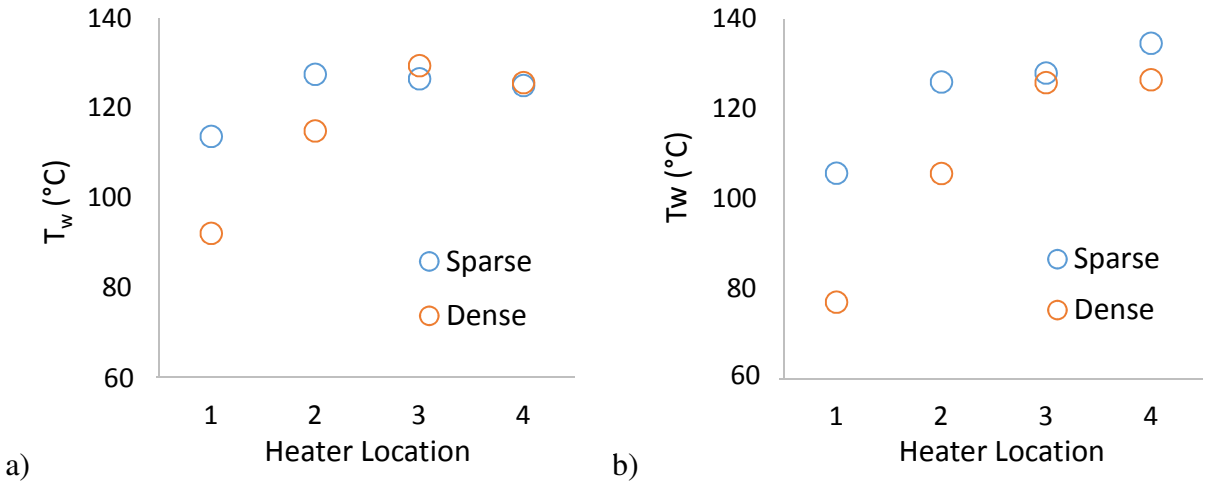

Figure 27 Comparison of temperature difference along flow direction at VFR = 26 mL/min: a) T_{in} = 55 °C, q_{eff}" = 185 W/cm^2; b) T_{in} = 30 °C, q_{eff}" = 227 W/cm^2

Local two phase heat transfer coefficient is calculated when the last quarter of pin fin array is completely in two phase flow, and local heater temperature closest to device exit was used. The results are presented in Figure 28 for sparse device, and in Figure 29 for dense device. For test conditions involving local dryout, local two phase heat transfer coefficient first increases and then decreases with heat flux. For other test conditions, two phase heat transfer coefficient generally increases with heat flux, and the dependence is not as significant as in test conditions involving local dryout. Lower inlet fluid temperatures result in higher two phase heat transfer coefficient.

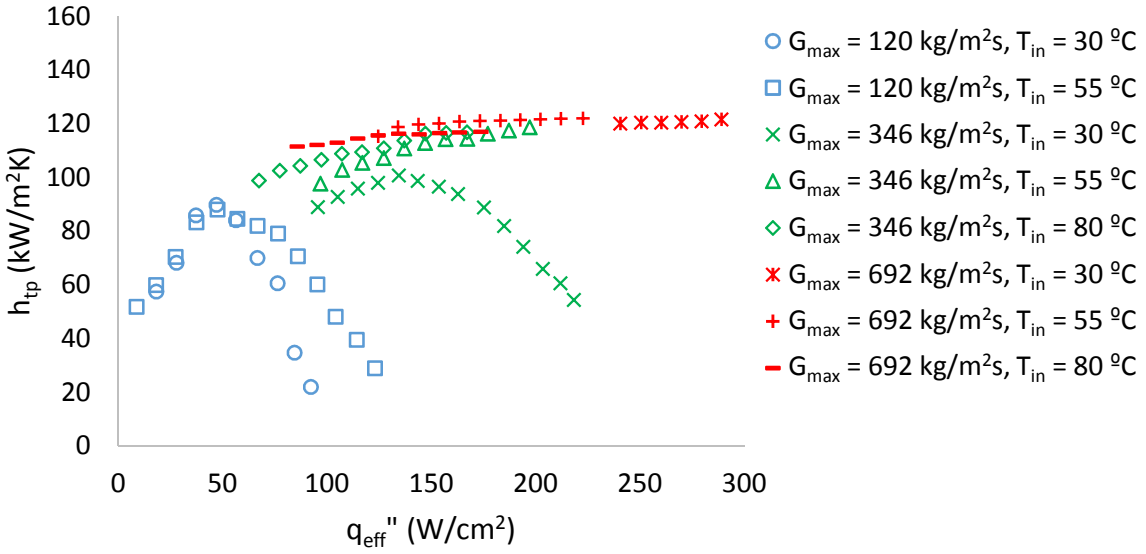

a)

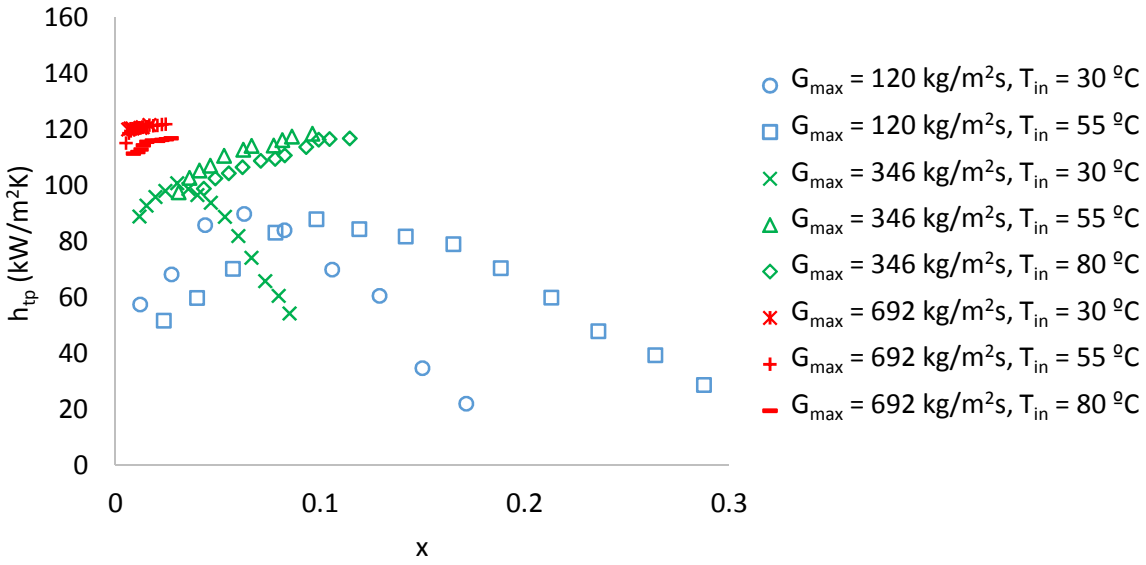

b)

Figure 28 Local two phase heat transfer coefficient for sparse device: a) h_{tp} vs. q_{eff}"; b) h_{tp} vs. x

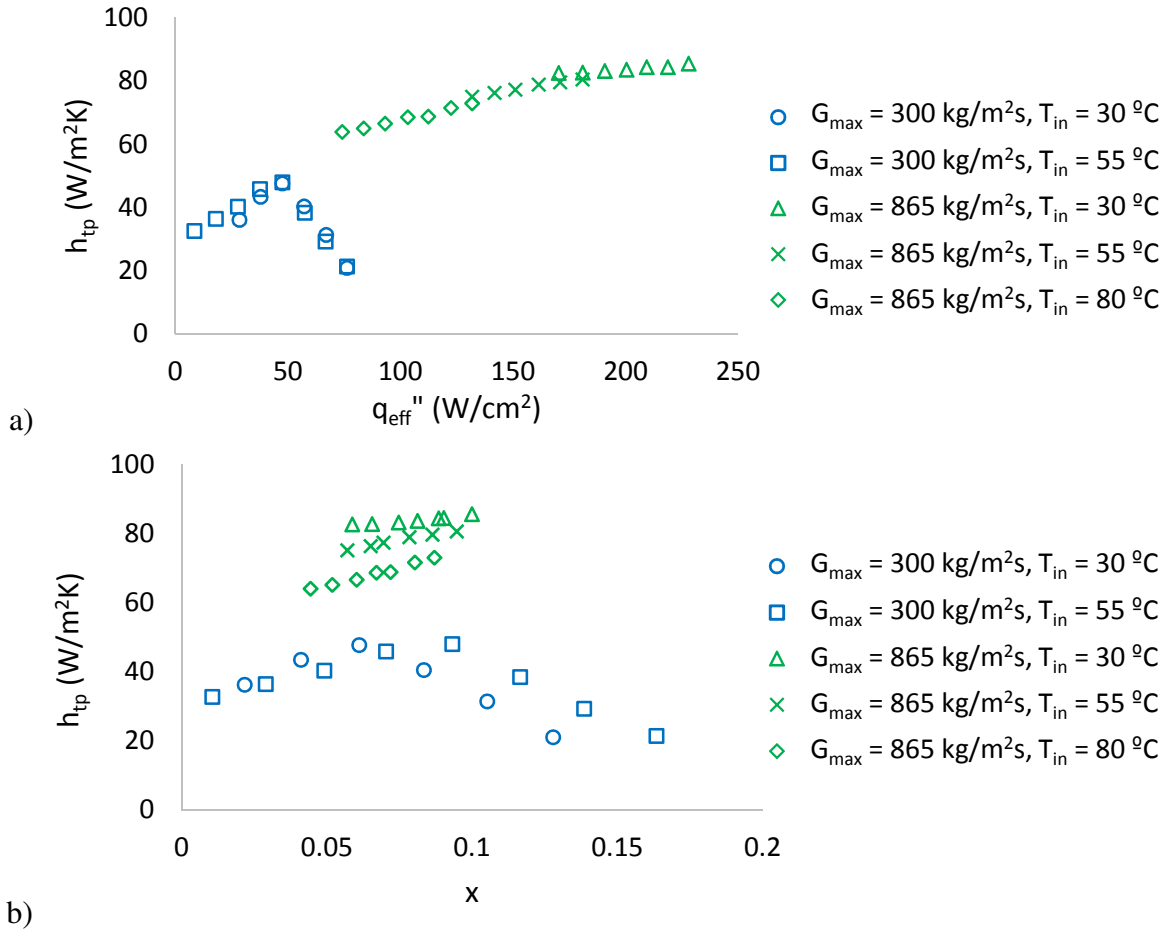

Figure 29 Local two phase heat transfer coefficient for dense device: a) h_{tp} vs. q_{eff}"; b) h_{tp} vs. x

For dense device at G_{max} = 865 kg/m^{2}s, boiling covers less than 3/4 of pin fin array for all tested heat fluxes and inlet fluid temperature conditions. The first quarter of pin fin array close to device inlet is always in single phase. The single phase heat transfer coefficients are calculated for the first quarter of pin fin array, and compared to two phase heat transfer coefficients for the last quarter of pin fin array close to device exit in Figure 30. The heat transfer coefficient is improved by up to 105% when fluid travel from single phase region to two phase region.

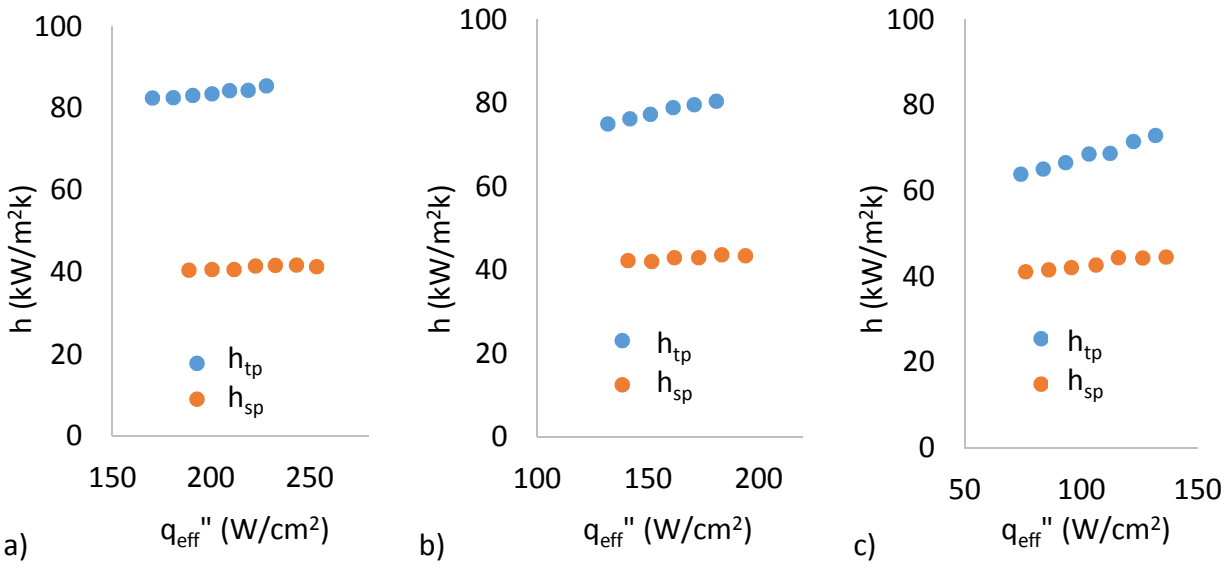

Figure 30 Comparison of h_{sp} and h_{tp} for dense device at G_{max} = 865 kg/m²s: a) T_{in} = 30 °C; b) T_{in} = 55 °C; c) T_{in} = 80 °C;

3.2.4 Two Phase Heat Transfer Coefficient Correlations

Two phase heat transfer coefficient correlations for two phase flow in micro scale pin fin array are available in literature. Qu and Siu-Ho developed a two phase heat transfer coefficient correlation based on inline square shape copper pin-fin [15]. They derived their correlation from their experimental work of flow boiling at different levels of inlet fluid subcooling, and their correlations requires an inlet subcooling term in the form of negative inlet quality x_{in}. The Qu and Siu-Ho two phase heat transfer coefficient correlation is

$$h_{tp} = 1.0 - 12.2 \cdot x_{in}\exp[-(101 \cdot x_{in} + 29.4) \cdot x_e]h_{tp,eq} \tag{21}$$

where $h_{tp,eq}$ represents heat transfer coefficient in high exit vapor quality x_e region for a near saturated inlet temperature condition, and takes a constant value of 50.44 kW/m²K. Two phase

heat transfer coefficients in their work decreases with heat flux and vapor quality, and thus this is not suitable for current study.

Krishnamurthy and Peles developed their two phase heat transfer coefficient using staggered silicon circular shape pin with D.I. water[13]. The tested heat fluxes and mass fluxes ranges are also close to current study. In their correlation, two phase heat transfer coefficient is modified from single phase heat transfer coefficient

$$h_{tp} = F h_{sp} \tag{22}$$

and

$$F = \zeta(\phi_l^2)^{0.2475} Pr^{0.333} \tag{23}$$

ζ is constant, and $\zeta = 1.4$. The frictional multiplier ϕ_l^2 is

$$\phi_l^2 = 1 + \frac{C}{X_{vv}} + \frac{1}{X_{vv}^2} \tag{24}$$

where C=0.24 is an empirically determined constant. The Martinelli parameter is defined as

$$X_{vv} = \left[\frac{(dP/dz)_l}{(dP/dz)_v}\right]^{1/2} \tag{25}$$

$(dP/dz)_l$ and $(dP/dz)_v$ are frictional pressure gradients for liquid and vapor phases flowing alone, respectively, and can be calculated from

$$\left(\frac{dP}{dz}\right)_l = \frac{fG^2(1-x)^2}{\rho_l D} \tag{26}$$

$$\left(\frac{dP}{dz}\right)_z = \frac{fG^2x^2}{\rho_v D} \tag{27}$$

The friction factor is

$$f = 63.246 Re_D^{-0.7797} \tag{28}$$

Single phase heat transfer coefficient is evaluated from

$$Nu_{sp} = 0.76\left(\frac{S_T}{D}\right)^{0.16}\left(\frac{S_L}{D}\right)^{0.2}\left(\frac{H_f}{D}\right)^{-0.11} Re^{0.33}Pr^{0.33} \tag{29}$$

and

$$h_{sp} = \frac{Nu_{sp} \cdot k_f}{D} \tag{30}$$

All fluid properties are evaluated at saturation condition.

Reeser et al. modified two phase heat transfer coefficient correlation developed by Krishnamurthy and Peles and proposed new correlations for water and HFE-7200, and for staggered and inline square shape pin fin, respectively. The correlation for water in staggered pin fin device is

$$h_{tp} = \zeta\left(\phi_l^2\right)^{0.2475} h_{sp} \tag{31}$$

where

$$\zeta = -0.07exp(4.3 \cdot x) + \left(\frac{80}{G_{max} + 2965}\right)^{1/2} \tag{32}$$

They used a different correlation for single phase Nusselt number

$$Nu_{sp} = 0.0413\left(\frac{S_T}{D}\right)^{0.2}\left(\frac{S_L}{D}\right)^{0.2}\left(\frac{H_f}{D}\right)^{0.25} Re^{0.6} Pr^{0.36}\left(\frac{Pr}{Pr_w}\right)^{0.25} \tag{33}$$

Other parameters are kept same as in Krishnamurthy and Peles' correlation.

The predicted two phase heat transfer coefficients using correlations developed by Krishnamurthy and Peles, and Reeser et al are compared with present experimental results where no dryout occurred. All the predicted two phase heat transfer coefficients are smaller than present experimental results, and h_{tp} predicted using Krishnamurthy and Peles' correlation are closer to present experimental results than Reeser et al's correlation, as shown in Figure 31. The predictions overlap for same mass flux at the same vapor quality, especially when using Reeser et al's correlation. These correlations are not sensitive to inlet fluid temperature, which is because they were developed from data without variation of inlet subcooling. A new two phase heat transfer correlation considering inlet subcooling is developed below. Since the Krishnamurthy and Peles' correlation provide better prediction, it is modified to include effects of inlet subcooling. The degree of inlet subcooling is included by using the term $\frac{C_P(T_{sat}-T_{in})}{h_{vap}}$. After multiple efforts, original correlation is modified to be

$$h_{tp} = F\left(\frac{S_T}{D}\right)^{037}\left(\frac{S_L}{D}\right)^{0.37}\left(\frac{C_P(T_{sat}-T_{in})}{h_{vap}}\right)^{0.05} h_{sp} \tag{34}$$

where

$$F = \zeta\left(\phi_l^2\right)^{0.2475} Pr^{0.333} \tag{35}$$

and $\zeta = 1.66$. Other parameter are the same as original correlation. The predicted h_{tp} is compared with experimental results in Figure 32. All the predicted data are bounded by $\pm 20\,\%$ of experimental data, and the mean absolute error is 6.2% as seen in Figure 33.

$$\text{MAE} = \frac{1}{M}\left(\frac{h_{tp,pred}-h_{tp}}{h_{tp}}\right)\times 100\% = 6.2\% \tag{36}$$

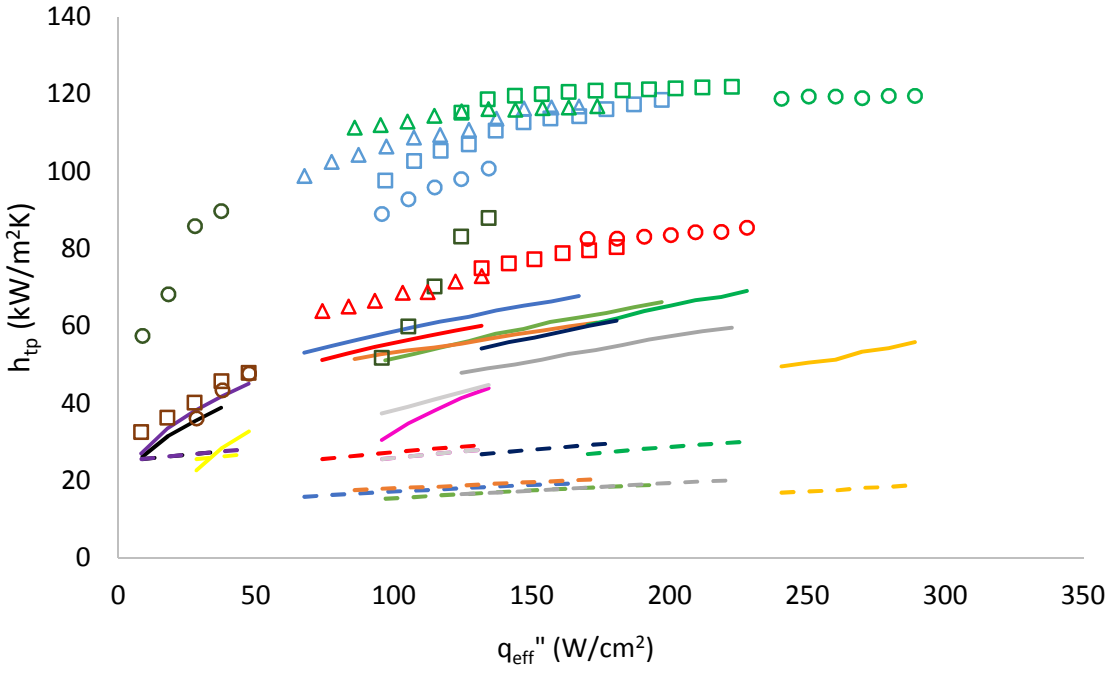

a)

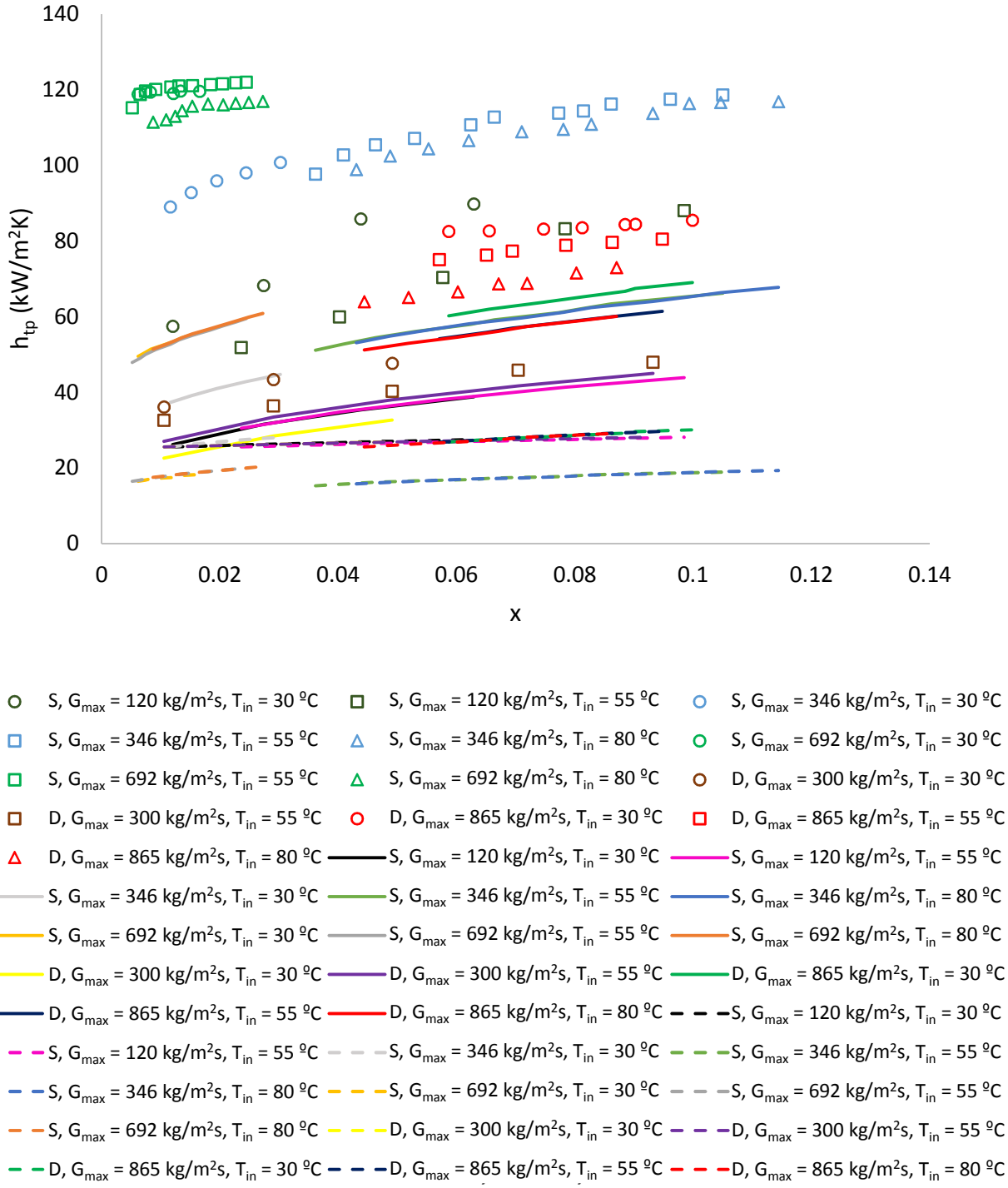

Figure 31 Comparison of h_{tp} with Correlations: a) h_{tp} vs q_{eff}"; b) h_{tp} vs x

——— Krishnamurthy and Peles - - - - Reeser et al S – Sparse D – Dense

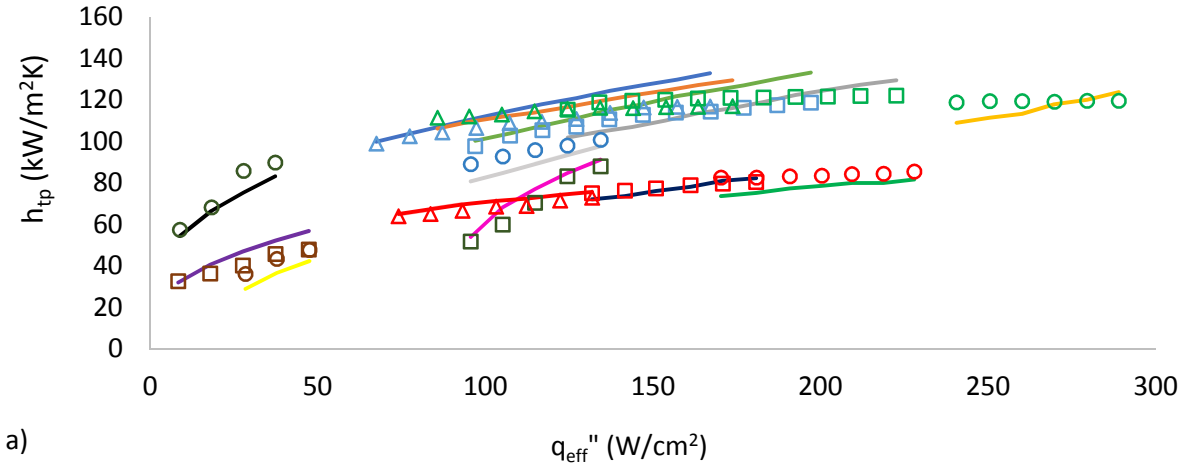

a)

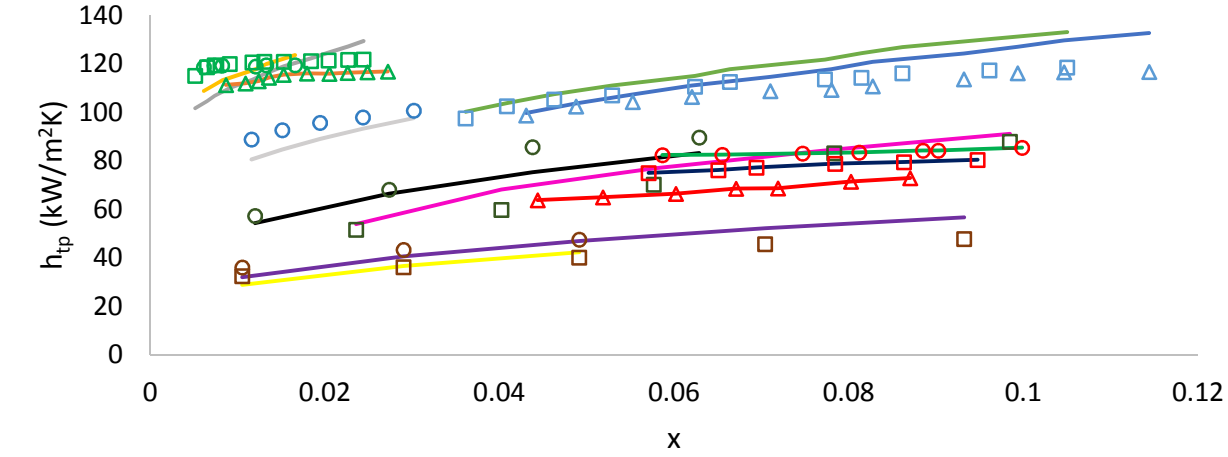

b)

S, G_{max} = 120 kg/m²s, T_{in} = 30 ºC
S, G_{max} = 120 kg/m²s, T_{in} = 55 ºC
S, G_{max} = 346 kg/m²s, T_{in} = 30 ºC
S, G_{max} = 346 kg/m²s, T_{in} = 55 ºC
S, G_{max} = 346 kg/m²s, T_{in} = 80 ºC
S, G_{max} = 692 kg/m²s, T_{in} = 30 ºC
S, G_{max} = 692 kg/m²s, T_{in} = 55 ºC
S, G_{max} = 692 kg/m²s, T_{in} = 80 ºC
D, G_{max} = 300 kg/m²s, T_{in} = 30 ºC
D, G_{max} = 300 kg/m²s, T_{in} = 55 ºC
D, G_{max} = 865 kg/m²s, T_{in} = 30 ºC
D, G_{max} = 865 kg/m²s, T_{in} = 55 ºC
D, G_{max} = 865 kg/m²s, T_{in} = 80 ºC
S, G_{max} = 120 kg/m²s, T_{in} = 30 ºC
S, G_{max} = 120 kg/m²s, T_{in} = 55 ºC
S, G_{max} = 346 kg/m²s, T_{in} = 30 ºC
S, G_{max} = 346 kg/m²s, T_{in} = 55 ºC
S, G_{max} = 346 kg/m²s, T_{in} = 80 ºC
S, G_{max} = 692 kg/m²s, T_{in} = 30 ºC
S, G_{max} = 692 kg/m²s, T_{in} = 55 ºC
S, G_{max} = 692 kg/m²s, T_{in} = 80 ºC
D, G_{max} = 300 kg/m²s, T_{in} = 30 ºC
D, G_{max} = 300 kg/m²s, T_{in} = 55 ºC
D, G_{max} = 865 kg/m²s, T_{in} = 30 ºC
D, G_{max} = 865 kg/m²s, T_{in} = 55 ºC
D, G_{max} = 865 kg/m²s, T_{in} = 80 ºC

Figure 32 Comparison of h_{tp} with new correlation: a) h_{tp} vs q_{eff}"; b) h_{tp} vs x

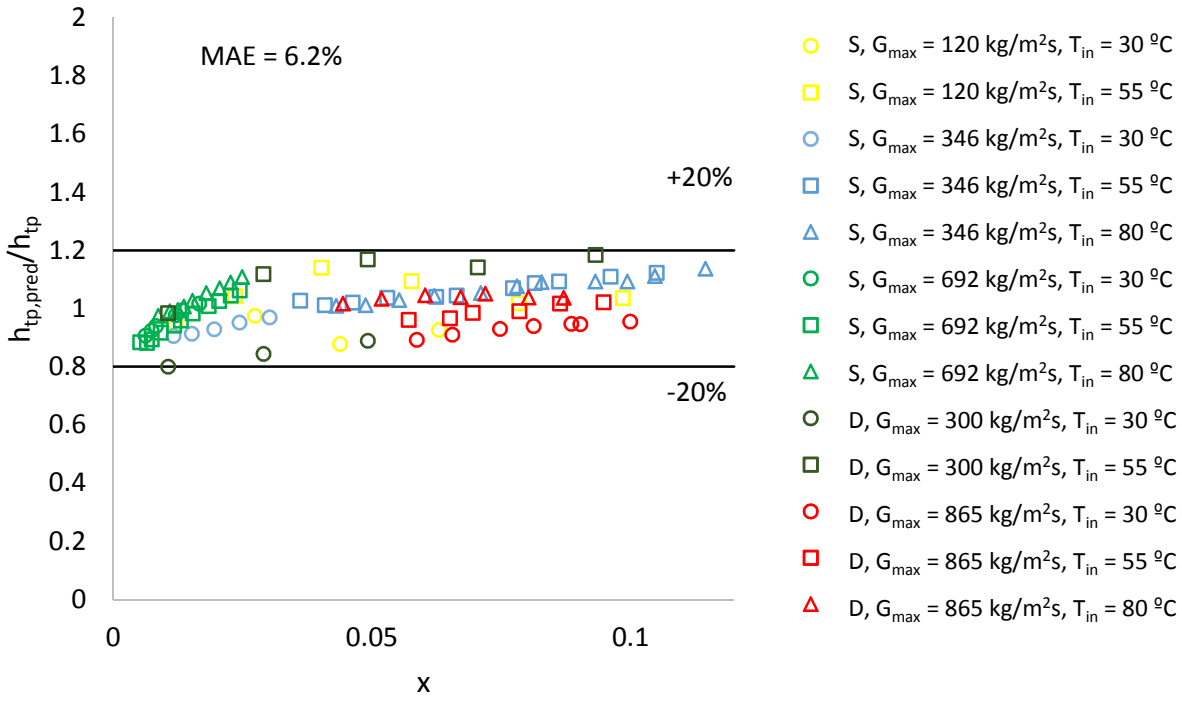

Figure 33 $h_{tp,pred}/h_{tp}$ vs. x

3.2.5 Two Phase Pressure Drop Correlations

The pressure drop includes two components, single phase pressure drop ΔP_{sub} and two phase pressure drop ΔP_{tp}.

$$\Delta P = \Delta P_{sub} + \Delta P_{tp} \tag{37}$$

The conventional pressure gradient evaluated from friction factor is

$$-\left(\frac{dP}{dz}\right)_{sub} = f\frac{G_{max}^2}{2\rho_l D} \tag{38}$$

Since this work studies pressure drop across a bank of pin fins, a slightly modified friction factor based on row number of pin fins is used

$$\Delta P_{sub} = \int -\left(\frac{dP}{dz}\right)_{sub} dz = \sum_{i=1}^{N_{tr}} f_{sp,i} \frac{G_{max}^2}{2\rho_l} \tag{39}$$

where N_{tr} is the row number of pin fins where single phase liquid flow and two phase flow transitions, and $f_{sp,i}$ is the friction factor evaluated at ith row of pins from inlet using $Re_i = G_{max}D/\mu_i$. The single phase friction factor is calculated from hydraulic tests for both sparse and dense devices using water and HFE-7200 (working fluid for Chapter 5) as shown in Figure 34, and

$$f_{sp} = 30\left(\frac{S_T}{D}\right)^{-1.18}\left(\frac{S_L}{D}\right)^{-1.18} Re^{-0.449} \tag{40}$$

Re is evaluated at average fluid temperature.

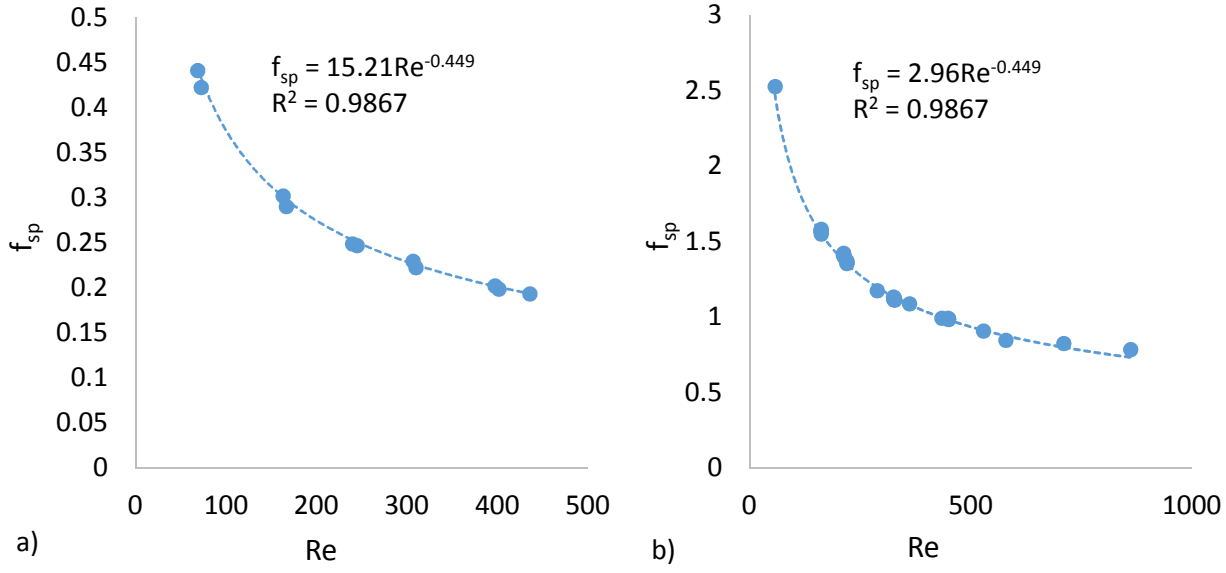

Figure 34 Single phase friction factor: a) single phase; b) two phase

Applying the separated flow model [48],

$$\Delta P_{tp} = \Delta P_{tp,f} + \Delta P_{tp,a} \tag{41}$$

where $\Delta P_{tp,f}$ accounts for frictional effects, and $\Delta P_{tp,a}$ accounts for acceleration of flow.

The frictional pressure drop is

$$\Delta P_{tp,f} = \int -\left(\frac{dP}{dz}\right)_{tp,f} dz = \int -\left(\frac{dP}{dz}\right)_{l} \phi_l^2 dz \tag{42}$$

where ϕ_l^2 is two phase multiplier and defined as

$$\phi_l = \left[\frac{(dP/dz)_{tp,f}}{(dP/dz)_l}\right]^{1/2} \tag{43}$$

and l denotes the frictional pressure gradient that would result if the liquid flows alone at a mass flux of $G_{max}(1-x)$.

Thus the two phase frictional pressure drop is

$$\Delta P_{tp,f} = \sum_{i=N_{tr}}^{N_t} f_{sp,i} \frac{G_{max}^2 (1-x)^2}{2\rho_l} \phi_l^2 \tag{44}$$

The acceleration term is

$$-\left(\frac{dP}{dz}\right)_{tp,a} = G_{max}^2 \frac{d}{dz}\left[\frac{x^2}{\rho_v \alpha} - \frac{(1-x)^2}{\rho_l(1-\alpha)}\right] \tag{45}$$

where α is void fraction, and pressure drop due to vapor acceleration is

$$\Delta P_{tp,a} = G_{max}^2 \left[\frac{x^2}{\rho_v \alpha} - \frac{(1-x)^2}{\rho_l(1-\alpha)}\right]_{outlet} - G_{max}^2 \left[\frac{x^2}{\rho_v \alpha} - \frac{(1-x)^2}{\rho_l(1-\alpha)}\right]_{inlet} \tag{46}$$

Thus the pressure drop can be estimated from

$$\begin{aligned} \Delta P = & \sum_{i=1}^{N_{tr}} f_{sp,i} \frac{G_{max}^2}{2\rho_l} + \sum_{i=N_{tr}}^{N_t} f_{sp,i} \frac{G_{max}^2 (1-x)^2}{2\rho_l} \phi_l^2 \\ & + \left\{ G_{max}^2 \left[\frac{x^2}{\rho_v \alpha} - \frac{(1-x)^2}{\rho_l(1-\alpha)}\right]_{outlet} - G_{max}^2 \left[\frac{x^2}{\rho_v \alpha} - \frac{(1-x)^2}{\rho_l(1-\alpha)}\right]_{inlet} \right\} \end{aligned} \tag{47}$$

Chisholm and Laird formulated the two phase multiplier ϕ_l^2 using Martinelli parameter as [49]

$$\phi_l^2 = 1 + \frac{C}{X} + \frac{1}{X^2} \tag{48}$$

where *C* is empirically determined constant, and *X* is Martinelli parameter.

$$X = \left[\frac{(dP/dz)_l}{(dP/dz)_v}\right]^{1/2} \tag{49}$$

$(dP/dz)_l$ and $(dP/dz)_v$ are the frictional pressure gradients for the liquid and vapor phases flowing alone inside the microgap, respectively. These frictional gradients can be computed as

$$\left(\frac{dP}{dz}\right)_l = -\frac{2fG_{max}^2(1-x)^2}{\rho_l D} \tag{50}$$

$$\left(\frac{dP}{dz}\right)_v = -\frac{2fG_{max}^2 x^2}{\rho_v D} \tag{51}$$

and frictional factor is determined using Equation (40), and thus

$$X = \left(\frac{1-x}{x}\right)^{0.776}\left(\frac{\mu_l}{\mu_v}\right)^{0.225}\left(\frac{\rho_v}{\rho_l}\right)^{0.5} \tag{52}$$

Five previous correlations are compared, and equations for C and void fraction α are listed in Table 5. Most pressure drop correlations follow the pioneering Lockhart-Martinelli type of correlations [50, 51]. These correlations were developed for two phase flow in macroscale pipes. Qu and Mudawar correlation was developed for 21 parallel $231\ \mu m \times 713\ \mu m$ microchannels using water [52]. Krishnamurthy and Peles [53] correlation was developed for nitrogen-water two phase flow across a bank of circular micro pillars of a diameter of 100 μm and a pitch-to-diameter ratio 1.5. α_H is homogeneous flow void fraction.

$$\alpha_H = \frac{x/\rho_v}{(1-x)/\rho_l + x/\rho_v} \tag{53}$$

Reeser et al. developed pressure drop correlations for water and HFE-7200 in microcap with staggered and inline square pin fins [32], and their correlation does not have the vapor acceleration term.

The predicted pressure drop using these correlations for sparse and dense devices are compared in Figure 35 to Figure 39. For sparse device, the Lockhard and Martinelli viscous liquid and viscous vapor model and Reeser et al model can predict pressure drop in current study within $\pm 30\%$. None of these correlations are able to predict pressure drop within $\pm 30\%$ for dense device.

Based on current data, a new pressure drop correlation is proposed. The void fraction and C factor are

$$\alpha = 1 - \frac{1}{\sqrt{1 + \frac{20}{X} + \frac{1}{X^2}}} \tag{54}$$

For sparse device,

$$C = 50 Re_l^{-0.4} \tag{55}$$

For dense device,

$$C = 9.7 Re_l^{-0.4} \tag{56}$$

Or

$$C = 4.94 \left(\frac{S_T}{D}\right)^{1.18} \left(\frac{S_L}{D}\right)^{1.18} Re_l^{-0.4} \tag{57}$$

The predicted pressure drop using this new model are shown in Figure 40. The mean absolute error of the new pressure drop correlation for sparse device and dense device are 4.1% and 4.5%, respectively.

For other working fluid, vapor density is suggested to be included in the factor C in the following form

$$C = 4.94\left(\frac{S_T}{D}\right)^{1.18}\left(\frac{S_L}{D}\right)^{1.18} Re_l^{-0.4}\left(\rho_{fluid,v}/\rho_{water,v}\right)^{0.27} \quad (58)$$

where $\rho_{fluid,v}$ and $\rho_{water,v}$ are vapor phase densitis of working fluid and water, respectively. This will be tested and discussed in Chapter 5 with dielectric liquid HFE-7200.

Table 5 Comparison of pressure drop correlations

Reference	C	α	MAE (sparse)	MAE (dense)
Lockhart and Martinelli (viscous liquid, viscous vapor) [50, 51]	5	$1-\frac{1}{\sqrt{1+\frac{20}{X}+\frac{1}{X^2}}}$	10.9%	55.7%
Lockhart and Martinelli (viscous liquid, turbulent vapor) [50, 51]	12	$1-\frac{1}{\sqrt{1+\frac{20}{X}+\frac{1}{X^2}}}$	30.5%	171.9%
Qu and Mudawar [52]	$21[1-\exp(-319d_{hch})](0.00418G_{max}+0.0613)$	$\frac{1}{1+\left(\frac{1-x}{x}\right)\left(\frac{\rho_v}{\rho_{fl}}\right)^{2/3}}$	163.3%	874.4%
Krishnamurthy and Peles [53]	$0.0358Re_{D,sp,l}$	$(1+0.04503f^{0.34}\ln(x))\alpha_H$	23.5%	158.7%
Reeser et al.[32]	8	-	12.8%	85.6%

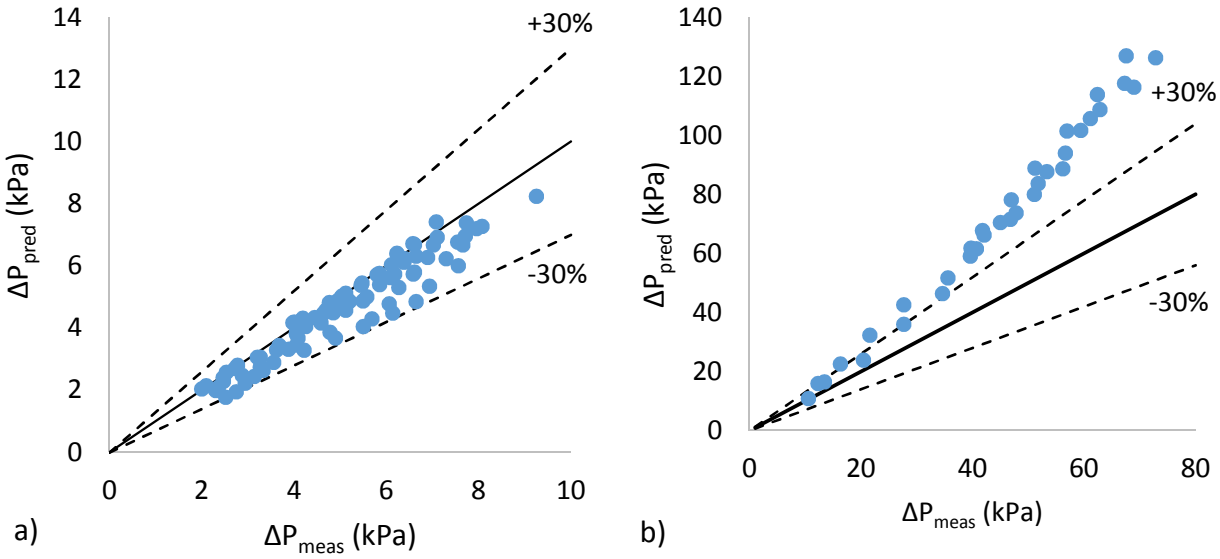

Figure 35 Pressure prediction using Lockhart and Martinelli (viscous liquid-viscous vapor) correlation: a) sparse device; b) dense device

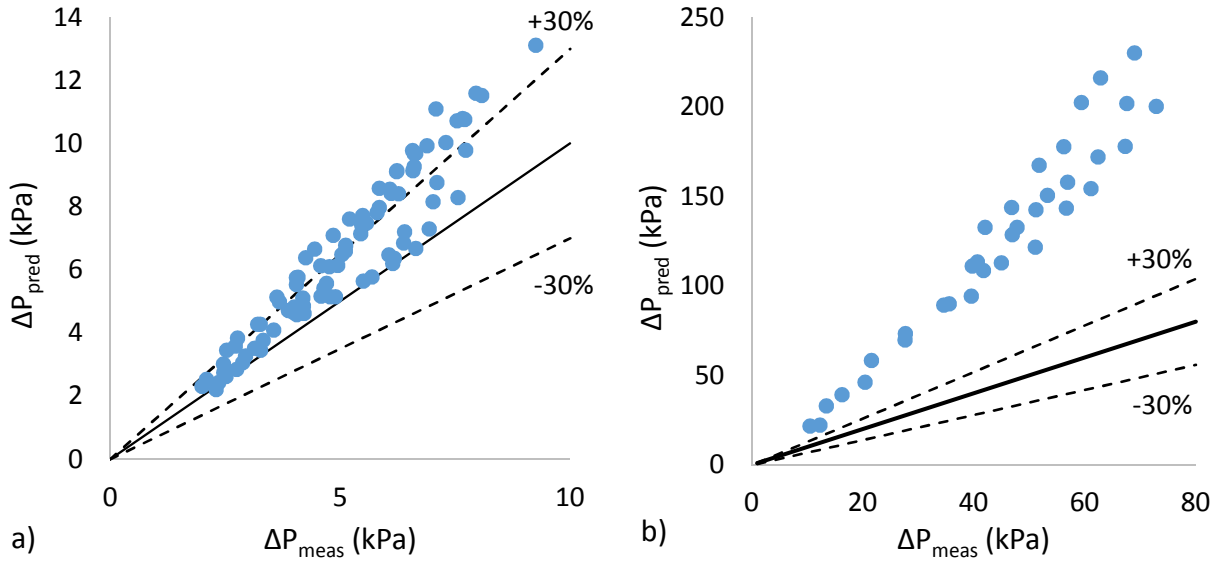

Figure 36 Pressure prediction using Lockhart and Martinelli (viscous liquid-turbulent vapor) correlation: a) sparse device; b) dense device

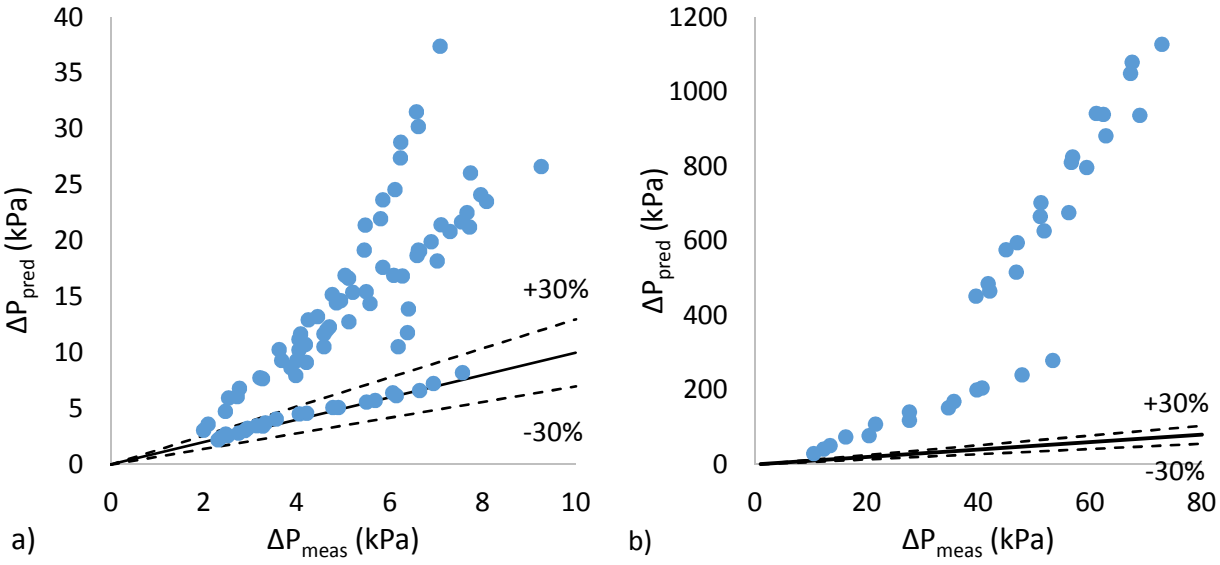

Figure 37 Pressure prediction using Qu and Mudawar correlation: a) sparse device; b) dense device

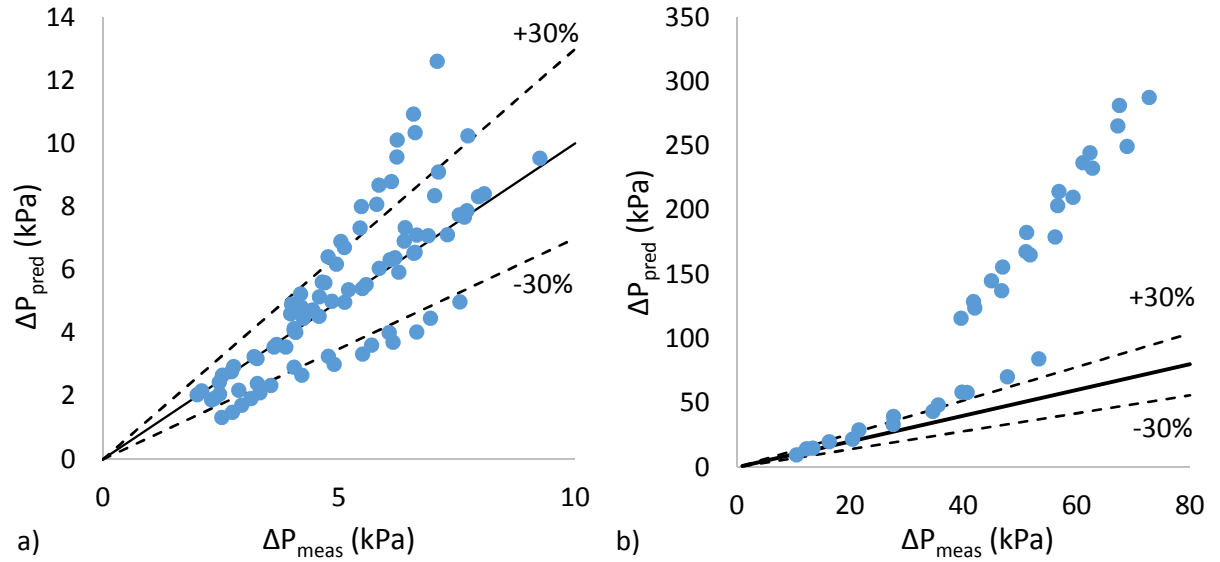

Figure 38 Pressure prediction using Krishnamurthy and Peles correlation: a) sparse device; b) dense device

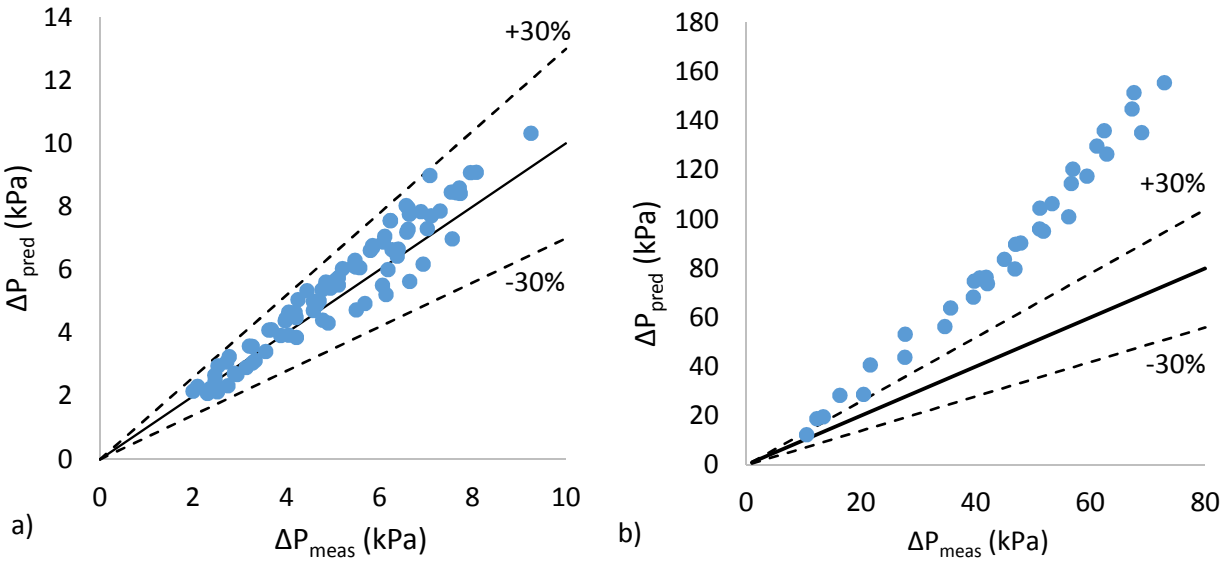

Figure 39 Pressure prediction using Reeser et al. correlation: a) sparse device; b) dense device

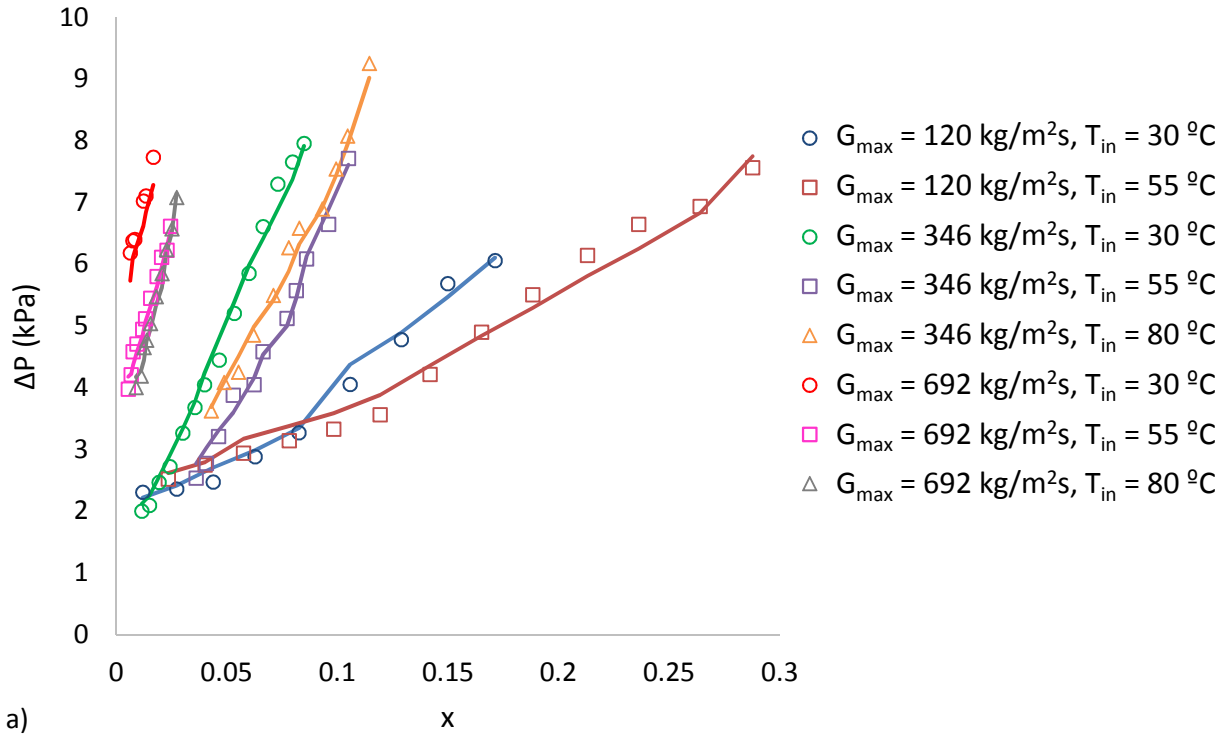

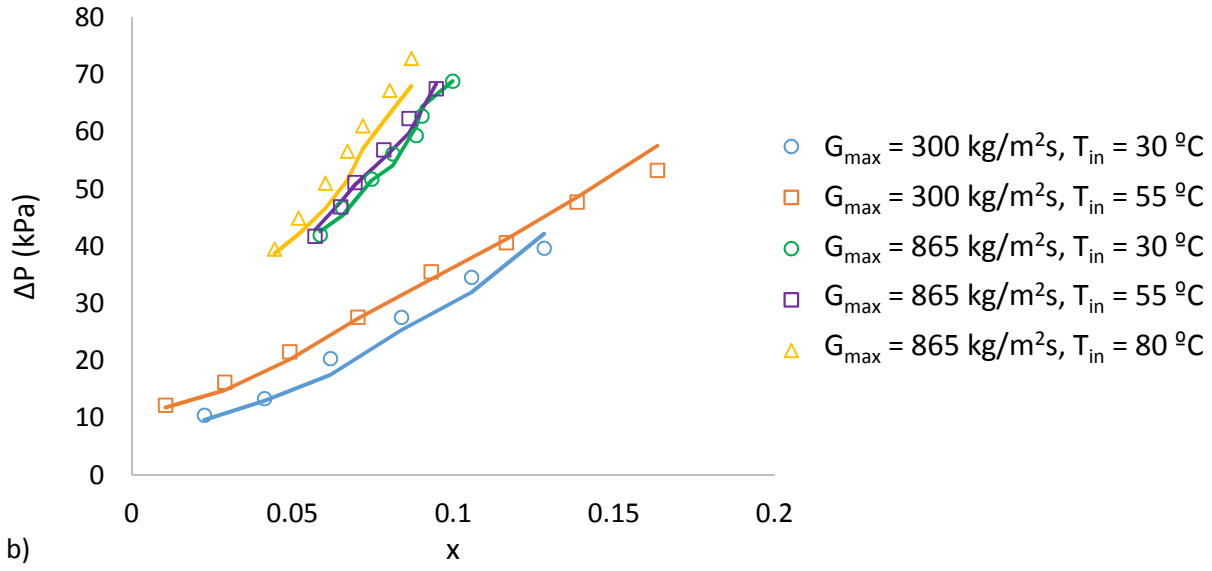

Figure 40 Pressure prediction using new correlation: a) sparse device; b) dense device

3.2.6 Ledinegg Instability

Two phase flow instability is a complex topic because many parameters can affect it simultaneously. The study of two phase flow instability started in 1930s after Ledinegg introduced the concept [54]. Two phase flow instability was first reviewed by Boure et al, and was classified into two types: static instabilities and dynamic instabilities. Tadrist reviewed two phase flow instabilities in narrow spaces such as micro channels [55], and recently Ruspini et al also present a review on this topic [56]. Ledinegg instability is one type of static instability. A two phase flow is subject to static instability when a small change from its original steady state flow condition, a new steady condition is not possible in vicinity of its original steady state.

Ledinegg instability, also known as flow excursion, involves a sudden change of flow rate. The criteria for Ledinegg instability is

$$\left(\frac{\partial \Delta P}{\partial G}\right)_{\text{int}} \leq \left(\frac{\partial \Delta P}{\partial G}\right)_{\text{ext}} \tag{59}$$

where $\left(\frac{\partial \Delta P}{\partial G}\right)_{\text{int}}$ and $\left(\frac{\partial \Delta P}{\partial G}\right)_{\text{ext}}$ are slopes of pressure drop versus flow rate curve of internal and external system, respectively. The internal system refers to flow section involving two phase, and the external system refers flow section that provides external pressure drop such as a pump. At a fixed heat flux, the representative pressure drop versus flow rate curve of two phase flow is an N shape curve, as shown in Figure 41. When the pump curve crosses the pressure drop versus flow rate curve at point A, and the slope $\left(\frac{\partial \Delta P}{\partial G}\right)_{\text{ext}}$ of pump curve is smaller than the slope $\left(\frac{\partial \Delta P}{\partial G}\right)_{\text{int}}$ of internal system as in Case 1, the two phase flow is stable. After a small disturbance of flow rate to the left of point A, the pump is able to provide larger pressure drop than the internal system required, resulting in increase in flow rate. Thus two phase flow can return to its original state, point A. If the slope $\left(\frac{\partial \Delta P}{\partial G}\right)_{\text{ext}}$ of pump curve is larger than the slope $\left(\frac{\partial \Delta P}{\partial G}\right)_{\text{int}}$ of internal system as in Case 2, after a small disturbance in flow rate to the left of point A, the pump is incapable of providing pressure drop required by internal system, resulting in even smaller flow rate. In this case, the two phase flow is unstable, and will shift to a stable condition (point B or point C) [57]. Many parameters can have effects on this type of two phase flow instability, such as system pressure, heat flux, flow rate, inlet fluid temperature, system geometry and fluid properties.

Ledinegg instability is known to be an issue in low pressure system [55, 57, 58]. Increasing system pressure reduces the negative slope of pressure drop versus flow rate curve due to reduction of liquid to vapor density ratio ρ_l/ρ_v, causing instability to diminish [58]. Since this section studied flow boiling of water in a vacuumed system, Ledinegg instability has been observed for

many heat flux, mass flux and inlet temperature conditions. The oscillations of pressure drop, flow rate, and temperature lead to either single phase liquid flow, or two phase flow alternatively present in the channel, or periodically change of boiling area in the channel. The slope of pump curve is -5 from the manufacture's specification sheet, and the slope $\left(\frac{\partial \Delta P}{\partial G}\right)_{\text{int}}$ of internal system when pressure and flow rate oscillation occurs ranges from -8 kpa/(mL/min) to -15 kpa/(mL/min) after examination of collected data.

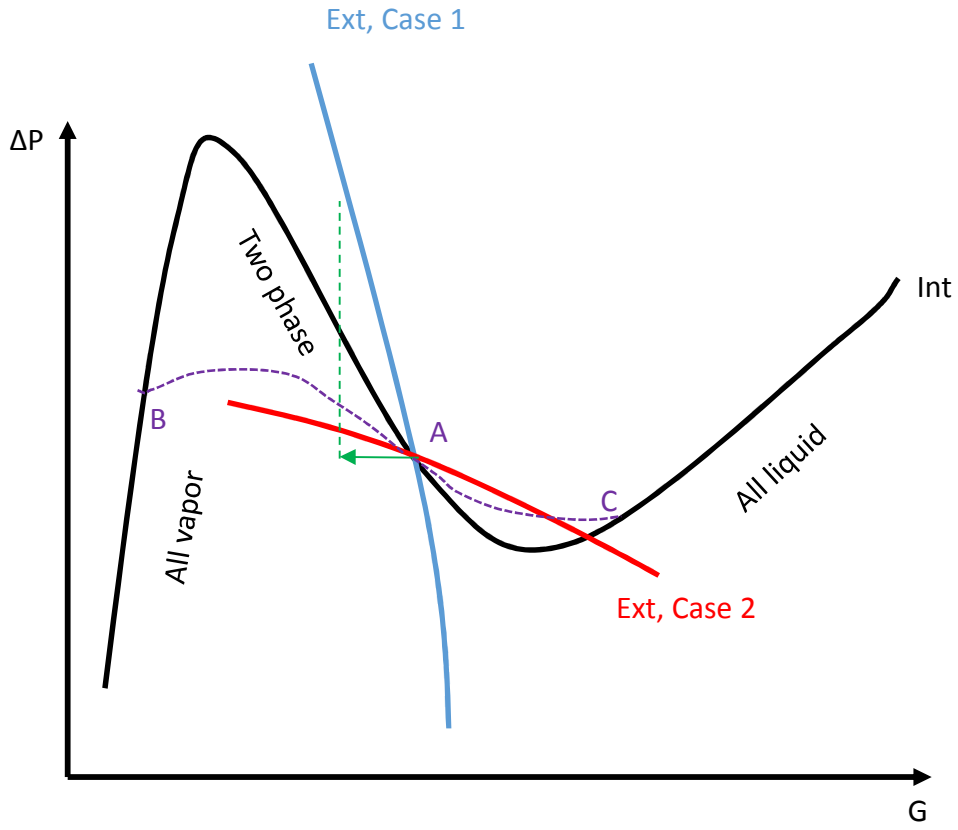

Figure 41 Characteristic of pressure drop vs flow tate at fixed heat flux

For sparse device at G_{max} = 346 kg/m^{2}s, T_{in} = 55 ºC and q_{eff}" = 67 W/cm^2, the fluctuation of pressure drop and volume flow rate (VFR) is shown in Figure 42. The flow pattern is single phase

liquid and two phase flow alternatively appear in pin fin array. The pressure drop accounts for the pressure from inlet of device to condenser, which is the flow section involving two phase flow. Two phase flow is associated with higher pressure drop and lower flow rate, and single phase liquid flow is associated with lower pressure drop and higher flow rate, as indicates in the figure. A small disturbance in two phase flow condition results in the flow to shift to a point C in Figure 41.

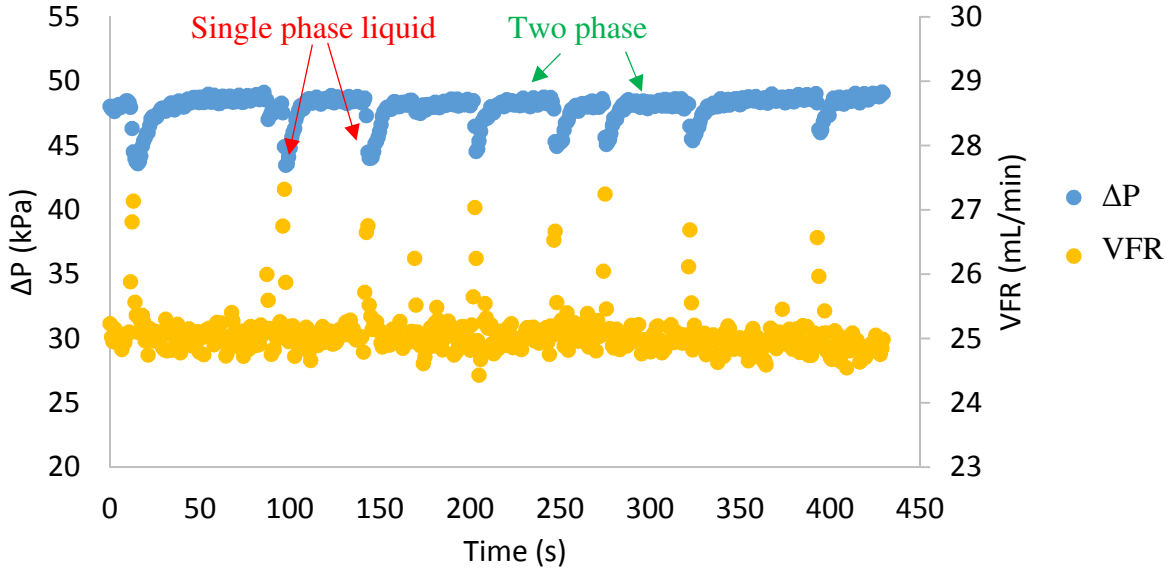

Figure 42 Sparse device, G_{max} = 346 kg/m^{2}s, T_{in} = 55 ºC, q_{eff}" = 67 W/cm^2

The instabilities are also observed for dense device. At G_{max} = 865 kg/m^{2}s, T_{in} = 30 ºC, and oscillations of pressure drop and flow rate at three different heat fluxes q_{eff}" = 88, 128 and 147 W/cm^2 are shown in Figure 43, Figure 44 and Figure 45. Heat fluxes beyond 147 W/cm^2 results in stable two phase flow. As heat flux increases, the device pressure increases, and two phase flow becomes stable. The single phase period is shortened and eventually eliminated as heat flux increases. Flow visualization at G_{max} = 865 kg/m^{2}s, T_{in} = 30 ºC, and q_{eff}" = 147 W/cm^2 showing single phase liquid flow and two phase flow at different time instances are presented in Figure 46.

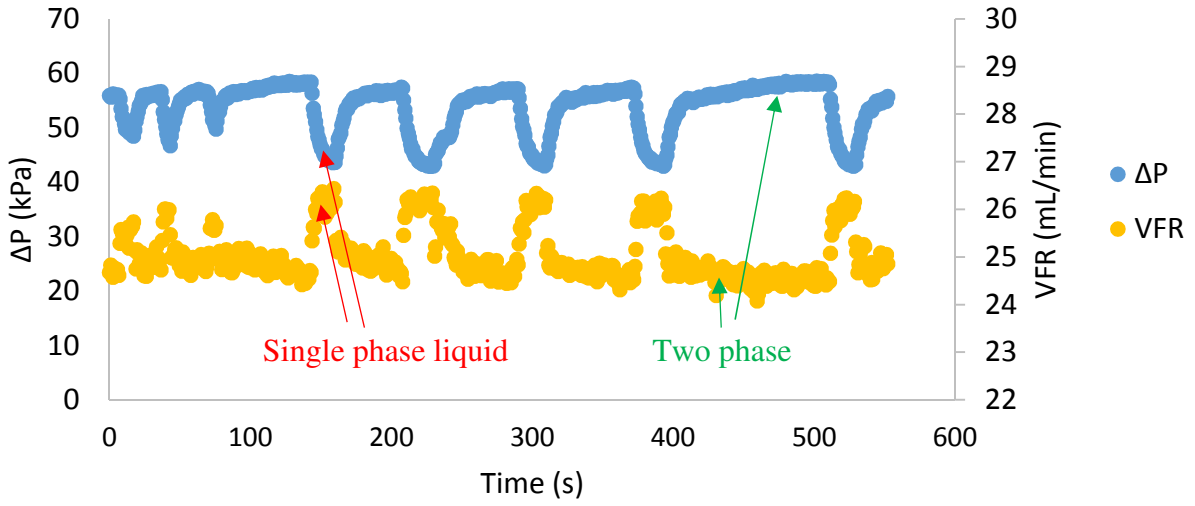

Figure 43 Dense device, G_{max} = 865 kg/m^{2}s, T_{in} = 30 ºC, q_{eff}" = 88 W/cm^2

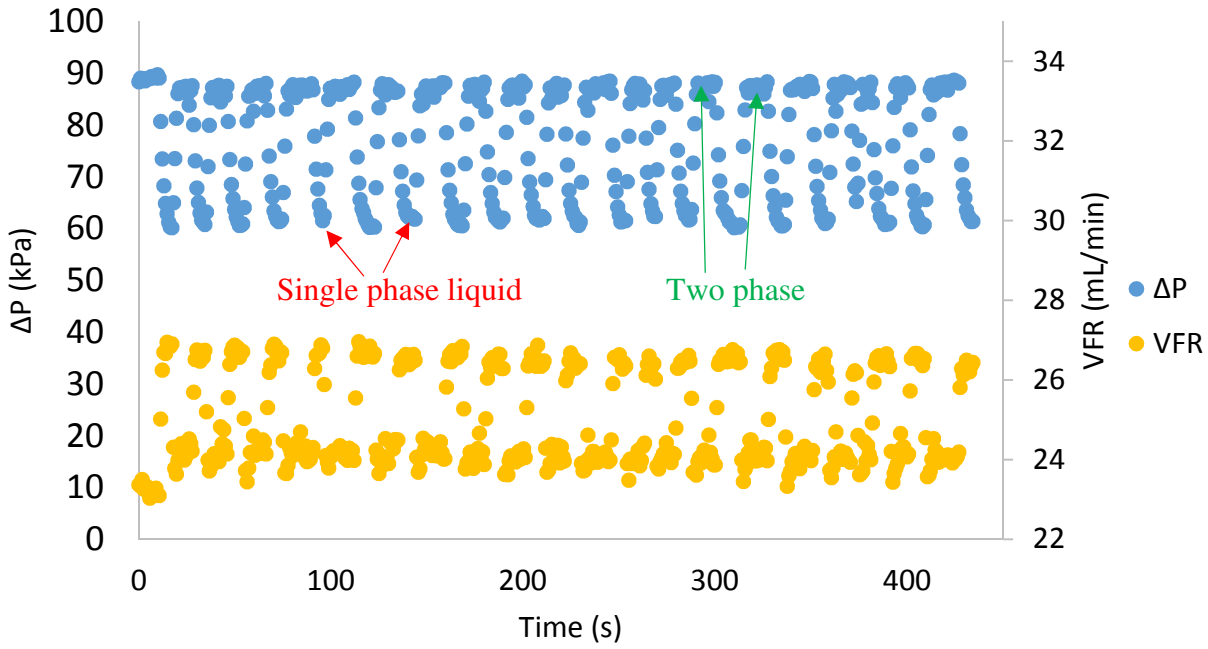

Figure 44 Dense device, G_{max} = 865 kg/m^{2}s, T_{in} = 30 ºC, q_{eff}" = 128 W/cm^2

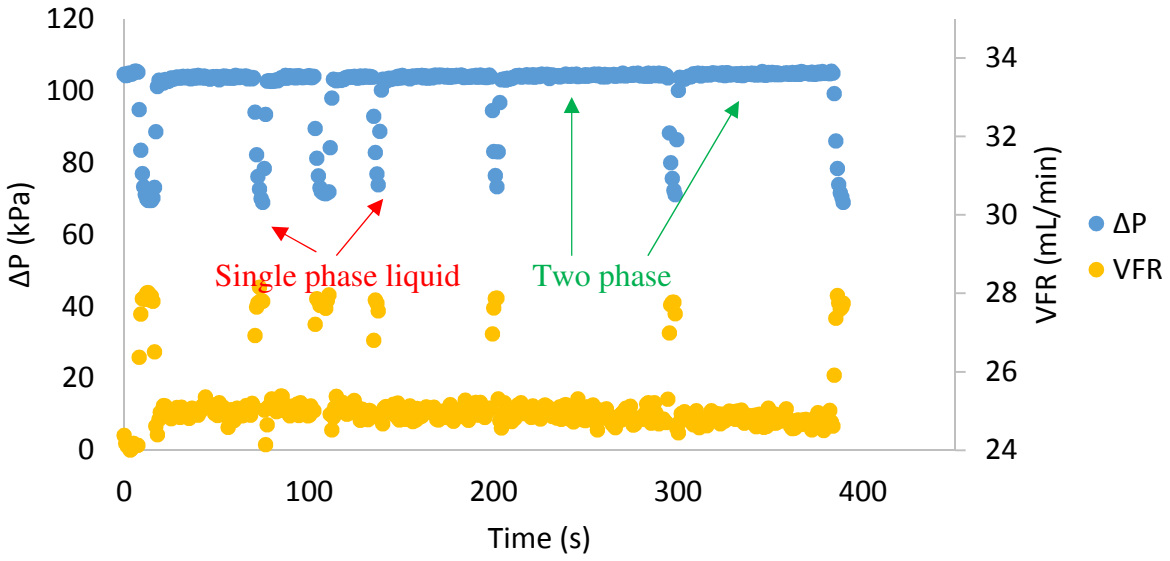

Figure 45 Dense device, G_{max} = 865 kg/m^{2}s, T_{in} = 30 ºC, q_{eff}" = 147 W/cm^2

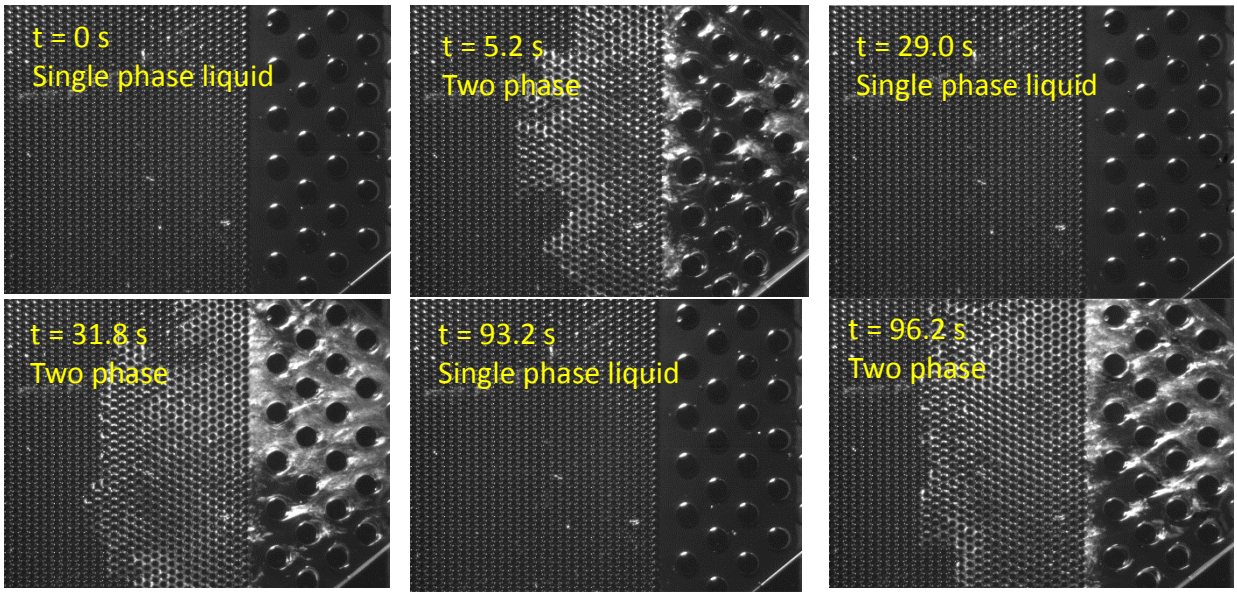

Figure 46 Flow visualization: dense device, G_{max} = 865 kg/m^{2}s, T_{in} = 30 ºC, q_{eff}" = 147 W/cm^2

3.3 Conclusions

This chapter studies flow boiling of water in pin fin enhanced microgap at reduced pressure in a closed flow system with two pin fin configurations. Large ranges of mass fluxes, heat fluxes, and inlet fluid temperatures were tested. The conclusions are as follows:

1. Two phase heat transfer coefficient behavior strongly depends on flow patterns. Dryout significantly degrades two phase heat transfer coefficient, which is not desired.
2. A new two phase heat transfer coefficient correlation is developed, which can predict current results with a MAE of 6.2%.
3. A new pressure drop correlation is developed based on separated flow model, which can predict current results with a MAE of 4.1% and 4.5% for sparse and dense devices, respectively.
4. Unlike traditional two phase flow regimes in macro scale channels or in microchannels, no bubbly flow, slug flow or annular flow is seen in pin fin enhanced microgaps. Boiling occurs in an area close to microgap outlet at low heat flux, and moves towards microgap inlet, as heat flux increases. Liquid films are observed to surround pin fins inside the boiling area.
5. In sparse device at low heat flux, liquid film is uniformly attached to pin fins, and liquid films of adjacent pin fins are connected at certain locations. At high heat flux, liquid film is stretched to sharp-tail liquid wake. Bubble nucleates at rear side of pin fin inside liquid film/wake.
6. In dense device, no sharp-tail liquid wake or bubble nucleation inside liquid wake is seen due to limited space between pin fins. At low heat flux, nucleated bubbles travel

in transverse direction instead of moving downstream also due to limited space between pin fins. Similarly as in sparse device, liquid film is uniformly attached to pin fins, and liquid films of adjacent pin fins are connected at certain locations. At increased heat flux, liquid films are offset to downstream.

CHAPTER 4. FLOW BOILING OF WATER IN PIN FIN ENHANCED MICROGAP FOR DIFFERENT HEAT SOURCE LOCATIONS

This chapter studies the effects of heat source locations on flow boiling of water in pin fin enhanced microgap at reduced pressure. The change of heating location varies boiling area and pressure distribution inside microgap, resulting in change of two phase flow stability, heat transfer characteristics and two phase flow regime. To the best of the author's knowledge, no relevant work is available after reviewing literature.

4.1 Experiment procedure

There are totally four separate heaters on each device covering an area of 1 cm^2, and numbered from 1 to 4 along flow direction as shown in Figure 47. Three heating patterns are studied: only heater No.1 and No. 2 powered, only heater No. 2 and No. 3 powered, and only heater No. 3 and No. 4 powered. The two working heaters are powered equally. The two unpowered heaters are used as RTD for temperature measurements. The experiment setup is the same as in Chapter 2, and the device tested is the microgap with dense pin fins. Two mass fluxes and two inlet fluid temperatures are tested: G_{max} = 300 kg/m^2s and G_{max} = 865 kg/m^2s, T_{in} = 30 ºC and T_{in} = 55 ºC.

For each mass flux and inlet fluid temperature condition, heat flux was increased from 10 W/cm^2 by an increment of 10 W/cm^2 for each experiment, until either critical heat flux condition was reached, or heater temperatures reached safety limit of 130 ºC. The experiment procedure is the same as in Chapter 2.

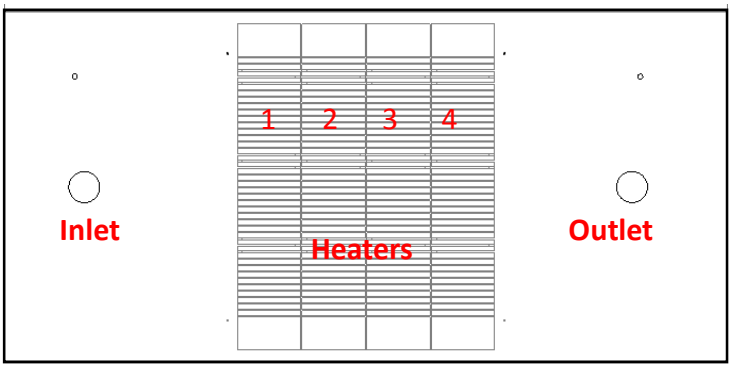

Figure 47 Heater locations

4.2 Results and Discussion

For each set of tests, results at the same mass flux and inlet fluid temperature with all four heaters powered are compared as a baseline case. The heaters are noted as H1, H2, H3 and H4 in the legends of figures. Two phase flow is more stable when heating locations move towards microgap outlet, and at higher inlet fluid temperature.

4.2.1 G_{max} = 300 kg/m^{2}s

Pressure drop is presented in Figure 48 for T_{in} = 30 ºC, and in Figure 49 for T_{in} = 55 ºC. More stable data points were collected as heating location moves from H1 and H2 to H3 and H4, and as inlet fluid temperature increases from 30 ºC to 55 ºC. At the same quality, pressure drop decreases, as the two powered heaters move from inlet to outlet. Boiling area is close to microgap inlet when heater No.1 and 2 are powered, and vapor needs to travel through more rows of pin fins than the case when boiling area is close to microgap outlet when heater No. 3 and 4 are powered, resulting in higher pressure drop. Pressure drop, when all four heaters are powered, falls between only H2 and H3 on and only H3 and H4 on cases.

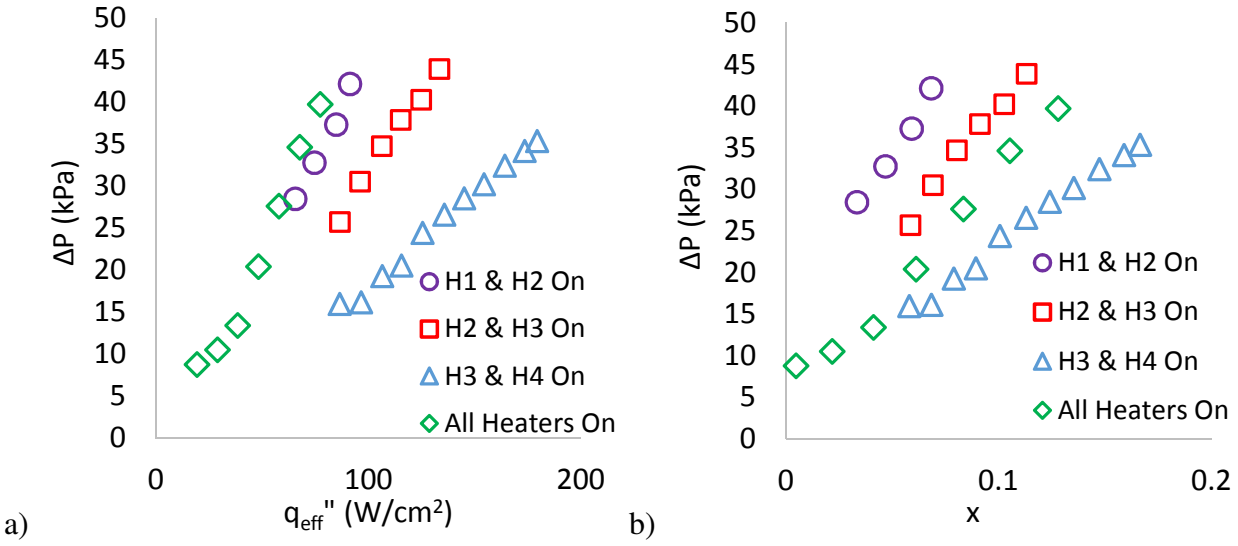

Figure 48 Pressure drop at G_{max} = 300 kg/m²s, T_{in} = 30 ºC: a) ΔP vs. q_{eff}"; b) ΔP vs. x

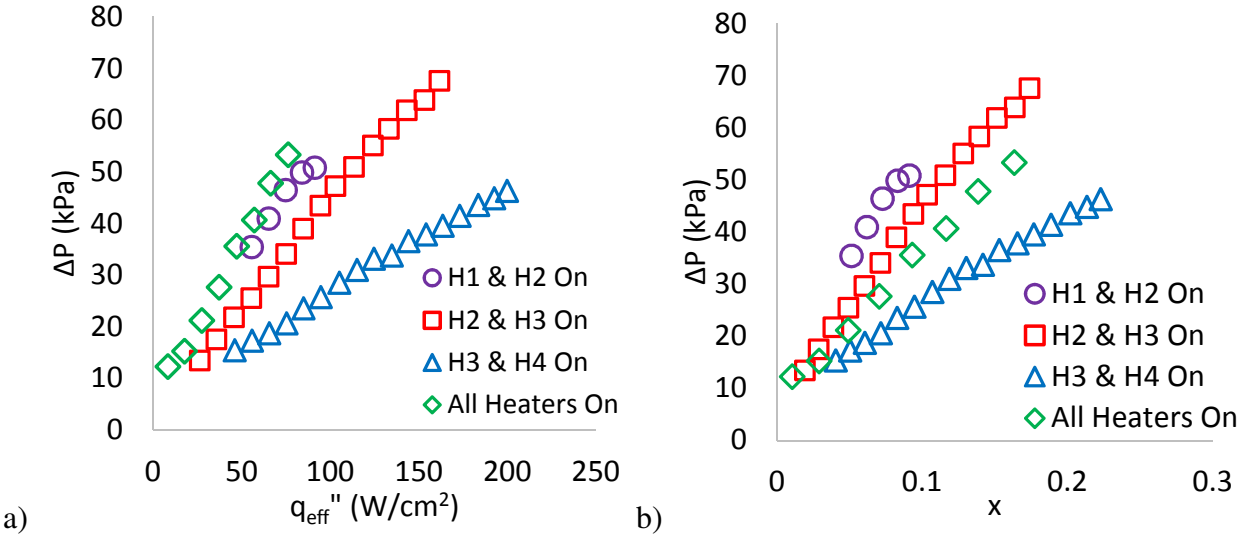

Figure 49 Pressure drop at G_{max} = 300 kg/m²s, T_{in} = 55 ºC: a) ΔP vs. q_{eff}"; b) ΔP vs. x

Figure 50 and Figure 51 show exit vapor quality for all heating locations when T_{in} = 30 ºC and T_{in} = 55 ºC, respectively. Vapor quality for all the three heating locations are in line with the case when all heaters are on by considering the fact that the total supplied power of the three

different heating location cases is half of the total power when all four heaters are on at the same heat flux.

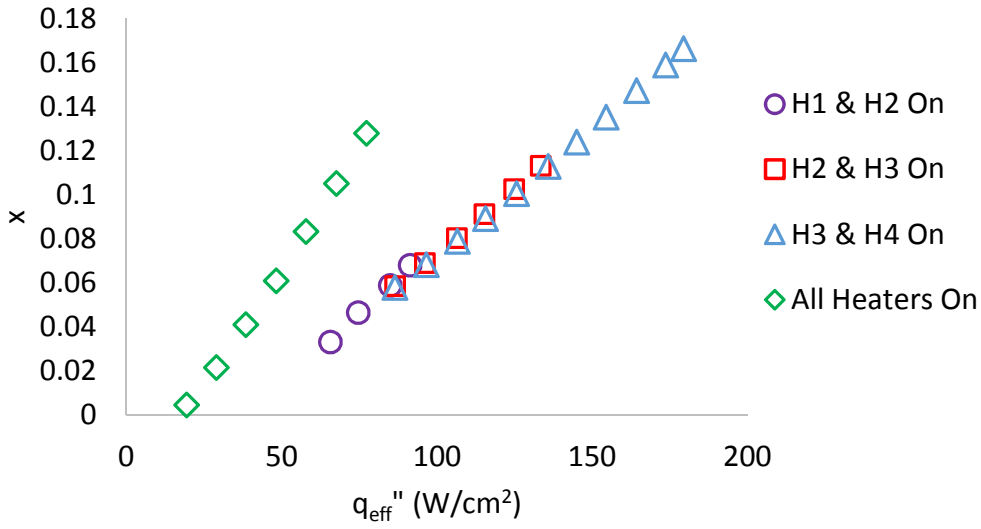

Figure 50 Exit vapor quality at G_{max} = 300 kg/m²s, T_{in} = 30 ºC

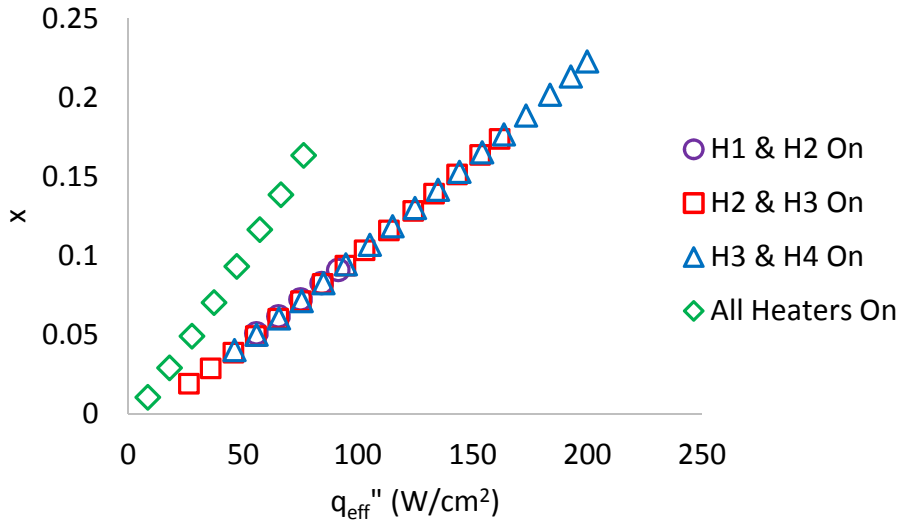

Figure 51 Exit vapor quality at G_{max} = 300 kg/m²s, T_{in} = 55 ºC

Figure 52 and Figure 53 compare two phase heat transfer coefficients for all heating conditions. Two phase heat transfer coefficients are calculated at the second working heater from microgap inlet. Two phase heat transfer coefficient improves, as heating location changes from close to inlet of microgap to outlet of microgap, and they are in the same range as when all four heaters are on. In Figure 52, the sudden drop in two phase heat transfer coefficient for the case when only heater No. 1 and No. 2 are on is caused by dryout, and this will be discussed in the context of flow visualization in next section. Heating locations at H1 and H2 are most unstable among all test cases. Two phase heat transfer coefficient first increases and then decreases when H2 and H3 on, and when H3 and H4 on. This is caused by change of two phase flow patterns and will be discussed in next section.

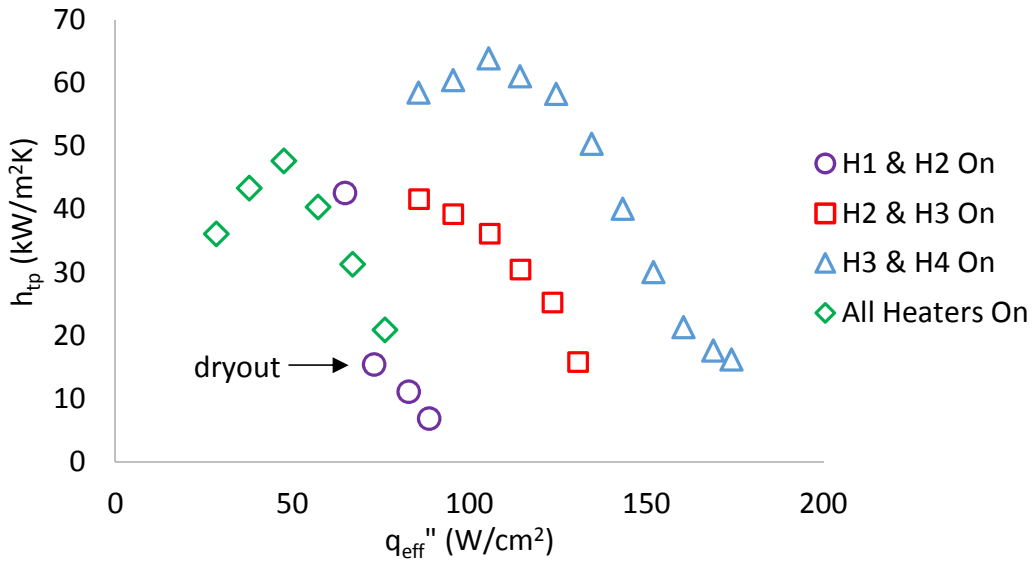

a)

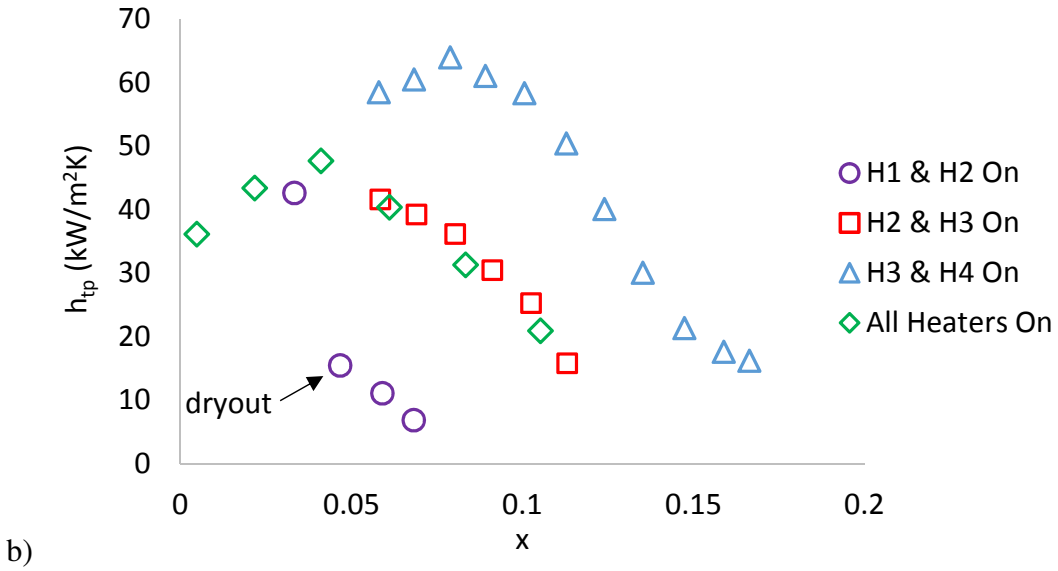

b)

Figure 52 Two phase heat transfer coefficient at G_{max} = 300 kg/m²s, T_{in} = 30 ºC: a) h_{tp} vs q_{eff}"; b) h_{tp} vs x

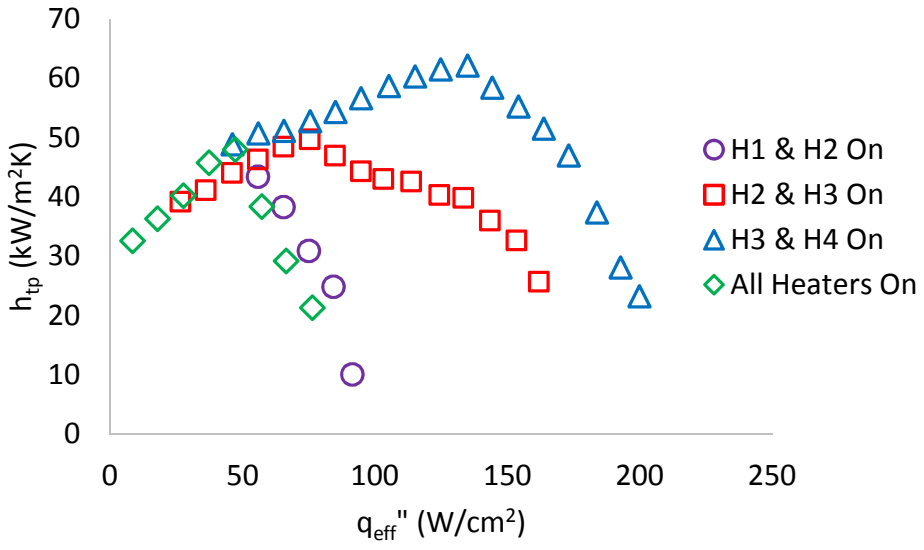

a)

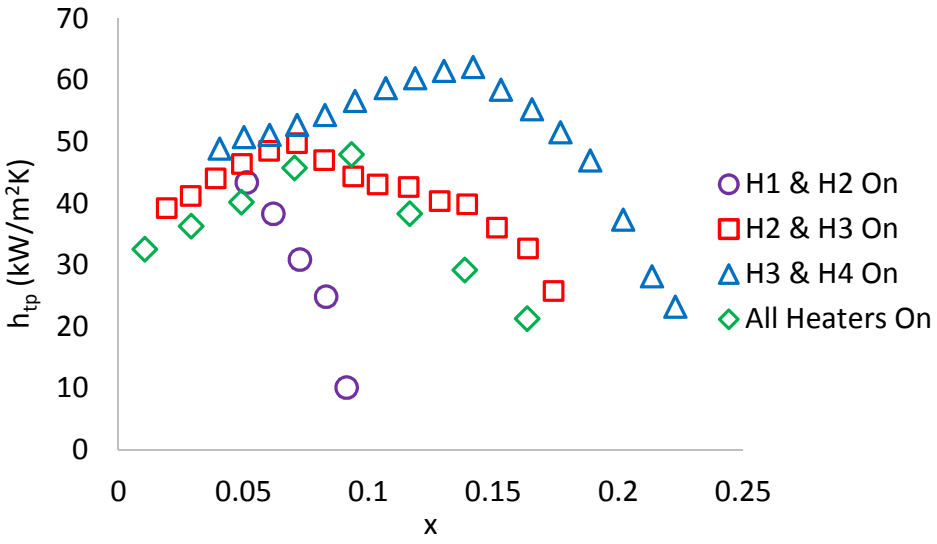

b)

Figure 53 Two phase heat transfer coefficient at G_{max} = 300 kg/m²s, T_{in} = 55 ºC: a) h_{tp} vs q_{eff}"; b) h_{tp} vs x

The saturation pressure is evaluated at the second of the two active heaters from microgap inlet. For the case with all four heaters on, saturation pressure is evaluated at the fourth heater from microgap inlet. Saturation pressures are below atmospheric pressure for the three heating locations as shown in Figure 54. At the same heat flux, saturation pressure decreases when heating location changes from close to microgap inlet to outlet. This agrees with the pressure drop trend. Figure 55 and Figure 56 present wall temperatures and boiling curve. A severe dryout condition causes the rapid increase in wall temperature and wall superheat when only heater No. 1 and No. 2 are powered. The changes of slope in wall temperature and boiling curve indicate dryout condition.

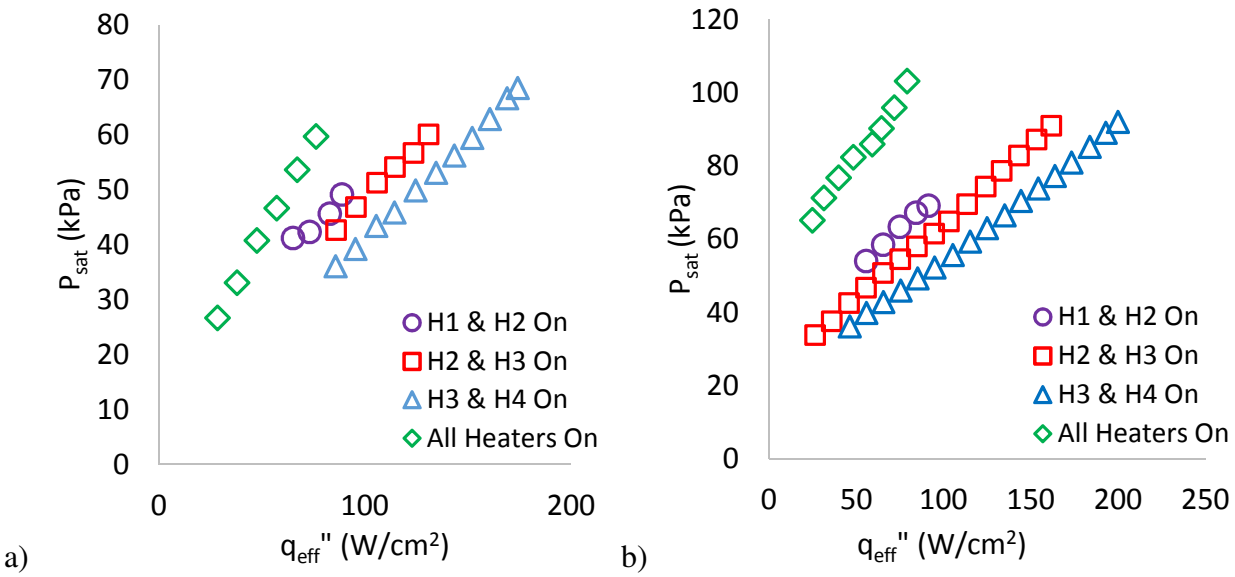

Figure 54 Saturation pressure at G_{max} = 300 kg/m²s: a) T_{in} = 30 ºC; b) T_{in} = 55 ºC

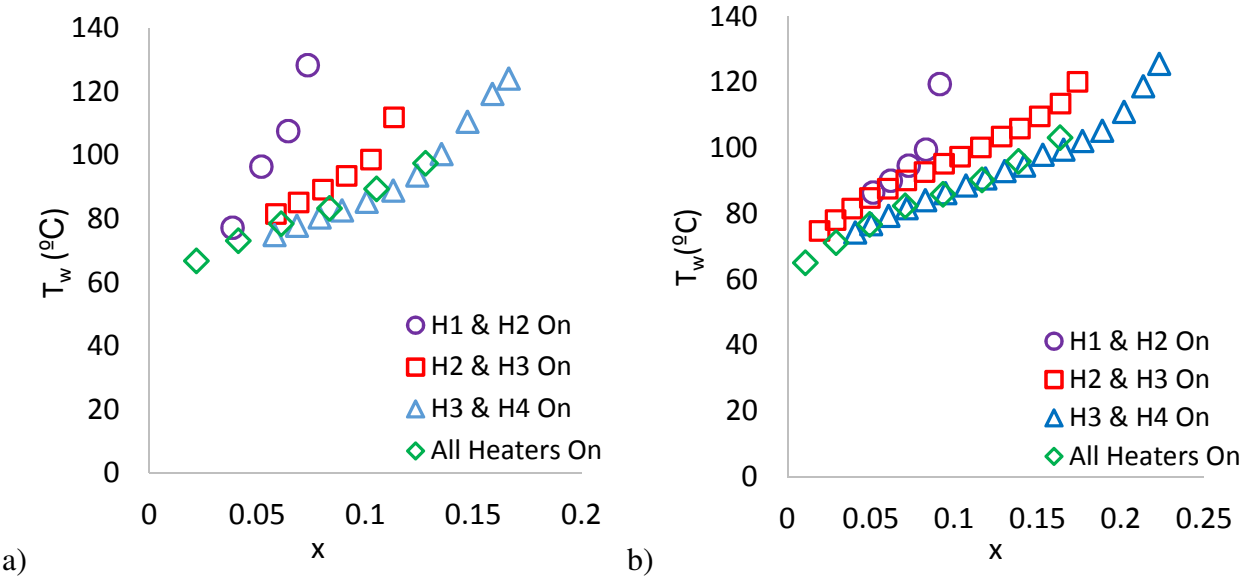

Figure 55 Wall temperature at G_{max} = 300 kg/m²s: a) T_{in} = 30 ºC; b) T_{in} = 55 ºC

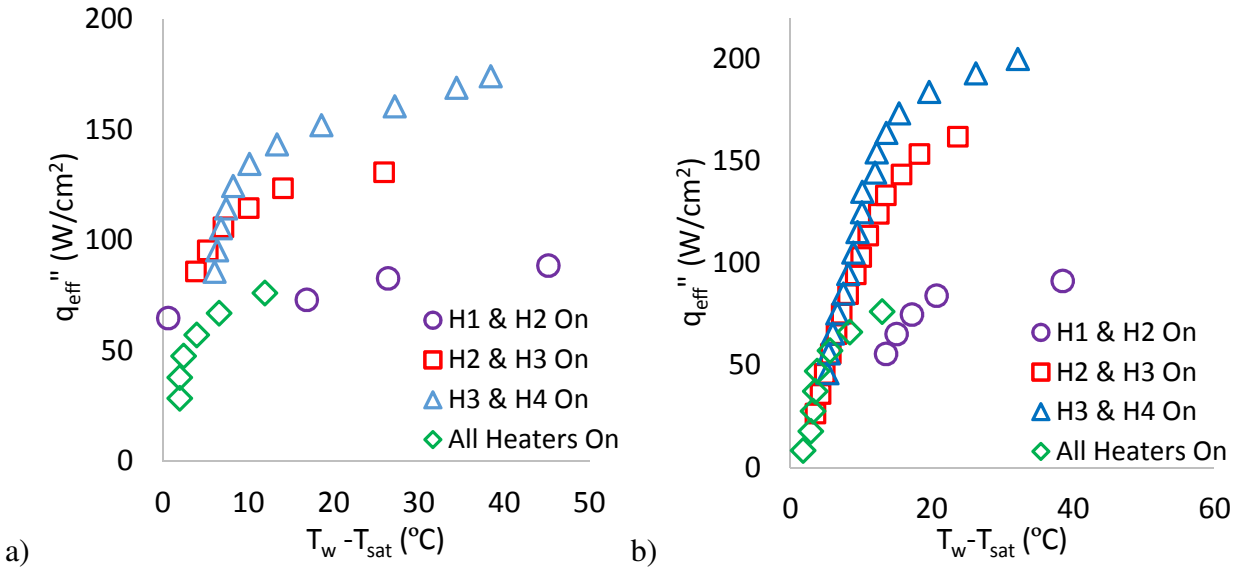

Figure 56 Boiling curve at G_{max} = 300 kg/m^{2}s: a) T_{in} = 30 ºC; b) T_{in} = 55 ºC

4.2.2 G_{max} = 865 kg/m^{2}s

At mass flux of G_{max} = 865 kg/m^{2}s and T_{in} = 30 ºC, no steady boiling condition could be achieved before heater temperatures reached the safe limit of 130 ºC. For T_{in} = 55 ºC, only the heating location at heater No. 3 and No. 4 has steady boiling.

Figure 57 compares pressure drop for the cases when only heater No. 3 and No. 4 are on, and when all heaters are on. Pressure drop for the latter case is slightly higher than the former case at the same exit vapor quality. Two phase heat transfer coefficient, when only heater No. 3 and No. 4 are powered, is higher than two phase heat transfer coefficient when all four heaters are on, as shown in Figure 58. This agrees with results of G_{max} = 300 kg/m^{2}s. Exit vapor quality and boiling curve are presented in Figure 59 a) and b), respectively. Exit vapor quality also agrees with each other for both heating conditions, as in the cases when G_{max} = 300 kg/m^{2}s. Wall superheat increases linearly with heat fluxes, as seen in Figure 59 b) because no dryout condition is observed.

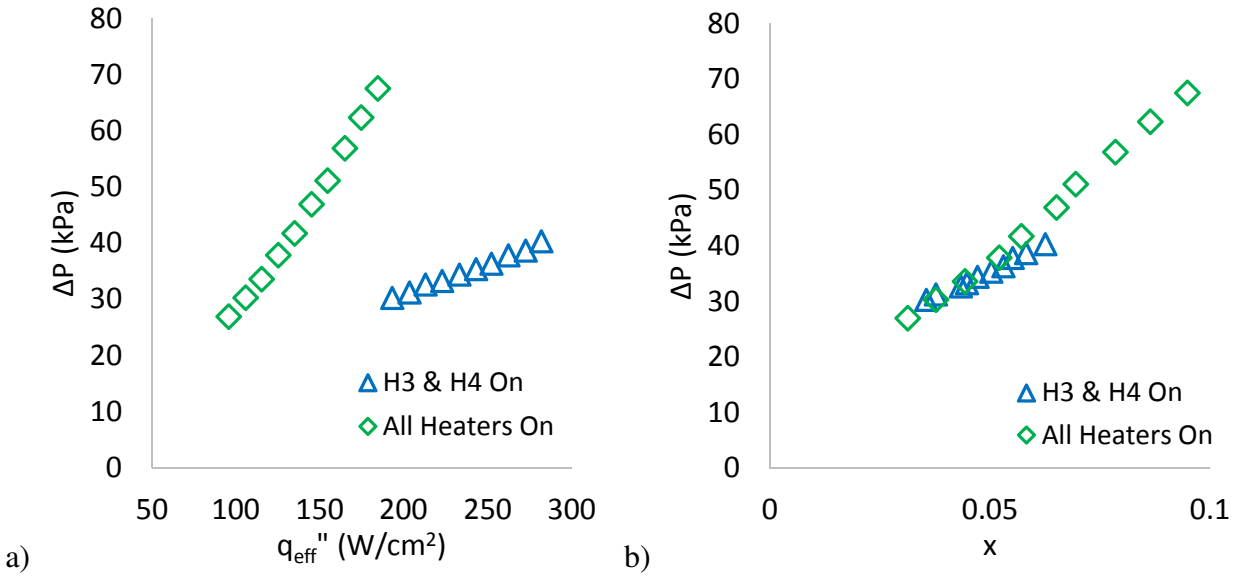

Figure 57 Pressure drop at G_{max} = 865 kg/m²s, T_{in} = 55 ºC: a) ΔP vs. q_{eff}"; b) ΔP vs. x

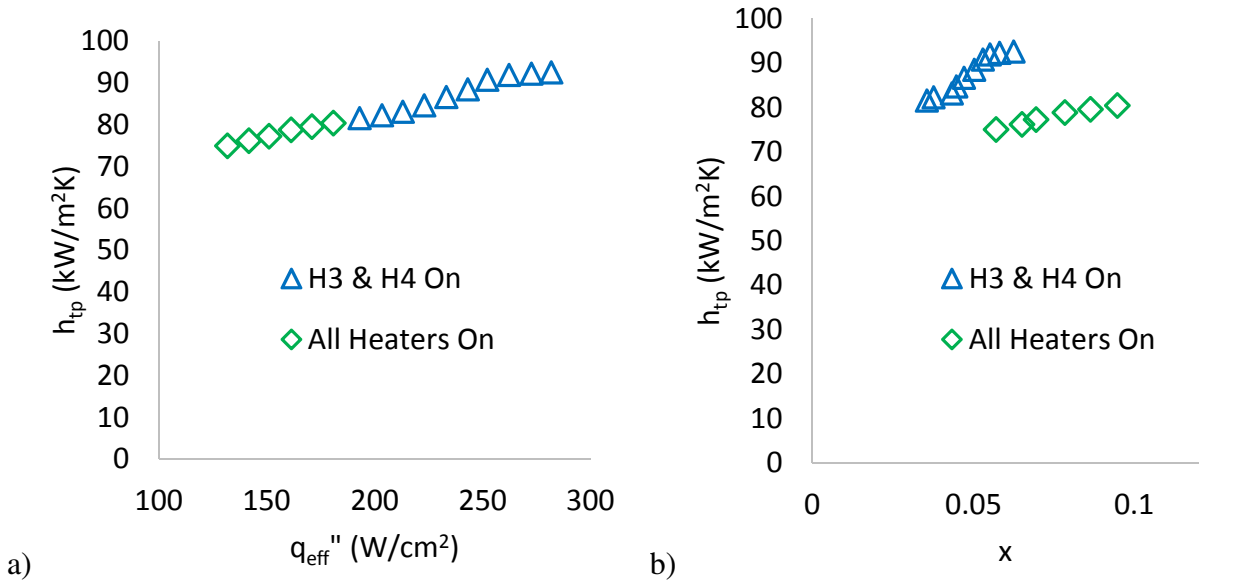

Figure 58 Two phase heat transfer coefficient at G_{max} = 865 kg/m²s, T_{in} = 55 ºC: a) h_{tp} vs. q_{eff}"; b) h_{tp} vs. x

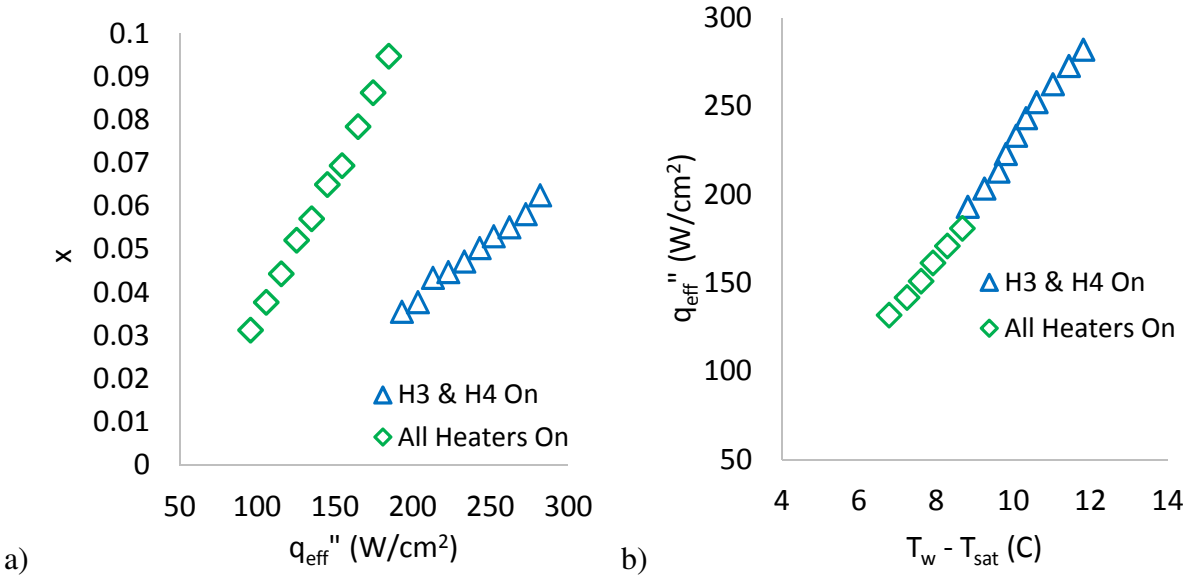

Figure 59 G_{max} = 865 kg/m²s, T_{in} = 55 ºC: a) exit vapor quality; b) boiling curve

Similar to Chapter 3, Ledinegg instability is also observed. The pressure and flow rate oscillations for G_{max} = 865 kg/m²s, T_{in} = 55 ºC, q_{eff}" = 76.1W/cm² are shown in Figure 60. The flow pattern is single phase liquid and two phase flow alternatively occupying microgap.

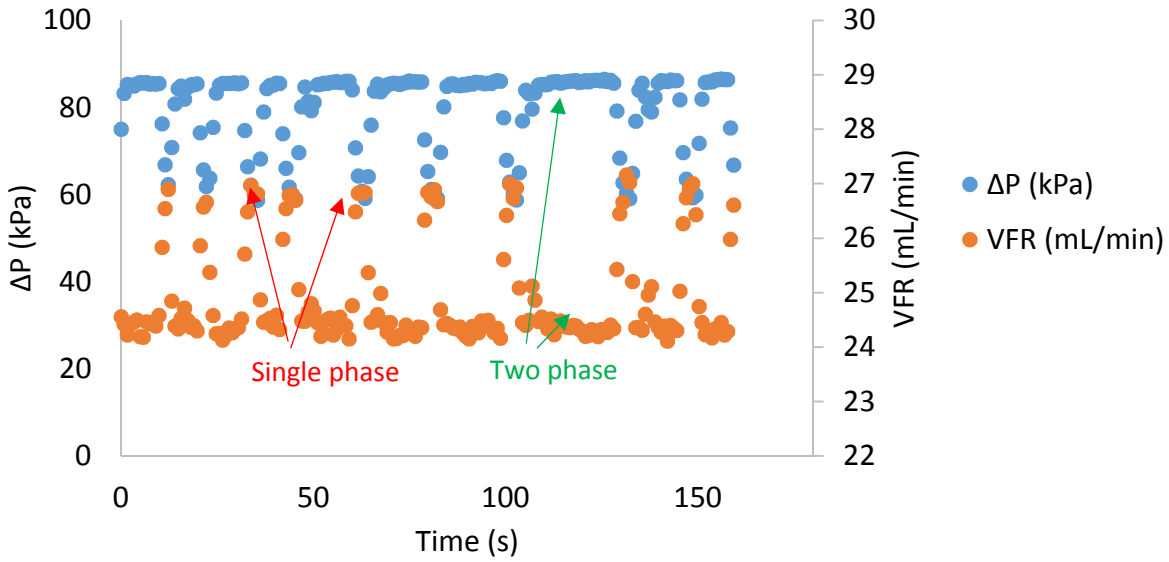

Figure 60 Instability at G_{max} = 865 kg/m²s, T_{in} = 55 ºC, q_{eff}" = 76.1 W/cm²

4.2.3 Two Phase Heat Transfer Coefficient and Pressure Drop Correlations

The two phase heat transfer coefficient correlation developed in Chapter 3 can predict two phase heat transfer coefficients within ±20% when no dryout occurs, as shown in Figure 61. The mean absolute error is 9.8%.

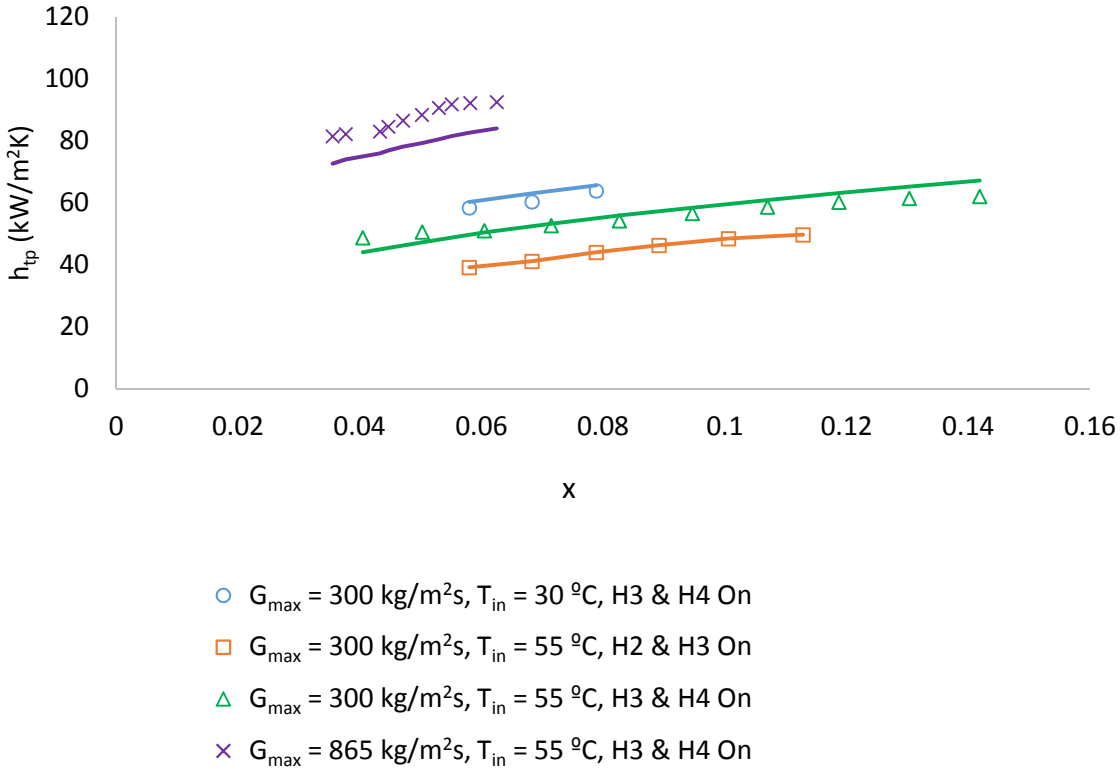

Figure 61 Two phase heat transfer coefficients prediction

The pressure drop correlation developed in Chapter 3 can predict pressure drop within ±20%, as shown in Figure 62. The mean absolute error is 4.8%.

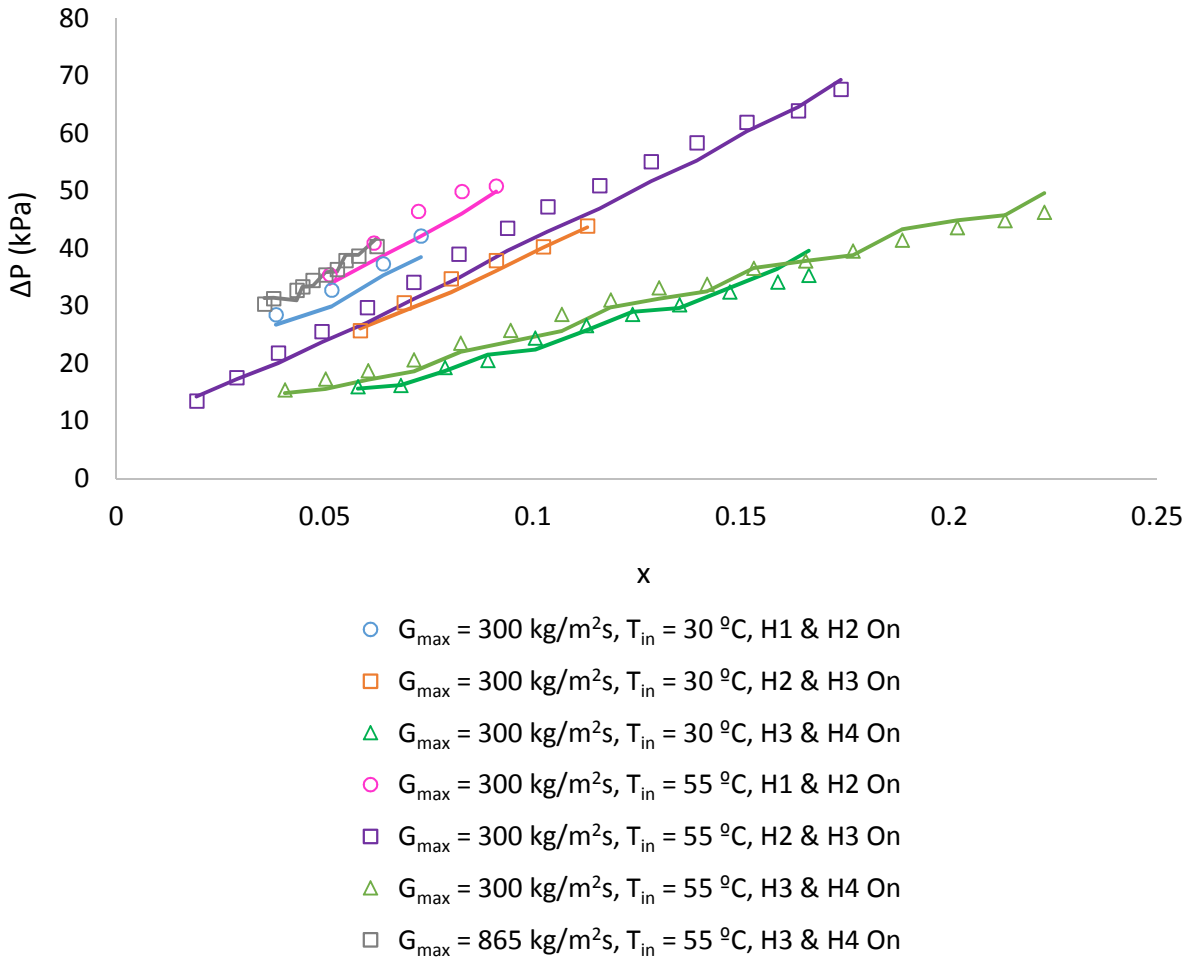

Figure 62 Pressure drop prediction

4.3 Flow Visualization

Flow direction is from left side to right side for all the flow visualization in this section. Figure 63 shows flow visualization at G_{max} = 300 kg/m^{2}s and T_{in} = 30 ºC with only heater No. 1 and No. 2 powered. For heat flux q_{eff}" = 74.6 W/cm^2 and beyond, a severe dryout condition occurs. Single phase liquid occupies a small corner of pin fin array, and two phase flow occupies a thin stripe area, as shown in Figure 63. The majority of pin fin array is in dryout condition, resulting in

sudden decrease in two phase heat transfer coefficient, and dramatic increase in wall superheat. Similar dryout conditions are seen for T_{in} = 55 ºC with only heater No. 1 and No. 2 on.

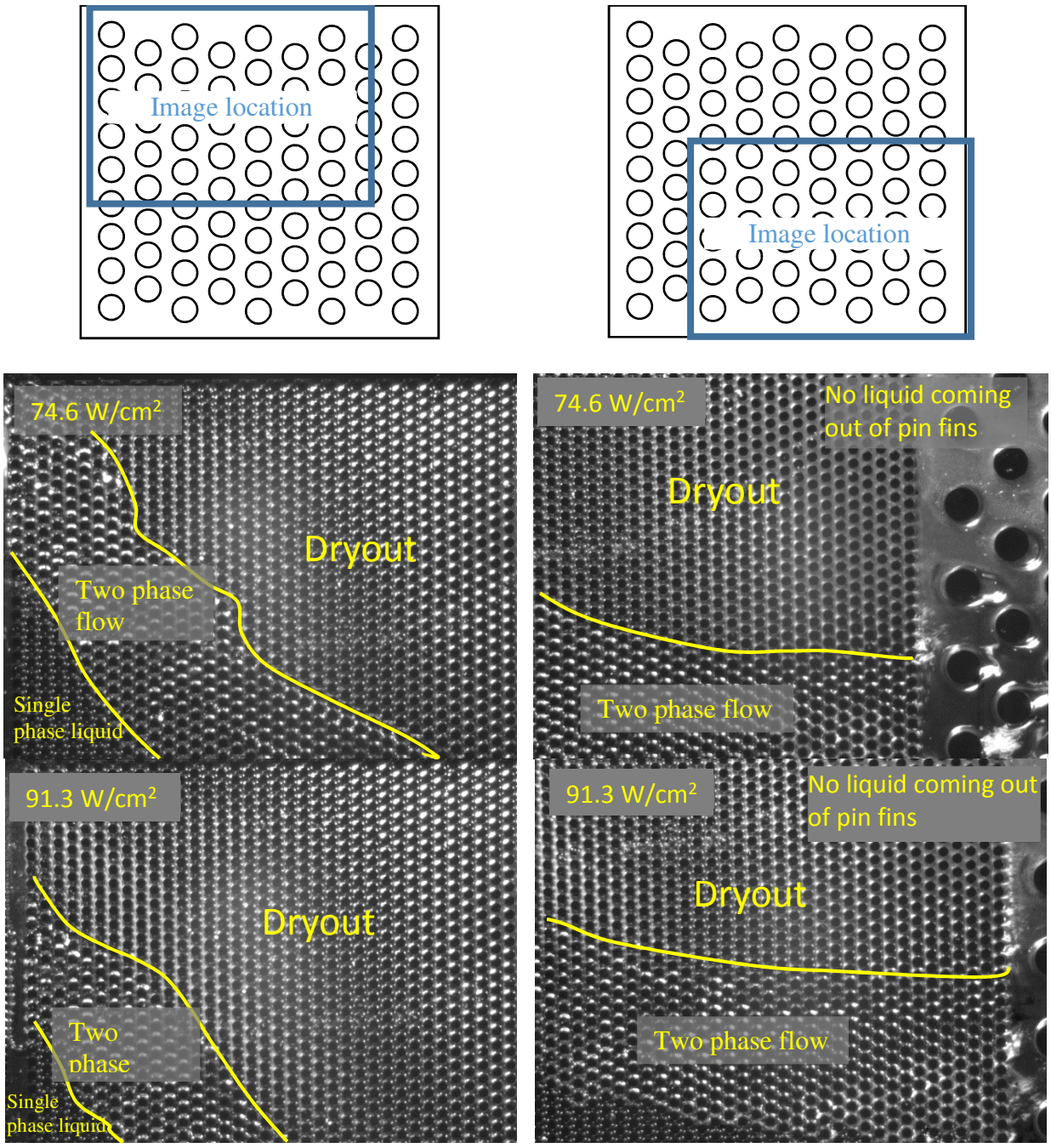

Figure 63 Flow visualization at G_{max} = 300 kg/m²s, T_{in} = 30 ºC, H1 & H2 on

Figure 64 presents flow visualization at G_{max} = 300 kg/m^{2}s and T_{in} = 30 ºC with heater No. 3 and No. 4 on. As heat flux increases, boiling area moves towards microgap inlet. At q_{eff}" = 86.5 W/cm^2, the zoomed in image shows that liquid films are surrounding circular pins. At some locations, liquid films are connected at adjacent pins. At q_{eff}" = 125.6 W/cm^2, liquid films also are still observed. As heat flux further increased to q_{eff}" = 164.3 W/cm^2, local dryout is seen, resulting in decreasing two phase heat transfer coefficient.

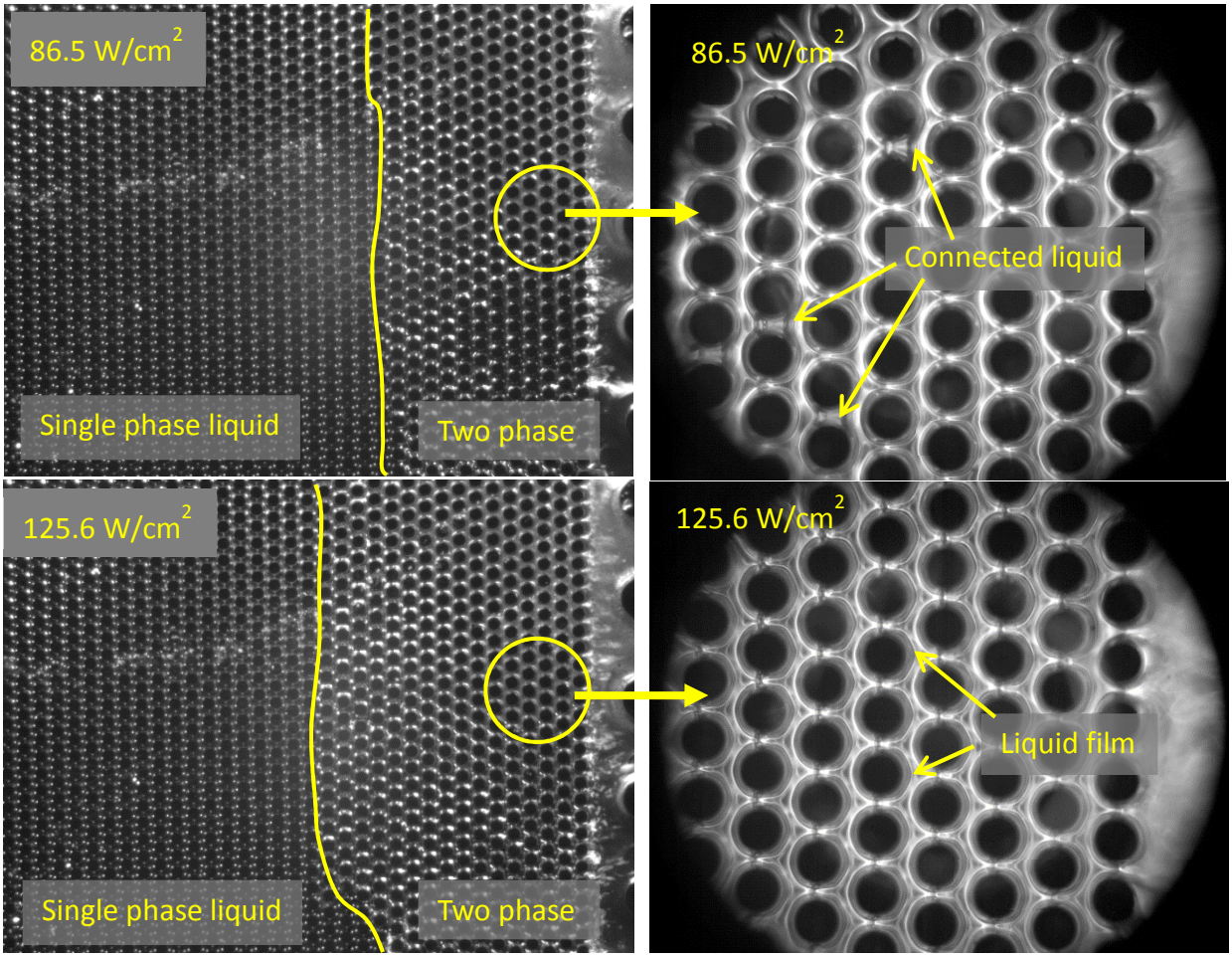

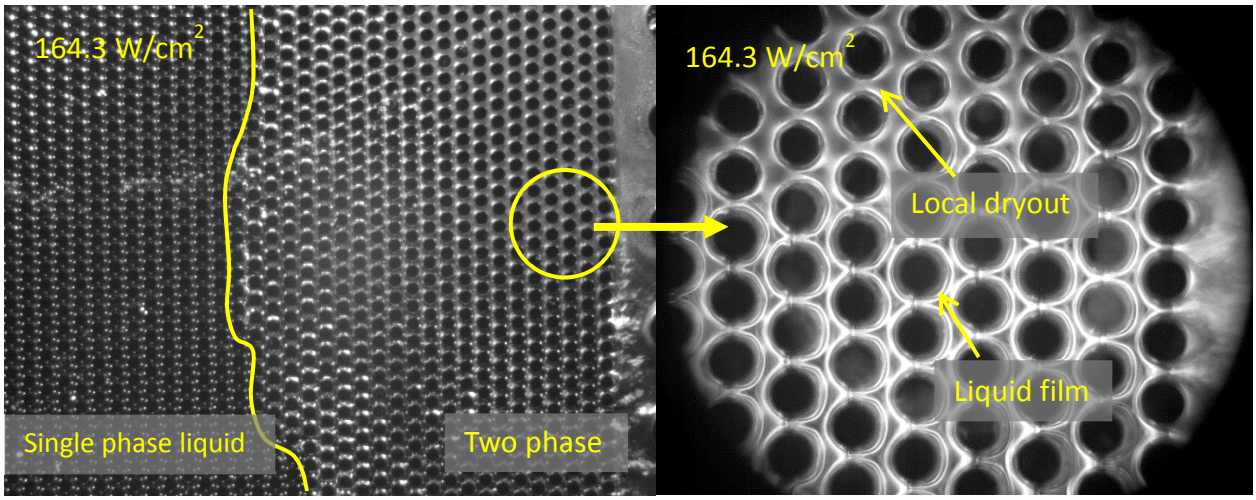

Figure 64 Flow visualization at G_{max} = 300 kg/m^{2}s, T_{in} = 30 ºC, H3 & H4 on

Figure 65 illustrates the flow at G_{max} = 300 kg/m^{2}s and T_{in} = 55 ºC, with heater No. 2 and No. 3 on. Locations of H2 and H3 are marked. The yellow solid curve separates the two phase and single phase liquid regions. At q_{eff}" = 26.5 W/cm^2, boiling covers less than half of the H3 area. Liquid films are observed to form, and are connected to large regions of liquid at certain locations, as seen in the zoomed in image. At q_{eff}" = 65.4 W/cm^2, the boiling covers all the H3 area, and liquid films surrounding pin fins become separate. From q_{eff}" = 26.5 to 65.4 W/cm^2, two phase heat transfer coefficient increases with heat flux due to increased boiling area and thinning of liquid films. As heat flux increased to q_{eff}" = 103.2 W/cm^2, liquid films are still seen to surround pin fins, and films at rear side of pin fins are slightly thicker than films at front side of pin fins, likely due to vapor phase acceleration. From q_{eff}" = 65.4 to 103.2 W/cm^2, two phase heat transfer coefficient shows less dependence on heat flux because no obvious change of flow regime is seen from zoomed in images. At heat flux q_{eff}" = 133.3 W/cm^2, local dryout is observed. Further increases of heat flux to q_{eff}" = 160.4 W/cm^2, larger dryout area is observed in zoomed in image. This explains the decrease trend of two phase heat transfer coefficient from q_{eff}" = 103.2 to 160.4 W/cm^2.

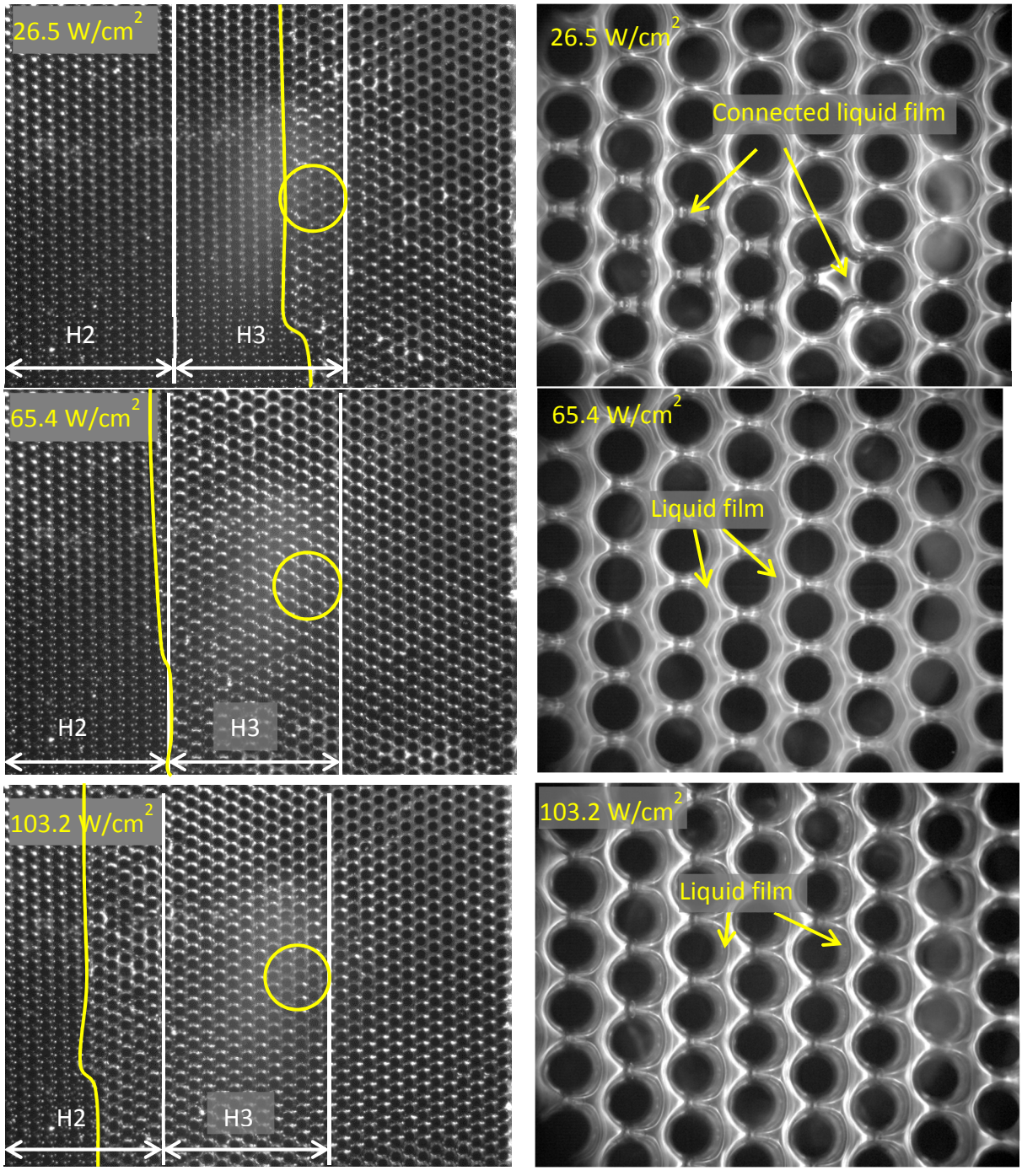
26.5 W/cm2
H2
H3
26.5 W/cm2
Connected liquid film
65.4 W/cm2
H2
H3
65.4 W/cm2
Liquid film
103.2 W/cm2
H2
H3
103.2 W/cm2
Liquid film

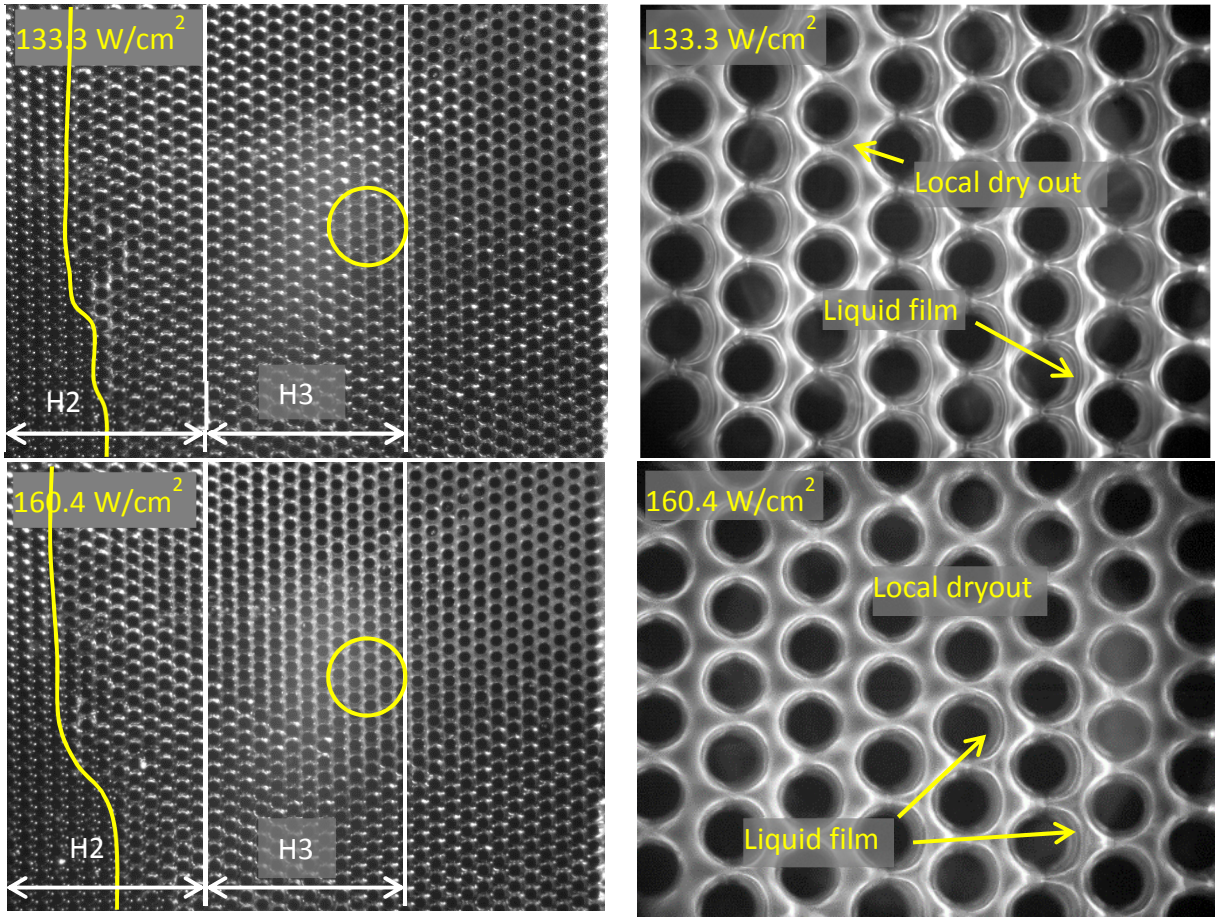

Figure 65 Flow visualization at G_{max} = 300 kg/m^{2}s, T_{in} = 55 ºC, H2 & H3 on

Figure 66 shows flow visualizations for G_{max} = 865 kg/m^{2}s and T_{in} = 55 ºC with heater No. 3 and No. 4 on. At the lowest heat flux q_{eff}" = 193.0 W/cm^2 that enables stable flow boiling and highest heat flux q_{eff}" = 281.8 W/cm^2 achieved before heater temperatures reach the safe limit of 130 ºC, there is no obvious change of flow patterns, as seen in the zoomed in images in Figure 66. Therefore two phase heat transfer coefficients do not vary dramatically with heat flux as shown in Figure 58.

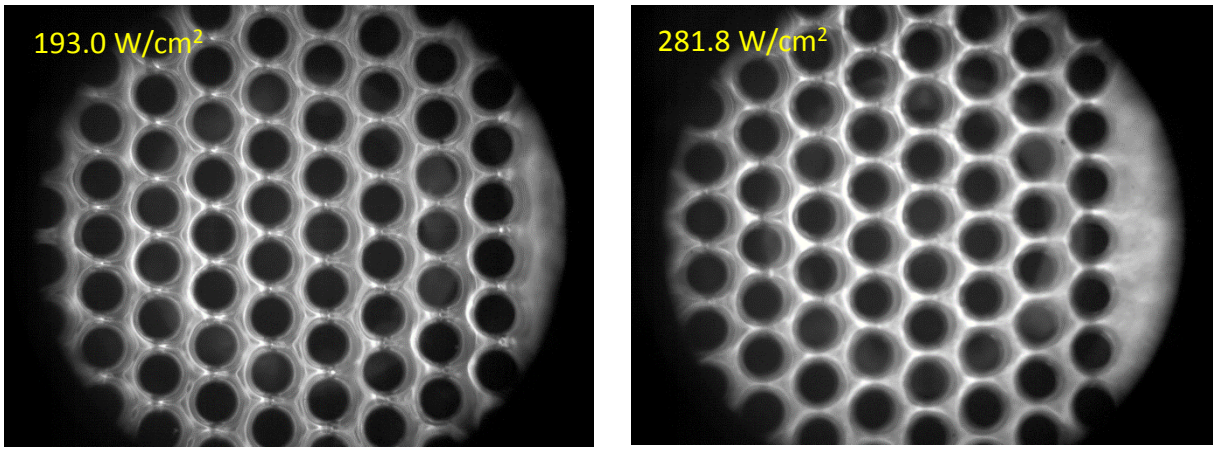

Figure 66 Flow visualization at G_{max} = 865 kg/m²s, T_{in} = 55 ºC, H3 & H4 on

4.4 Conclusions

The effects of heating locations are studied in this chapter, and the conclusions are as follows:

1. Change of heating locations has an important effect on flow boiling of water in pin fin enhanced microgap at reduced pressure.
2. As heating location moves from inlet to outlet, flow boiling becomes more stable, pressure drop becomes smaller, and two phase heat transfer coefficient becomes higher. When heating at H3 and H4, the upstream pin fins perform as pressure restrictors and aid to suppress unstable oscillations, resulting in better performance when heating at H3 and H4.
3. Two phase heat transfer coefficient also strongly depends on two phase flow patterns, as when all four heaters are uniformly powered.
4. The two phase heat transfer coefficient and pressure drop correlations developed in Chapter 3 are able to predict current result with a MAE of 9.8% and 4.8%, respectively.

CHAPTER 5. FLOW BOILING OF HFE-7200 IN PIN FIN ENHANCED MICROGAP

This chapter investigates flow boiling of dielectric liquid HFE-7200 in pin fin enhanced microgap. Two phase heat transfer coefficient and pressure drop are studied and compared with existing correlations. New two phase heat transfer coefficient and pressure drop correlations are also developed.

5.1 Experiment conditions

The experiment was performed using the same flow loop as for D.I. water tests. However, the fluid reservoir was open to atmosphere. Therefore, the system pressure at fluid reservoir is 101.3 kPa. HFE-7200 has a boiling point of 76 ºC at atmospheric pressure, which is acceptable for electronics cooling. Two mass fluxes and three inlet fluid temperatures were studied: G_{max} = 1270 kg/m^{2}s and 2511 kg/m^{2}s, and T_{in} = 20, 40 and 60 ºC. Heat fluxes were increased from 10 W/cm^2 by an increment of 10 W/cm^2 until heater temperature safe limit of 130 ºC is reached. Neither dryout nor critical heat flux condition was observed.

5.2 Results and Discussion

Pressure drop increases dramatically as flow transitions from single phase to two phase as heat flux increases, as shown in Figure 67 a) and Figure 68 a). Two phase pressure drop increases with exit vapor quality linearly, and there is no significant effects of inlet fluid temperatures on pressure drop, as seen in Figure 67 b) and Figure 68 b). This observation is different from D.I. water data due to different fluid thermodynamic properties. Both the liquid phase and vapor phase

densities and viscosities of HFE-7200 are higher than those of water, resulting in higher pressure drops for HFE-7200. Thus the effects of viscosity variation due to fluid temperature is not as noticeable for HFE-7200 as for water.

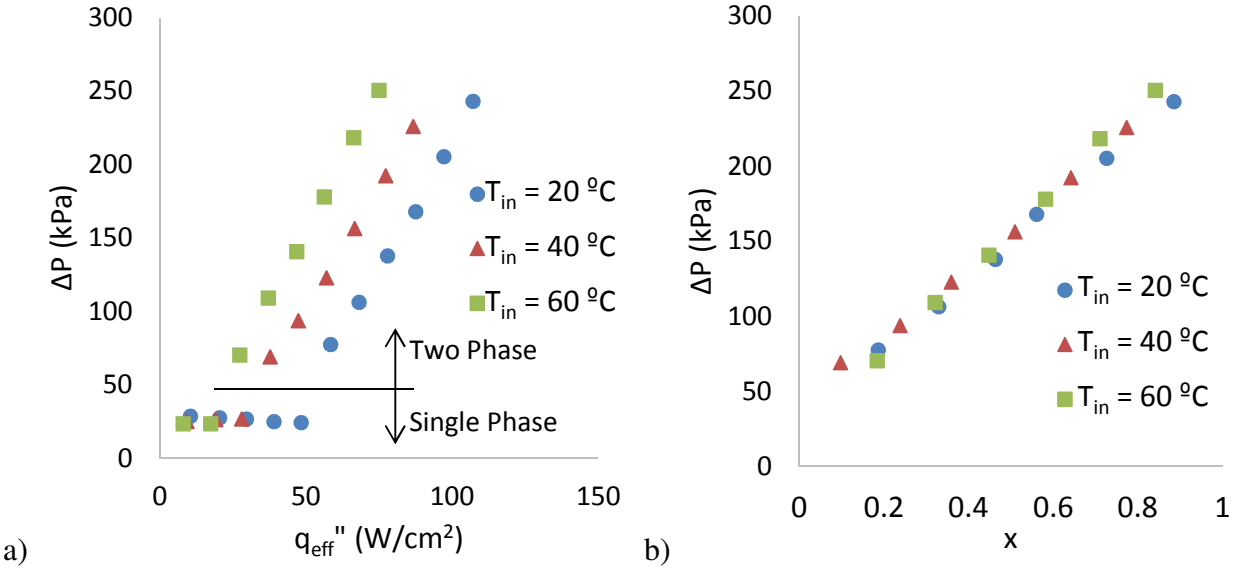

Figure 67 Pressure drop at G_{max} = 1270 kg/m²s: a) ΔP vs q_{eff}"; b) ΔP vs x

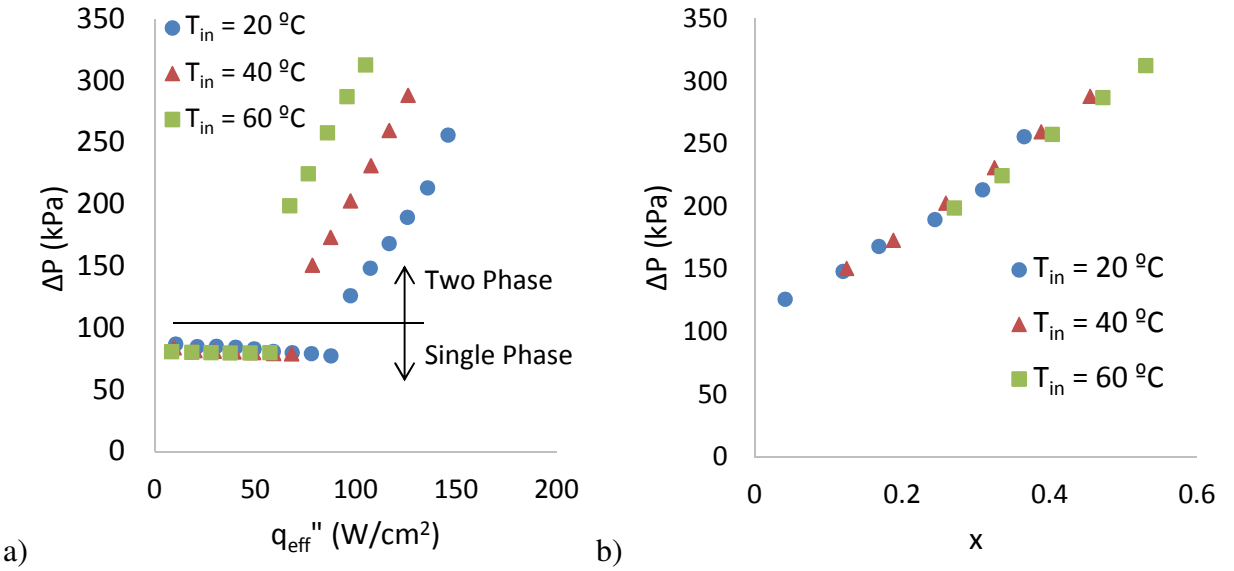

Figure 68 Pressure drop at G_{max} = 2511 kg/m²s: a) ΔP vs q_{eff}"; b) ΔP vs x

Figure 69 shows exit vapor quality, and the maximum exit vapor quality achieved for G_{max} = 1270 kg/m^{2}s is 0.84, and for G_{max} = 2511 kg/m^{2}s is 0.53 without achieving critical heat flux. As for water data using the same device, the maximum exit vapor quality is 0.18 and large area of dryout is seen and critical heat flux is encountered when further increase in exit vapor quality. The effect of inlet fluid temperature is similar as for water data. Higher inlet fluid temperatures result in higher exit vapor quality at the same heat flux condition, which is as expected.

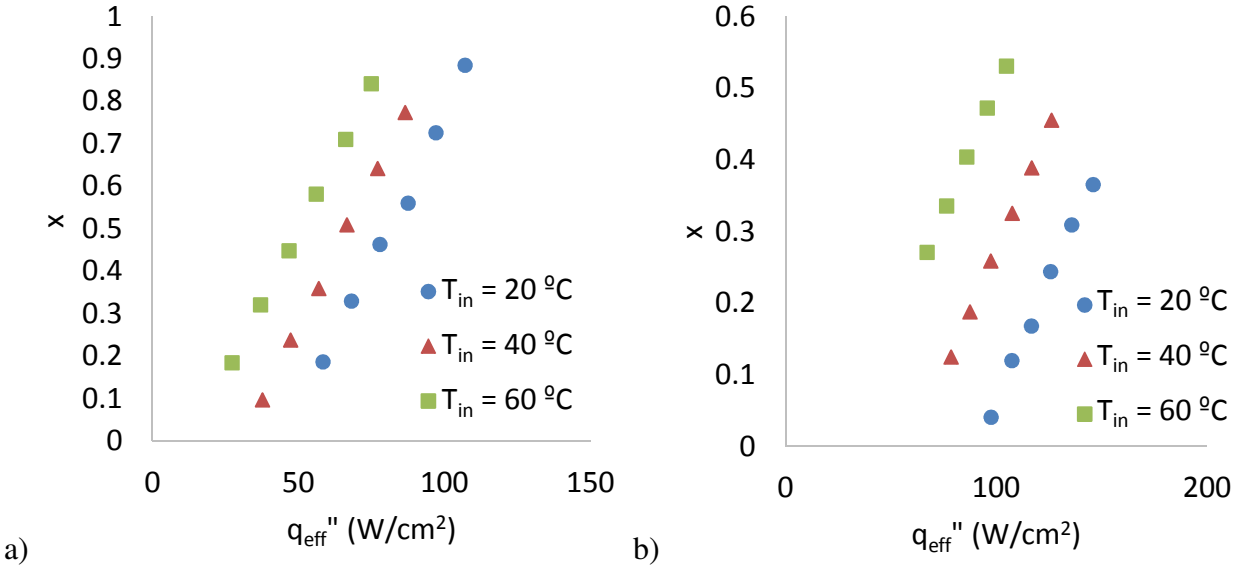

Figure 69 Exit vapor quality at: a) G_{max} = 1270 kg/m^{2}s; b) G_{max} = 2511 kg/m^{2}s

The wall temperatures at G_{max} = 1270 kg/m^{2}s and G_{max} = 2511 kg/m^{2}s are shown in Figure 70 a) and b), respectively. Wall temperature is evaluated in the last quarter of pin fin arrays closet to microgap outlet where heater No. 4 is located. At lower mass flux, there is a noticeable change of the slope of T_w - q_{eff}" curve at the point where boiling starts. At higher mass flux, the change of slope of T_w - q_{eff}" curve after the point where boiling starts is not as noticeable, because only part of H4 area is in boiling even at the highest tested heat flux.

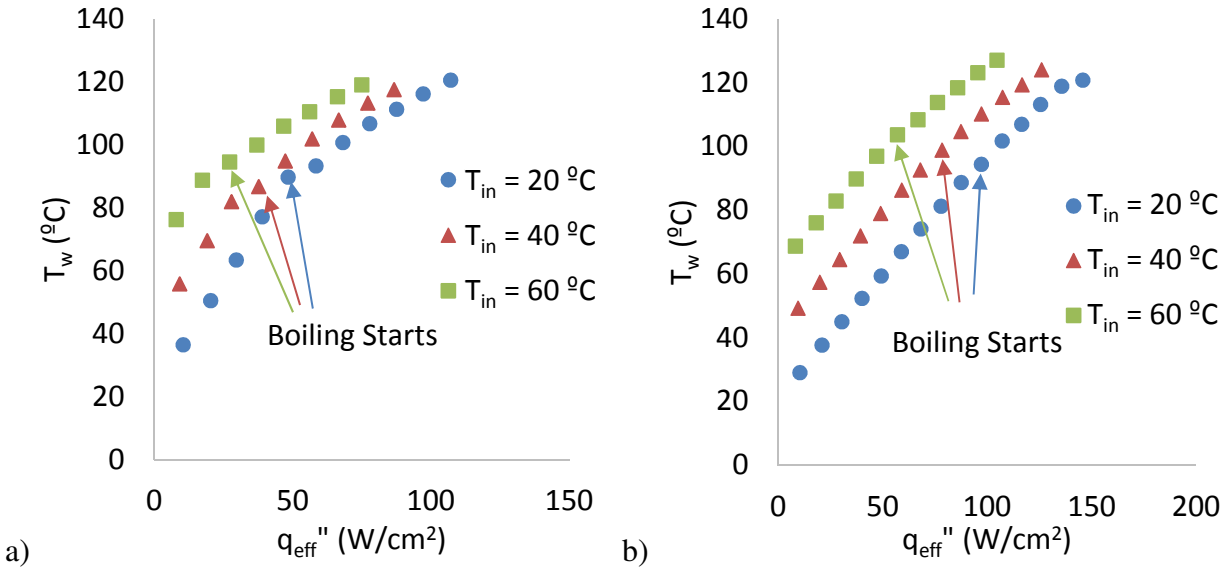

Figure 70 Wall temperature at: a) G_{max} = 1270 kg/m²s; b) G_{max} = 2511 kg/m²s

Boiling curve at G_{max} = 1270 kg/m²s and G_{max} = 2511 kg/m²s are shown in Figure 71 a) and b), respectively. Wall superheat increases with heat flux almost linearly indicating no dryout condition. When dryout occurs, a slight increase in heat flux can lead to a large increase in wall super heat, resulting in decreased slope of boiling curve. At the same heat flux, higher inlet fluid temperature yields higher wall superheat, due to lower two phase heat transfer coefficient.

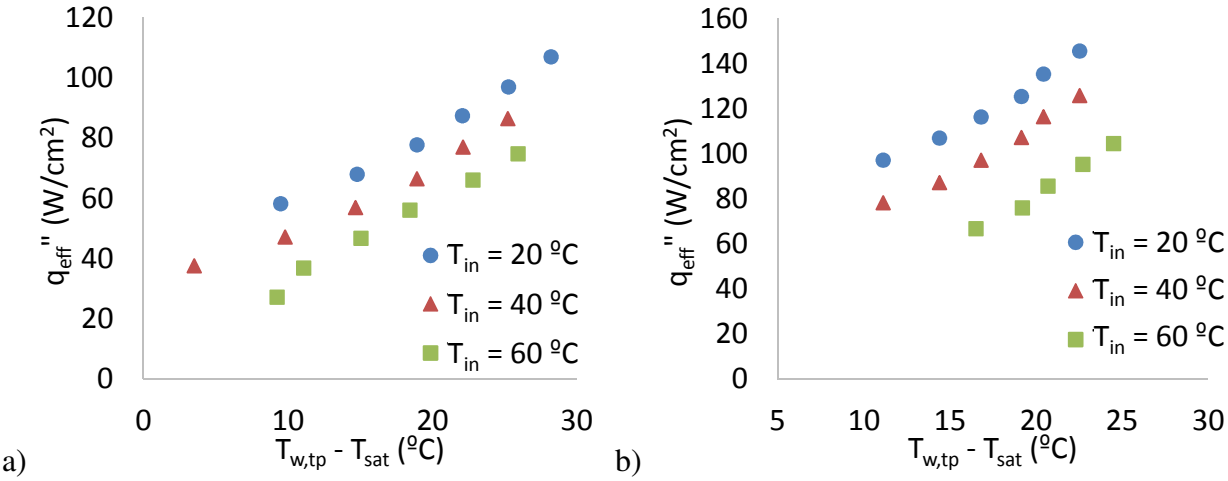

Figure 71 Boiling curve at: a) G_{max} = 1270 kg/m²s; b) G_{max} = 2511 kg/m²s

Figure 72 and Figure 73 compares two phase heat transfer coefficients for G_{max} = 1270 kg/m^{2}s and G_{max} = 2511 kg/m^{2}s. Two phase heat transfer coefficient is calculated using the H4 temperature, and H4 area is where boiling occurs. There is a sharp decrease in two phase heat transfer coefficient at low quality. When exit vapor quality is beyond 0.4, two phase heat transfer coefficient falls into a plateau region and dependence on vapor quality becomes less prominent.

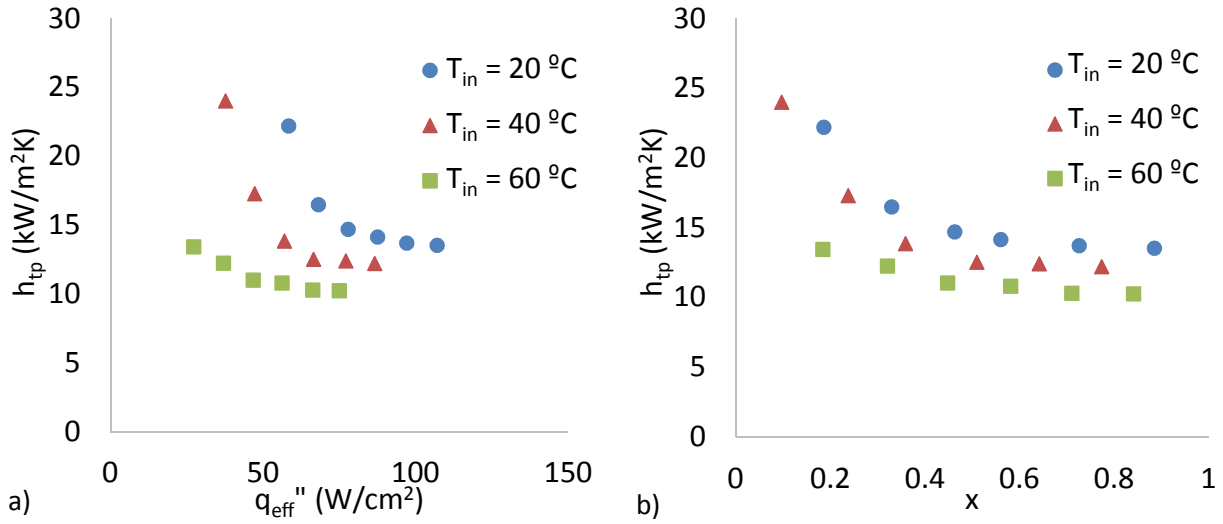

Figure 72 Two phase heat transfer coefficient at G_{max} = 1270 kg/m^{2}s: a) h_{tp} vs q_{eff}"; b) h_{tp} vs x

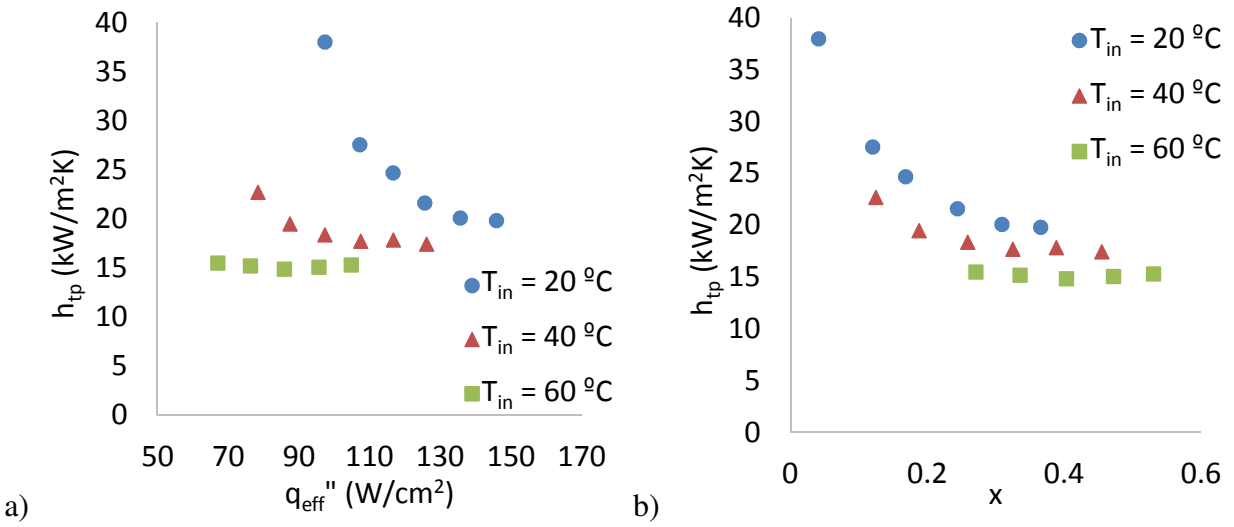

Figure 73 Two phase heat transfer coefficient at G_{max} = 2511 kg/m^{2}s: a) h_{tp} vs q_{eff}"; b) h_{tp} vs x

The findings agree with the work by Reeser et al [32], and average heat transfer coefficient from Reeser et al [32] is shown in Figure 75 for comparison. The difference of Reeser et al's work from current study is that they utilized square pin fin with inline and staggered arrangement in copper microgap, and mass flux range studied is less than half of mass fluxes studied in current work. They reported average heat transfer coefficient instead of two phase heat transfer coefficient. The two phase heat transfer coefficient values are higher than average heat transfer coefficient reported by Reeser et al due to above mentioned differences, and generally follow the same trend. The decrease of two phase heat transfer coefficient after the plateau region as exit vapor quality further increase is not observed in current study. Average heat transfer coefficients are calculated and presented in Figure 74 for comparison.

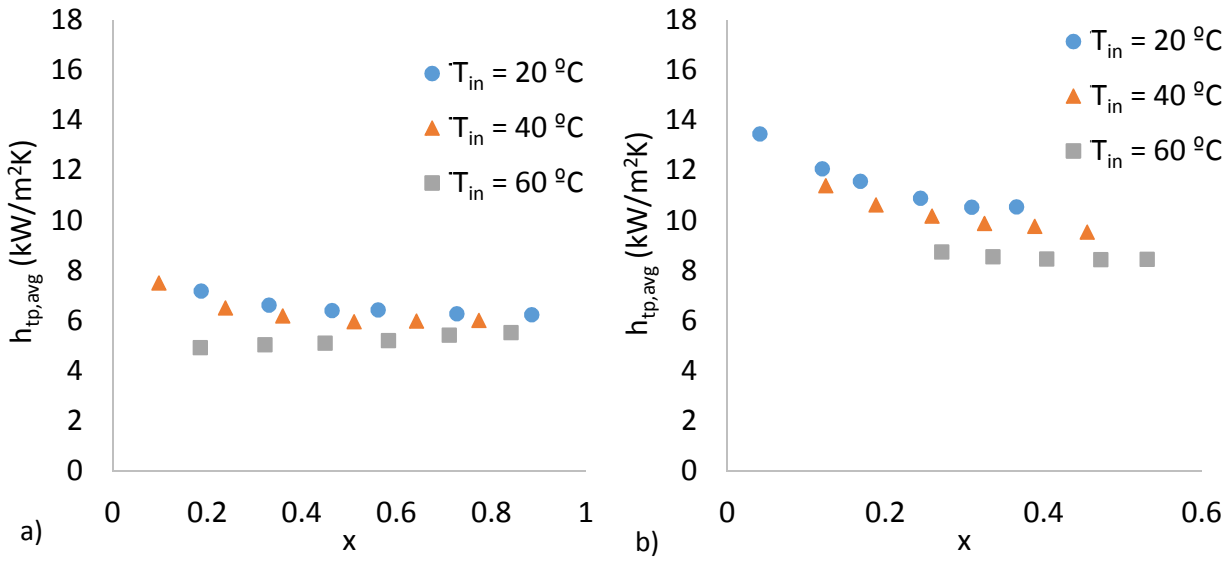

Figure 74 Average two phase heat transfer coefficient: a) G_{max} = 1270 kg/m²s, b) G_{max} = 2511 kg/m²s

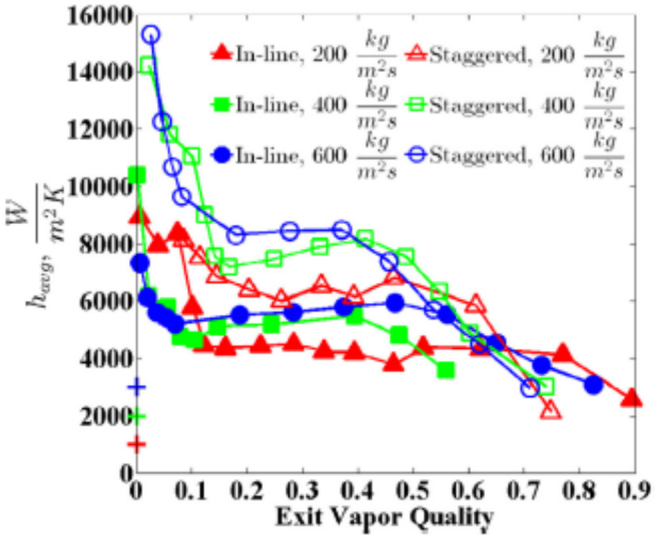

Figure 75 Average heat transfer coefficient vs exit vapor quality, Reeser et al [32]

Figure 76 compares single phase heat transfer coefficient calculated in H1 area and two phase heat transfer coefficient in H4 area. Heat transfer coefficients are improved by 13% - 200% when fluids travels from single phase region to two phase region.

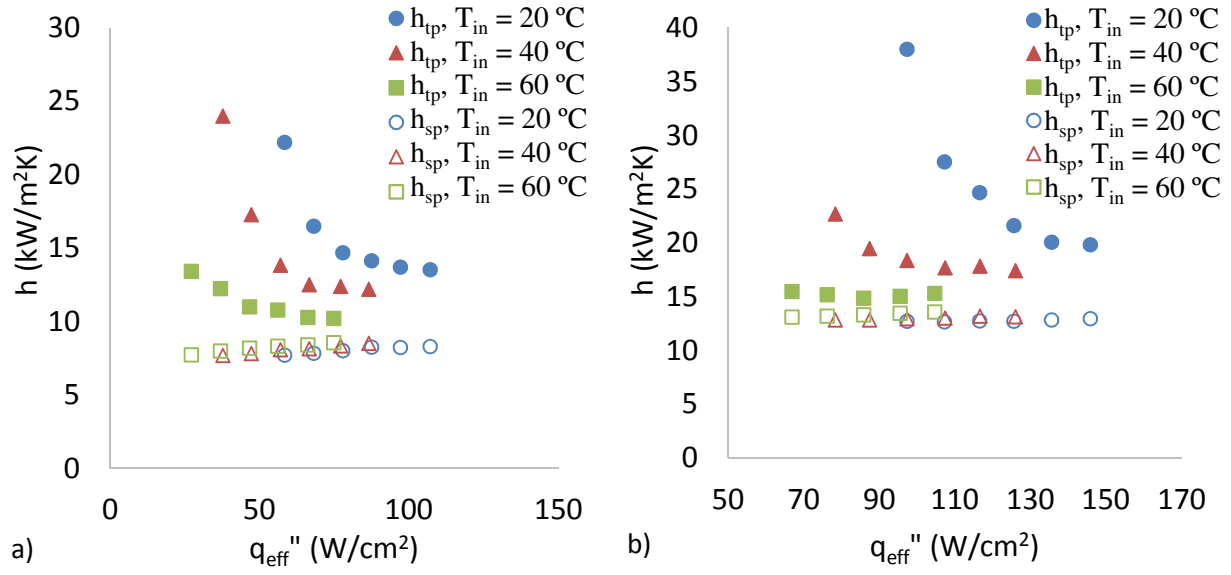

Figure 76 Comparison of h_{sp} and h_{tp}: a) G_{max} = 1270 kg/m²s, b) G_{max} = 2511 kg/m²s

5.3 Two Phase Heat Transfer Coefficient Correlation

Reeser et al. developed a heat transfer correlation for HFE-7200 flowing through square pin array [32]. The correlation is in the same format of water correlation discussed in Chapter 2, except a modified ζ,

$$\zeta = 6\exp(-14.15x) - 3.63x^3 + \left(\frac{45}{G_{max} + 88}\right)^{1/2} \tag{60}$$

This correlation yields negative two phase heat transfer coefficients for current study. ζ has a negative coefficient in the second term in the right side of the above equation. The mass flux G_{max} studied in this work is larger, resulting in smaller third term in right side of the above equation, and negative ζ and negative predicted two phase heat transfer coefficient.

Two phase heat transfer coefficient correlation in Equation (21) developed by Qu and Siu-Ho was based on inline square shape copper pin-fin using water for exit vapor quality up to 0.28 [15]. This correlation can predict decreasing two phase heat transfer coefficient vs exit vapor quality. However, the exit vapor quality of current study is beyond 0.28, and this correlation predicts two phase heat transfer coefficients as high as the order of 10^9 kW/m^{2}K, which is significantly over predicting and off the correct range.

Based on current data, a new two phase heat transfer correlation for HFE-7200 flowing through circular pin-fin enhanced microgap proposed to be

$$h_{tp} = \mathrm{F}h_{sp} \tag{61}$$

following the same format used in Chapter 2. h_{sp} is the single phase heat transfer coefficient calculated using the same correlation in Chapter 2. After multiple efforts, the factor F is determined to be

$$F = 5x^{-0.3}\left(\frac{C_P(T_{sat} - T_{in})}{h_{vap}}\right)^{0.4} \tag{62}$$

The comparison of predicted two phase heat transfer coefficient and measured two phase heat transfer coefficient is shown in Figure 77, and the mean absolute error is 5%.

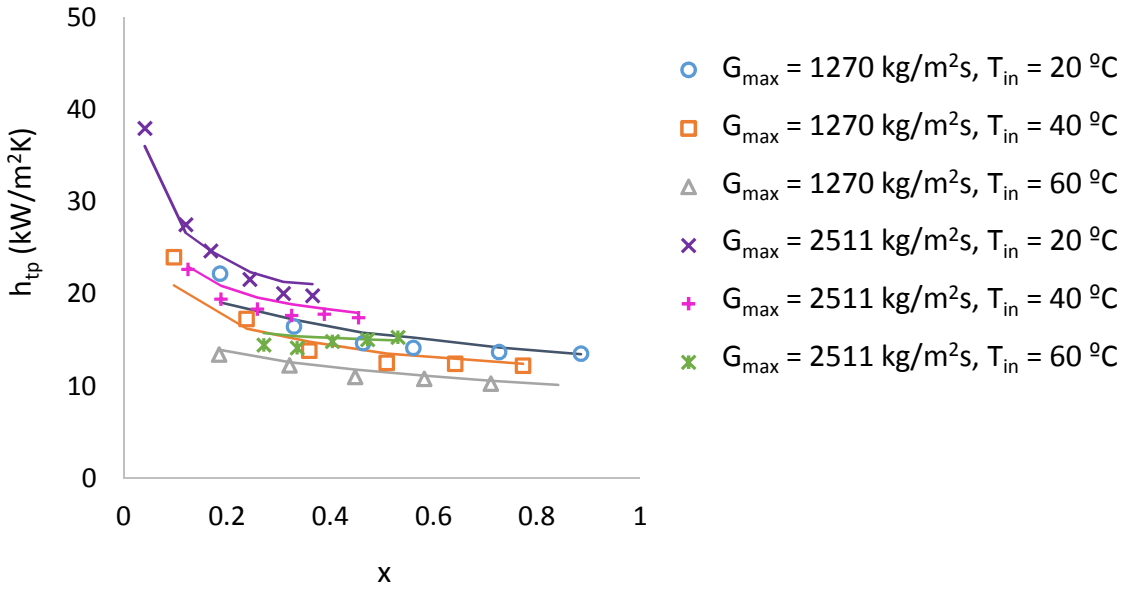

Figure 77 New two phase heat transfer coefficient correlation for HFE-7200

5.4 Two Phase Pressure Drop Correlation

The predicted two phase pressure drops using correlations from Table 5 are shown in Figure 78 to Figure 82. The Reeser et al correlation for HFE-7200 is different from the correlation

for water. The two phase pressure drop term is multiplied by a constant $\lambda = 0.044$, and the constant C in the two phase multiplier equals 5 instead of 8.

$$\Delta P_{tp,f} = \sum_{i=N_{tr}}^{N_t} \lambda f_{sp,i} \frac{G_{max}^2 (1-x)^2}{2\rho_f} \phi_l^2 \tag{63}$$

Figure 83 shows pressure drop predictions using the newly developed correlation in Chapter 2. From these figures, the Lockhart and Martinelli (viscous liquid – viscous vapor) correlation, the Lockhart and Martinelli (viscous liquid – turbulent vapor) correlation, and the newly developed correlation for water can predict the trend with reasonable accuracy. Qu and Mudawar, Reeser et al. correlations yield the worst predictions. The pressure drop correlation developed for water in Chapter 2 can be improved by modifying the factor C in two phase multiplier to include the vapor phase density. The major difference in properties which affects pressure drop of HFE-7200 and water is vapor density. The vapor density of HFE-7200 is about 35 times that of water, which is not included in the factor C from Chapter 2. The factor C is found to be

$$C = 9.7 Re_l^{-0.4} \left(\rho_{HFE7200,v} / \rho_{water,v}\right)^{0.27} \tag{64}$$

The modified factor C can predict current HFE-7200 pressure drop data with MAE = 11.7%. The results are shown in Figure 84.

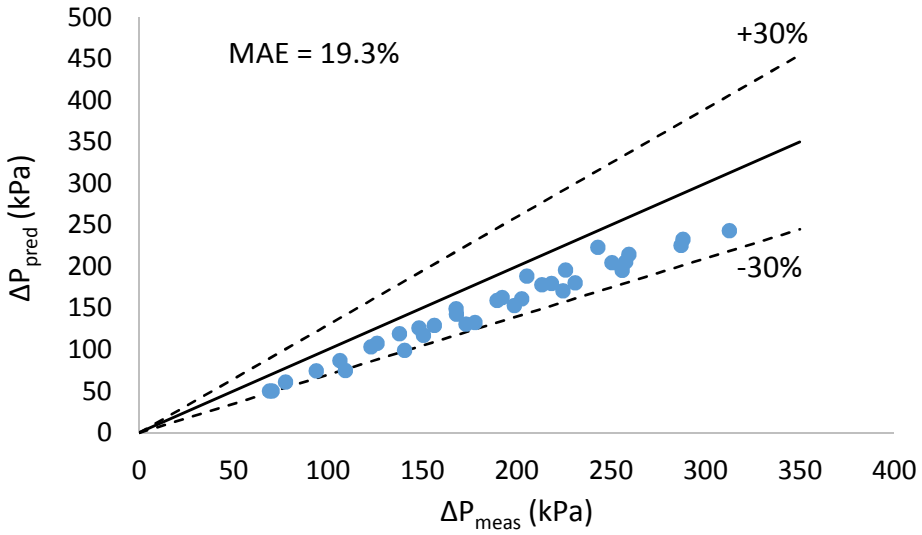

Figure 78 Pressure prediction using Lockhart and Martinelli (viscous liquid-viscous vapor) correlation

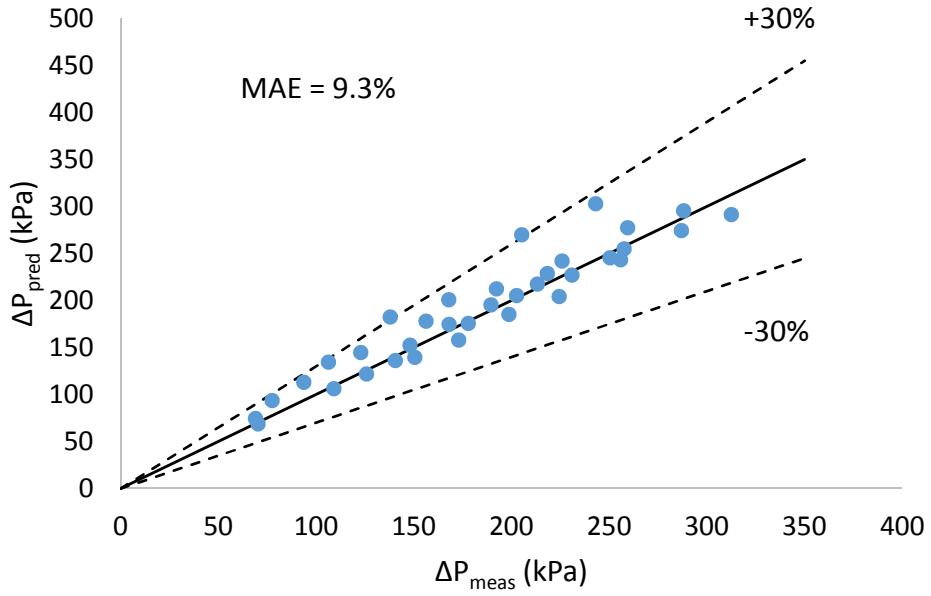

Figure 79 Pressure prediction using Lockhart and Martinelli (viscous liquid-turbulent vapor) correlation

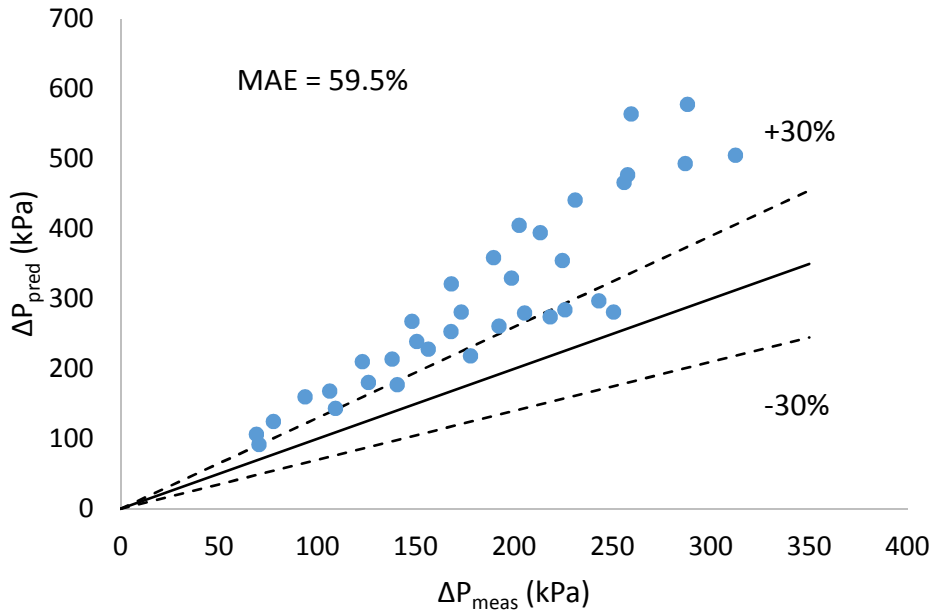

Figure 80 Pressure prediction using Krishnamurthy and Peles correlation

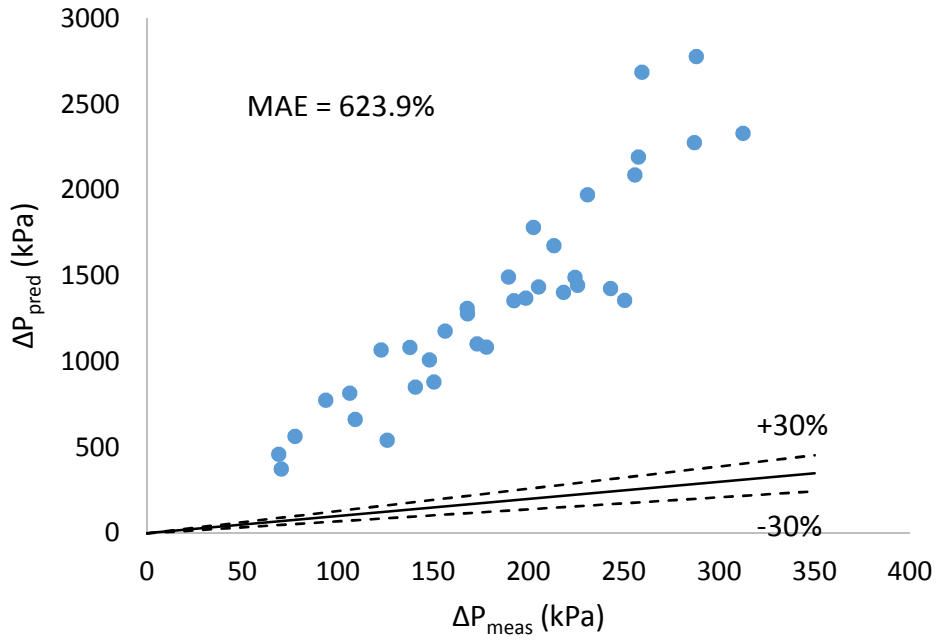

Figure 81 Pressure prediction using Qu and Mudawar correlation

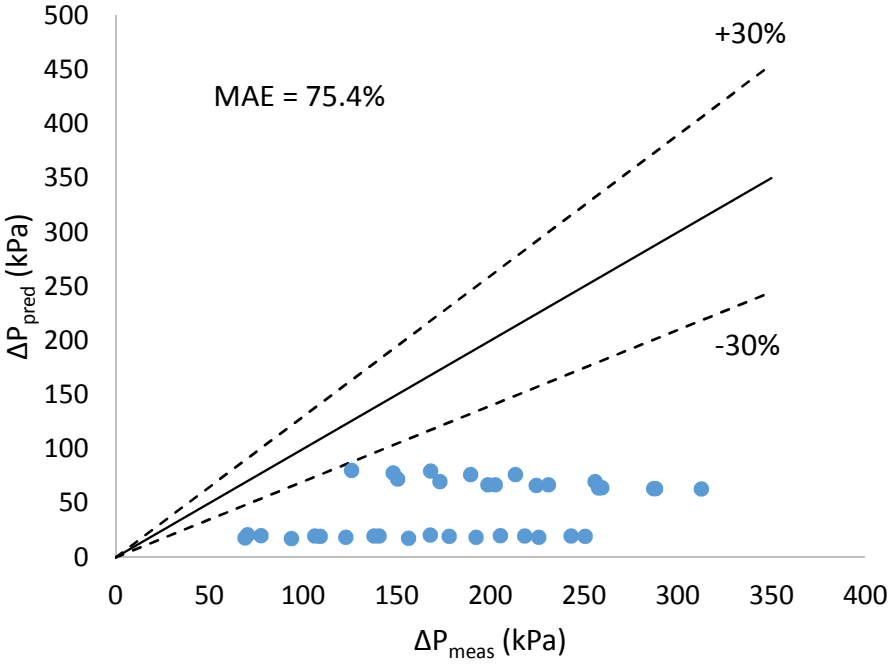

Figure 82 Pressure prediction using Reeser et al. correlation

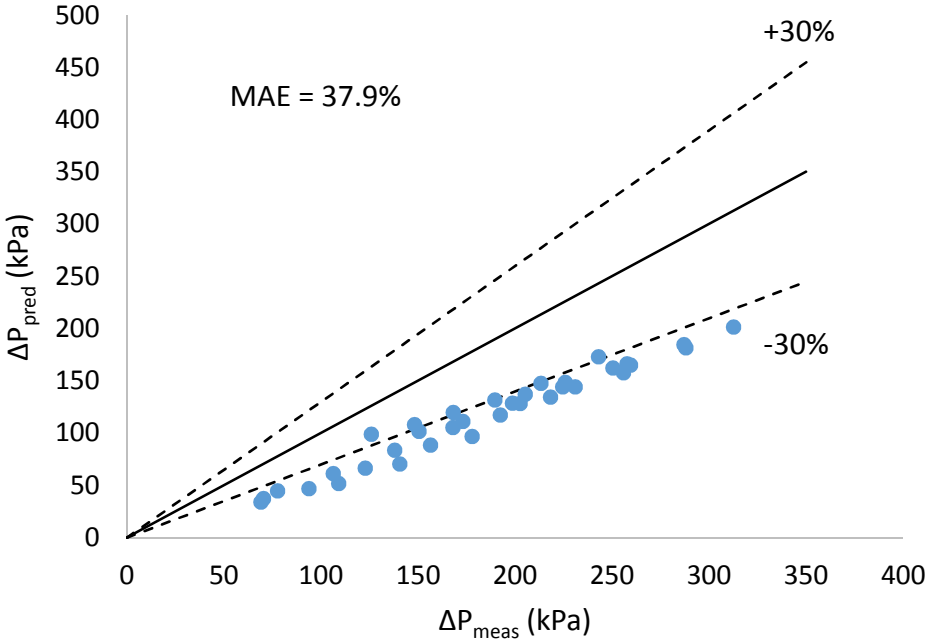

Figure 83 Pressure prediction using water correlation

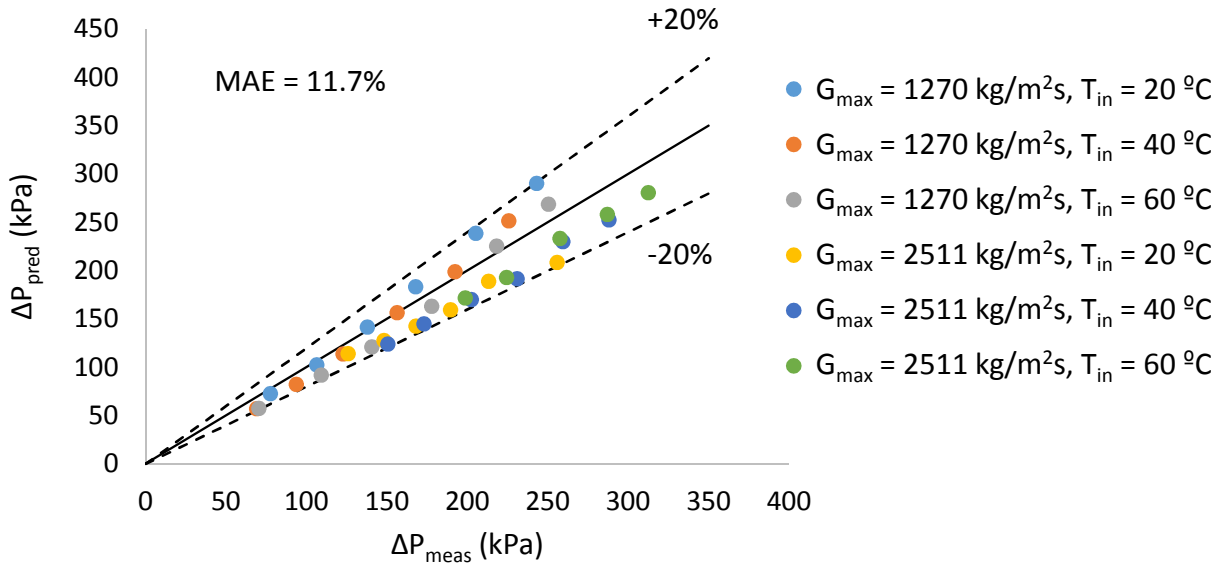

Figure 84 Pressure prediction using new correlation for HFE-7200

5.5 Flow Visualization

Figure 85 and Figure 86 illustrate flow visualization at G_{max} = 1270 kg/m^{2}s and T_{in} = 20 ºC, and G_{max} = 2511 kg/m^{2}s and T_{in} = 40 ºC, respectively. Boiling area is in the downstream side of pin fin array, and moves towards upstream as heat flux increased. For the higher mass flux, the boiling area is not able to cover the entire H4 area even at the highest heat flux tested. The zoomed in images are shown in Figure 87 and Figure 88. For G_{max} = 1270 kg/m^{2}s, T_{in} = 20 ºC, and q_{eff}" = 58.3 W/cm^2, bubble nucleation is observed in upstream part of boiling area. In downstream part of boiling area, liquid films are seen to surround pin fins with a sharp tail wake. At increased heat flux of 107.0 W/cm^2, bubble nucleation at upstream is not seen, and liquid films are also observed to surround pin fins. The film is thicker at the rear side of pin fin than at front side. For G_{max} = 2511 kg/m^{2}s, T_{in} = 40 ºC and q_{eff}" = 78.4 W/cm^2, boiling occurs only in one row of pins. At q_{eff}"

= 126 W/cm^2, liquid films with sharp tail wakes are seen to surround pin fins. Dryout is not observed for all the tested conditions.

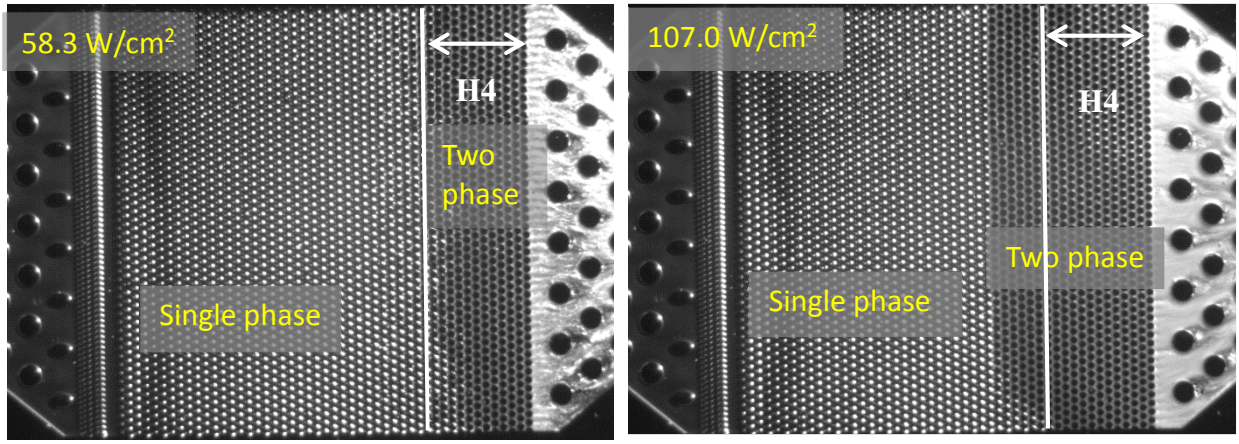

Figure 85 Large area flow visualization at G_{max} = 1270 kg/m^{2}s and T_{in} = 20 ºC

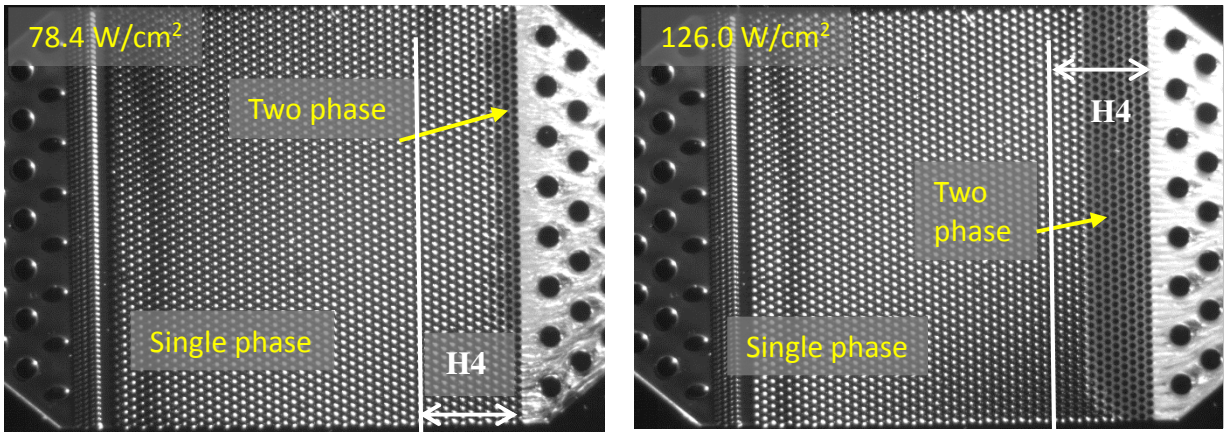

Figure 86 Large area flow visualization at G_{max} = 2511 kg/m^{2}s and T_{in} = 40 ºC

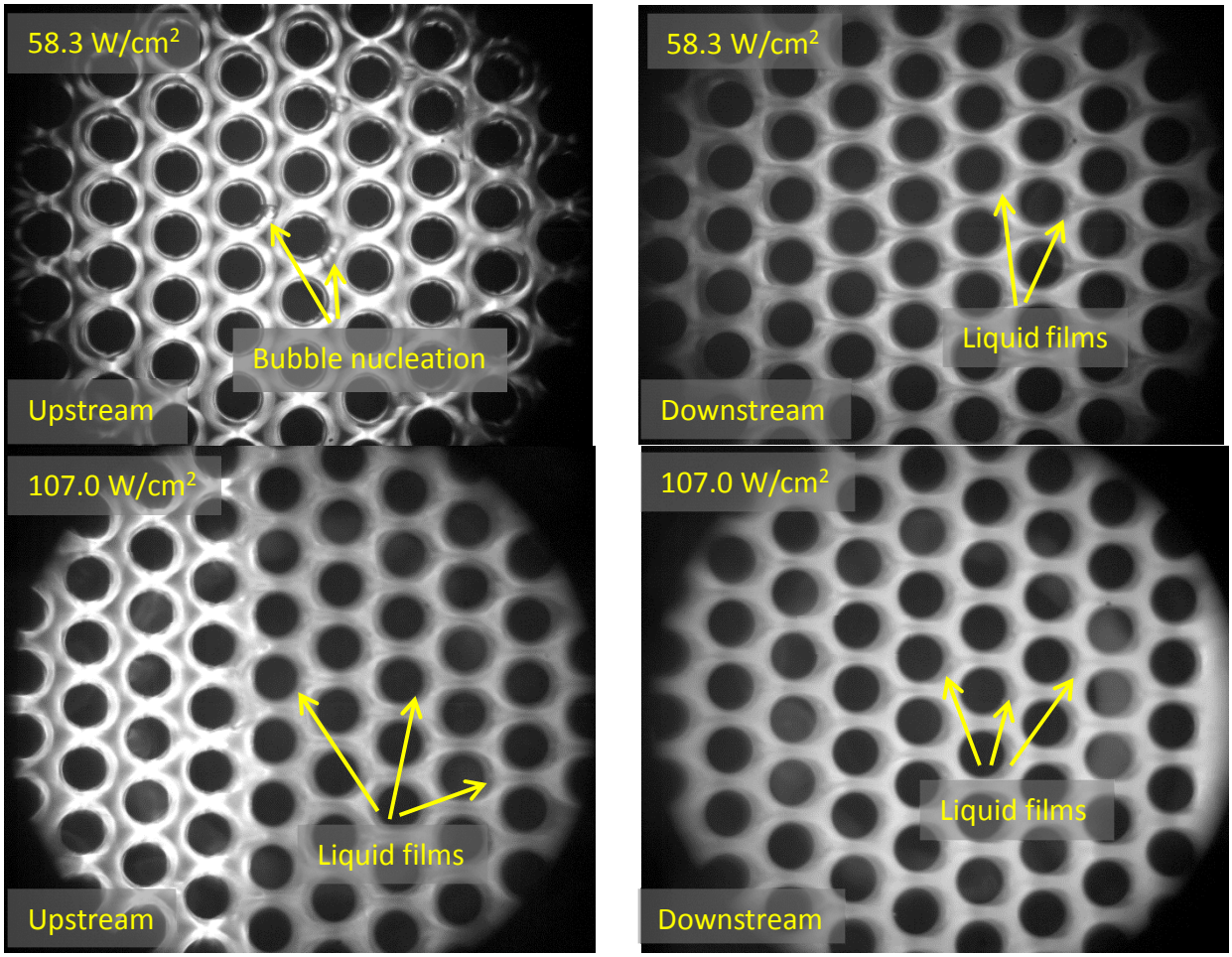

Figure 87 Zoomed in flow visualization at G_{max} = 1270 kg/m²s and T_{in} = 20 ºC

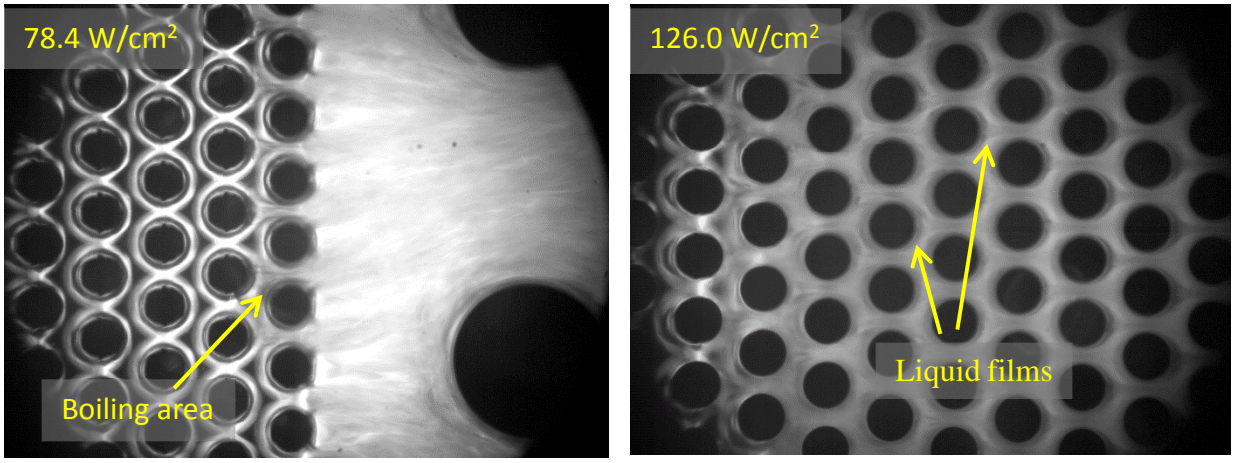

Figure 88 Zoomed in fow visualization at G_{max} = 2511 kg/m²s and T_{in} = 40 ºC

5.6 Conclusions

This chapter studies flow boiling of HFE-7200 in pin fin enhanced microgap, and the conclusions are as follows:

1. Two phase pressure drop is independent of inlet fluid temperature.
2. In the tested range of mass flux and heat flux, wall superheat increases linearly with heat flux, indicating no dryout occurred.
3. Two phase heat transfer coefficient shows a sharp decrease at low exit vapor quality, and when exit vapor quality is beyond 0.4, the dependence of two phase heat transfer coefficient on heat flux is less prominent.
4. The existing two phase heat transfer coefficient correlations are not able predict current results within a reasonable range. A new two phase heat transfer coefficient correlation is proposed.
5. The existing pressure drop correlations can predict current results within a reasonable range. A modified pressure drop correlation is proposed to improve accuracy.
6. Boiling area is at downstream side of pin fin array, and moves towards upstream as heat flux increases. Liquid films are observed to surround pin fins, with sharp tail wakes.

CHAPTER 6. CONCLUSIONS AND FUTURE WORK RECOMMENDATIONS

This chapter concludes this study, and a few recommendations on future work are made based on findings from this work.

6.1 Conclusions

6.1.1 Heat Transfer Characteristics

Two phase heat transfer behavior strongly depends on flow patterns for water. Dryout significantly degrades two phase heat transfer coefficient, which is not desired. For water without dryout condition, two phase heat transfer coefficients generally increase with heat fluxes within the tested mass flux and heat flux ranges. Conversely, for HFE-7200, two phase heat transfer coefficients decrease with heat fluxes within the tested mass flux and heat flux ranges. Two phase heat transfer coefficient shows a sharp decrease at low exit vapor quality, and when exit vapor quality is beyond 0.4, the dependence of two phase heat transfer coefficient on heat flux is less prominent. Both increasing and decreasing trends of two phase heat transfer coefficients versus heat flux were reported in previous work for water [13, 15, 32], and only decreasing trend was reported for HFE-7200 in literature [32]. For water, the two phase heat transfer coefficient correlations developed by Krishnamurthy and Peles [13] and Reeser et al [32] are compared with current data, and they are not able to predict current data satisfactorily. New two phase heat transfer coefficient correlation is developed for current water data, with a MAE of 6.2%. For HFE-7200, two phase heat transfer coefficient correlations developed by Qu and Siu-Ho [15] and Reeser et al

[32] are examined, because these correlations can predict decreasing trend of h_{tp}. However, predictions of these correlations are significantly off range for current HFE-7200 data. Thus, a new two phase heat transfer coefficient correlation for HFE-7200 is developed which can predicts current data with a MAE of 5%. Two phase heat transfer coefficients of water is higher than two phase heat transfer coefficient of HFE-7200 due to better thermodynamic properties. The specific heat and latent heat of vaporization of water at saturation condition of atmospheric pressure are 3.2 and 20.0 times those of HFE-7200, respectively, which makes water better at heat absorption for both single phase liquid flow and two phase flow.

Critical heat flux is only observed for water at VFR = 9 mL/min and all tested inlet temperatures for both sparse and dense devices, within the tested mass flux and heat flux ranges. Dryout is observed for testing conditions when critical heat flux is reached, and also at VFR = 26 mL/min, T_{in} = 30 °C for sparse device, within the tested mass flux and heat flux ranges. Both increased flow rate and inlet fluid temperatures delay critical heat flux conditions. It is obvious that when flow rate is higher, more heat can be carried away, resulting in higher critical heat flux. When inlet fluid temperature is increased, or fluid is at saturated/near saturated condition, it also enables fluid to absorb more heat. When T_{in} = 30 °C, fluid undergoes sensible heating from 30 °C to 55 °C, and the heat absorbed per mass unit is C_p*(55°C − 30°C) = 104.6 kJ/kg. When T_{in} = 55 °C, which is a saturated inlet condition, the heat absorbed per mass unit is h_{vap} = 2370 kJ/kg, which is considerably larger than the T_{in} = 30 °C case. Thus, higher inlet fluid temperature assists to delay critical heat flux. The highest effective heat fluxes achieved before heater temperature reaches 130 °C are 300 W/cm^2 and 146 W/cm^2, for water and HFE-7200, respectively, which also indicates that water is better at heat absorption than HFE-7200.

Although water has attractive thermodynamic properties as a coolant, water is not as chemically stable as HFE-7200. Corrosion of flow loop components was observed. Before experiment conducted in this work, the flow loop utilized brass tubing, and after long period of experiment with water, brass was corroded and debris were collected in the filter and also in the devices. This caused device clogging since the space between pin fins are very limited. Thus using water as coolant posts requirement for flow loop component materials. Stainless steel and plastic are recommended for water.

6.1.2 Pressure Drop Characteristics

The two phase pressure drop for water is below 80 kPa, and for HFE-7200 is from 69 kPa to 312 kPa, within the tested mass flux and heat flux ranges. Both density and viscosity of water are smaller than those of HFE-7200, resulting in lower pressure drop. The archived maximum exit vapor quality for water is also smaller than that for HFE-7200, which are 0.18 and 0.84, respectively, resulting in lower vapor phase acceleration pressure drop for water. The pressure drop can be modeled by summation of the pressure drops of single phase region and two phase region, and the two phase region pressure drop can be modeled using separated flow model, with Martinelli parameter, X, and two phase multiplier, ϕ_l^2. The Lockhart and Martinelli (viscous liquid, viscous vapor) correlation [50, 51], Lockhart and Martinelli (viscous liquid, turbulent vapor) correlation [50, 51], Qu and Mudawar correlation [52], Krishnamurthy and Peles correlation [53], and Reeser et al correlations [32] are examined for water data, and they are not able to predict current results satisfactorily. Therefore, a new correlation is developed which can predict current water data with a MAE of 4.1% and 4.5% for sparse and dense devices, respectively. For HFE-7200, the Lockhart and Martinelli (viscous liquid, viscous vapor) correlation, Lockhart and

Martinelli (viscous liquid, turbulent vapor) correlation, and the correlation developed for water in Chapter 3 can make acceptable predictions. A slight change in correlation developed or water can predict current HFE-7200 pressure drop data within $\pm 20\%$, with a MAE of 7.8%.

The effect of inlet fluid temperatures on pressure drop for HFE-7200 is not as noticeable as for water. Since the pressure drop of HFE-7200 is significantly higher than that of water, the effects of viscosity variation due to fluid temperature change are not noticeable.

The water experiment was conducted at reduced pressure to lower saturation temperature. The reservoir pressure was close to vacuum for all water tests. However, as heat flux and exit vapor quality increase, the pressure drop from device exit to reservoir increases, leading to increase in device outlet pressure. Eventually, the device outlet pressure is higher than atmospheric pressure. Ledinegg instability was observed, which is known to be a probem in low pressure system. Pressure, flow rate, and temperature oscillations are associated with Ledinegg instability. Single phase liquid and two phase flow alternatively occupy the microgap when Ledinegg instability occurs. Further increase in heat flux results in stable two phase flow. The HFE-7200 experiment was conducted with reservoir open to atmospheric, and no two phase flow instabilities were observed.

In application to electronics cooling, water is the better option when large heat flux needs to be removed due to its excellent thermodynamic properties, and the structural strength requirement for using water is also lower. However, boiling point of water is unacceptably high at atmospheric pressure, and reduced system pressure is necessary. Ledinegg instability accompanies with flow boiling of water at reduced pressure, which needs to be mitigated. A positive displacement pump is recommended. For moderate heat flux applications, HFE-7200 is the better

option, because it has a lower boiling point, and chemically inert. No instabilities have been observed for HFE-7200, which also makes it attractive. However, the pressure drop is relatively high for HFE-7200, requires stronger flow loop components to hold the pressure.

6.1.3 Flow Patterns

For water, unlike traditional two phase flow regimes in macro scale channels or in microchannels, no bubbly flow, slug flow or annular flow is seen in pin fin enhanced microgaps. Boiling occurs in an area close to microgap outlet at low heat flux, and moves towards microgap inlet, as heat flux increases. Inside the boiling area, liquid films are observed to surround pin fins. In sparse device at low heat flux, liquid film is uniformly attached to pin fins, and liquid films of adjacent pin fins are connected at certain locations. As heat flux increases, liquid film attached to each pin becomes separated. At high heat flux, liquid film is stretched to sharp-tail liquid wake. Bubble nucleates at rear side of pin fin inside liquid film/wake. In dense device, no sharp-tail liquid wake or bubble nucleation inside liquid wake is seen due to limited space between pin fins. At low heat flux, bubble nucleation at upstream of boiling area is observed. The nucleated bubbles travel and grow in transverse direction instead of moving downstream also due to limited space between pin fins. Similarly as in sparse device, liquid film is uniformly attached to pin fins, and liquid films of adjacent pin fins are connected at certain locations. As heat flux increases, liquid film attached to each pin becomes separated. At high heat flux, liquid films are offset to downstream cue to vapor phase acceleration. Instead of seeing a stretched liquid wake as in sparse device, the liquid film is thicker at rear side of pin fin than at front side. Dryout is observed at certain conditions. Liquid droplets from upstream are seen to pass the dryout region occasionally.

For HFE-7200, boiling area is at downstream side of pin fin array, and moves towards upstream as heat flux increases. At low heat flux, bubble nucleation is observed at upstream of boiling area, and liquid films are observed to surround pin fins, with sharp tail wakes, at downstream of boiling area. At increased heat flux, no bubble nucleation is seen in the entire boiling area due to increased pressure. The main flow pattern for HFE-7200 is liquid film surrounding pin fins with a sharp tail wake. No dryout is seen within the tested mass flux and heat flux ranges.

6.1.4 Effects of Heat Source Locations

Change of heating locations has an important effect on flow boiling of water. As heating location moves from inlet to outlet, flow boiling becomes more stable, pressure drop becomes smaller, and two phase heat transfer coefficient becomes higher. When heating at H3 and H4, the upstream pin fins perform as pressure restrictors and aid to suppress unstable oscillations, resulting in better performance when heating at H3 and H4. When designing pin fin enhanced microgap heatsink, extra rows of pin fins at upstream of heated section are recommended.

Two phase heat transfer coefficient also strongly depends on two phase flow patterns, similarly as when all four heaters are uniformly powered. The two phase heat transfer coefficient and pressure drop correlations developed in Chapter 3 are able to yield predictions with a MAE of 9.8% and 4.8%, respectively.

6.2 Recommendations on Future Work

Based on the findings in this work, a few recommendations on future work are as follows:

1. The heaters used in this work are platinum resistance heaters deposited directly on reverse side of heat sink. The heaters are also used for temperature measurement, known as resistance temperature detectors (RTDs). The platinum heaters induced a temperature limit of 130 °C. When heater temperature exceeds 130 °C, the heater resistance vs temperature calibration curve shifts, leading to inaccurate temperature measurement. Thus, tested heat flux range is limited to when heater temperature reaches 130 °C in this work. To study boiling at higher mass flux and heat flux, a robust heater or separate heater and temperature sensor are recommended. Critical heat flux has not been well studied as well, which also requires robust heaters.
2. The tested devices in this work have two pressure taps placed at upstream and downstream of staggered pin fin arrays, to measure inlet and outlet pressure. To better understand two phase pressure drop, multiple pressure taps placed at different locations between inlet and outlet along flow direction are recommended in future design of sample device.
3. The effects of pin fin configurations on flow boiling are not clear. There are many parameters in designing pin fin enhanced microgap heat sink, such as pin fin shape, pin fin height, transverse pitch, longitudinal pitch, and pin fin diameter. Two phase heat transfer coefficient, pressure drop, and flow patterns are all observed to be different for sparse and dense device. Thus, parametric study is necessary to better understand flow boiling in pin fin enhanced microgap.
4. Investigation of flow boiling in a plain microgap with the same gap size as a baseline case is recommended. This can assist to understand effects of pin fin and flow regimes, etc.

5. Liquid films are seen to attach to pin fins by means of high speed flow visualization. For flow boiling of water in sparse device, bubble nucleation at rear side of pin fin inside liquid film is observed. The lens used for flow visualization can only focus on a single depth level, and therefore the obtained images are 'depth averaged' and cannot capture all the details. To better understand bubble nucleation, bubble growth and interface tracking, numerical modeling is recommended. However, numerical modeling of two phase flow is very challenging and computationally expensive.
6. The current flow system is fairly large, occupying 1 m × 0.5 m × 0.5 m space, which is may not be suitable for electronics cooling, especially for portable electronics. Minimizing the system size is recommended for application in a real electronics cooling system.

REFERENCES

[1] Garimella, S. V., and Sobhan, C., 2003, "Transport in microchannels-a critical review," Annual review of heat transfer, 13(13).

[2] Thome, J. R., 2004, "Boiling in microchannels: a review of experiment and theory," International Journal of Heat and Fluid Flow, 25(2), pp. 128-139.

[3] Tibirica, C. B., and Ribatski, G., 2013, "Flow boiling in micro-scale channels–synthesized literature review," International Journal of Refrigeration, 36(2), pp. 301-324.

[4] Bar-Cohen, A., and Rahim, E., "Modeling and prediction of two-phase refrigerant flow regimes and heat transfer characteristics in microgap channels," Proc. ASME 2007 5th International Conference on Nanochannels, Microchannels, and Minichannels, American Society of Mechanical Engineers, pp. 1141-1160.

[5] Bar-Cohen, A., Sheehan, J. R., and Rahim, E., 2012, "Two-phase thermal transport in microgap channels—theory, experimental results, and predictive relations," Microgravity Science and Technology, 24(1), pp. 1-15.

[6] "Engineering Equation Solver Academic Professional Software, 2015 version."

[7] Tsai, W.-T., 2005, "Environmental risk assessment of hydrofluoroethers (HFEs)," Journal of hazardous materials, 119(1), pp. 69-78.

[8] Lee, H. J., and Lee, S. Y., 2001, "Heat transfer correlation for boiling flows in small rectangular horizontal channels with low aspect ratios," International Journal of Multiphase Flow, 27(12), pp. 2043-2062.

[9] Yang, Y., and Fujita, Y., "Flow boiling heat transfer and flow pattern in rectangular channel of mini-gap," Proc. Second International Conference on Microchannels and Minichannels (ICMM2004-2383), New York, USA.

[10] Koşar, A., and Peles, Y., 2006, "Convective flow of refrigerant (R-123) across a bank of micro pin fins," International Journal of Heat and Mass Transfer, 49(17), pp. 3142-3155.

[11] Koşar, A., and Peles, Y., 2007, "Boiling heat transfer in a hydrofoil-based micro pin fin heat sink," International Journal of Heat and Mass Transfer, 50(5–6), pp. 1018-1034.

[12] Lie, Y., Ke, J., Chang, W., Cheng, T., and Lin, T., 2007, "Saturated flow boiling heat transfer and associated bubble characteristics of FC-72 on a heated micro-pin-finned silicon chip," International Journal of Heat and Mass Transfer, 50(19), pp. 3862-3876.

[13] Krishnamurthy, S., and Peles, Y., 2008, "Flow boiling of water in a circular staggered micro-pin fin heat sink," International Journal of Heat and Mass Transfer, 51(5), pp. 1349-1364.

[14] Sheehan, J., Kim, D. W., and Bar-Cohen, A., "Thermal Imaging of Two-Phase Coooled Microgap Channel Wall," Proc. ASME 2009 InterPACK Conference collocated with the ASME 2009 Summer Heat Transfer Conference and the ASME 2009 3rd International Conference on Energy Sustainability, American Society of Mechanical Engineers, pp. 491-499.

[15] Qu, W., and Siu-Ho, A., 2009, "Experimental study of saturated flow boiling heat transfer in an array of staggered micro-pin-fins," International Journal of Heat and Mass Transfer, 52(7–8), pp. 1853-1863.

[16] Ma, A., Wei, J., Yuan, M., and Fang, J., 2009, "Enhanced flow boiling heat transfer of FC-72 on micro-pin-finned surfaces," International Journal of Heat and Mass Transfer, 52(13), pp. 2925-2931.

[17] Yuan, M., Wei, J., Xue, Y., and Fang, J., 2009, "Subcooled flow boiling heat transfer of FC-72 from silicon chips fabricated with micro-pin-fins," International Journal of Thermal Sciences, 48(7), pp. 1416-1422.

[18] Dae-Whan, K., Rahim, E., Bar-Cohen, A., and Han, B., 2010, "Direct Submount Cooling of High-Power LEDs," Components and Packaging Technologies, IEEE Transactions on, 33(4), pp. 698-712.

[19] Kim, D. W., Rahim, E., Bar-Cohen, A., and Han, B., "Thermofluid characteristics of two-phase flow in micro-gap channels," Proc. Thermal and Thermomechanical Phenomena in Electronic Systems, 2008. ITHERM 2008. 11th Intersociety Conference on, IEEE, pp. 979-992.

[20] Sheehan, J., and Bar-Cohen, A., "Spatial and temporal wall temperature fluctuations in two-phase flow in microgap coolers," Proc. ASME 2010 International Mechanical Engineering Congress and Exposition, American Society of Mechanical Engineers, pp. 1701-1708.

[21] Alam, T., Lee, P. S., Yap, C. R., and Jin, L., "Experimental investigation of microgap cooling technology for minimizing temperature gradient and mitigating hotspots in electronic devices," Proc. Electronics Packaging Technology Conference (EPTC), 2011 IEEE 13th, IEEE, pp. 530-535.

[22] Morshed, A. K. M. M., Yang, F., Yakut Ali, M., Khan, J. A., and Li, C., 2012, "Enhanced flow boiling in a microchannel with integration of nanowires," Applied Thermal Engineering, 32, pp. 68-75.

[23] Guo, D., Wei, J., and Zhang, Y., 2011, "Enhanced flow boiling heat transfer with jet impingement on micro-pin-finned surfaces," Applied Thermal Engineering, 31(11), pp. 2042-2051.

[24] Alam, T., Lee, P. S., Yap, C. R., and Jin, L., 2012, "Experimental investigation of local flow boiling heat transfer and pressure drop characteristics in microgap channel," International Journal of Multiphase Flow, 42, pp. 164-174.

[25] Alam, T., Lee, P. S., Yap, C. R., Jin, L., and Balasubramanian, K., 2012, "Experimental investigation and flow visualization to determine the optimum dimension range of microgap heat sinks," International Journal of Heat and Mass Transfer, 55(25), pp. 7623-7634.

[26] Morshed, A., Paul, T. C., and Khan, J. A., "Effect of cross groove on flow boiling in a microgap," Proc. ASME 2012 Heat Transfer Summer Conference collocated with the ASME 2012 Fluids Engineering Division Summer Meeting and the ASME 2012 10th International Conference on Nanochannels, Microchannels, and Minichannels, American Society of Mechanical Engineers, pp. 457-463.

[27] Isaacs, S. A., Joshi, Y., Zhang, Y., Bakir, M. S., and Kim, Y. J., "Two-Phase Flow and Heat Transfer in Pin-Fin Enhanced Micro-Gaps With Non-Uniform Heating," Proc. ASME 2013 4th International Conference on Micro/Nanoscale Heat and Mass Transfer, American Society of Mechanical Engineers, pp. V001T012A003-V001T012A003.

[28] Isaacs, S., Kim, Y. J., McNamara, A. J., Joshi, Y., Zhang, Y., and Bakir, M. S., "Two-phase flow and heat transfer in pin-fin enhanced micro-gaps," Proc. Thermal and Thermomechanical Phenomena in Electronic Systems (ITherm), 2012 13th IEEE Intersociety Conference on, IEEE, pp. 1084-1089.

[29] Alam, T., Lee, P. S., and Yap, C. R., 2013, "Effects of surface roughness on flow boiling in silicon microgap heat sinks," International Journal of Heat and Mass Transfer, 64, pp. 28-41.

[30] Alam, T., Lee, P. S., Yap, C. R., and Jin, L., 2013, "A comparative study of flow boiling heat transfer and pressure drop characteristics in microgap and microchannel heat sink and an evaluation of microgap heat sink for hotspot mitigation," International Journal of Heat and Mass Transfer, 58(1), pp. 335-347.

[31] Dai, X., Yang, F., Fang, R., Yemame, T., Khan, J. A., and Li, C., 2013, "Enhanced single- and two-phase transport phenomena using flow separation in a microgap with copper woven mesh coatings," Applied Thermal Engineering, 54(1), pp. 281-288.

[32] Reeser, A., Bar-Cohen, A., and Hetsroni, G., 2014, "High quality flow boiling heat transfer and pressure drop in microgap pin fin arrays," International Journal of Heat and Mass Transfer, 78(0), pp. 974-985.

[33] David, T., Mendler, D., Mosyak, A., Bar-Cohen, A., and Hetsroni, G., 2014, "Thermal Management of Time-Varying High Heat Flux Electronic Devices," Journal of Electronic Packaging, 136(2), pp. 021003-021003.

[34] Ong, C. L., Paredes, S., Sridhar, A., Michel, B., and Brunschwiler, T., "Radial hierarchical microfluidic evaporative cooling for 3-d integrated microprocessors," Proc. Proc. 4th European Conference on Microfluidics, Limerick.

[35] Schultz, M., Yang, F., Colgan, E., Polastre, R., Dang, B., Tsang, C., Gaynes, M., Parida, P., Knickerbocker, J., and Chainer, T., "Embedded Two-Phase Cooling of Large 3D Compatible Chips with Radial Channels," Proc. ASME 2015 International Technical Conference and Exhibition on Packaging and Integration of Electronic and Photonic Microsystems collocated with the ASME 2015 13th International Conference on Nanochannels, Microchannels, and Minichannels, American Society of Mechanical Engineers, pp. V003T010A007-V003T010A007.

[36] Yang, F., Schultz, M., Parida, P., Colgan, E., Polastre, R., Dang, B., Tsang, C., Gaynes, M., Knickerbocker, J., and Chainer, T., "Local Measurements of Flow Boiling Heat Transfer on Hot Spots in 3D Compatible Radial Microchannels," Proc. ASME 2015 International Technical Conference and Exhibition on Packaging and Integration of Electronic and Photonic Microsystems collocated with the ASME 2015 13th International Conference on Nanochannels, Microchannels, and Minichannels, American Society of Mechanical Engineers, pp. V003T010A006-V003T010A006.

[37] Tamanna, A., and Lee, P. S., 2015, "Flow boiling heat transfer and pressure drop characteristics in expanding silicon microgap heat sink," International Journal of Heat and Mass Transfer, 82, pp. 1-15.

[38] Tamanna, A., and Lee, P. S., "Investigation of flow boiling characteristics in expanding silicon microgap heat sink," Proc. Thermal and Thermomechanical Phenomena in Electronic Systems (ITherm), 2014 IEEE Intersociety Conference on, IEEE, pp. 458-465.

[39] Woodcock, C., Yu, X., Plawsky, J., and Peles, Y., 2015, "Piranha Pin Fin (PPF)—Advanced flow boiling microstructures with low surface tension dielectric fluids," International Journal of Heat and Mass Transfer, 90, pp. 591-604.

[40] Lee, H. J., and Lee, S. Y., 2001, "Pressure drop correlations for two-phase flow within horizontal rectangular channels with small heights," International Journal of Multiphase Flow, 27(5), pp. 783-796.

[41] Dae Whan, K., Bar-Cohen, A., Rahim, E., and Han, B., "Thermofluid characteristics of two-phase flow in microgap channels," Proc. Proc. IEEE ITHERM Conference.

[42] Chen, J. C., 1966, "Correlation for boiling heat transfer to saturated fluids in convective flow," Industrial & Engineering Chemistry Process Design and Development, 5(3), pp. 322-329.

[43] Shah, M., 1982, "Chart correlation for saturated boiling heat transfer: equations and further study," ASHRAE Trans.;(United States), 88(CONF-820112-).

[44] Kawahara, A., Chung, P.-Y., and Kawaji, M., 2002, "Investigation of two-phase flow pattern, void fraction and pressure drop in a microchannel," International Journal of Multiphase Flow, 28(9), pp. 1411-1435.

[45] Qu, W., and Siu-Ho, A., 2009, "Measurement and prediction of pressure drop in a two-phase micro-pin-fin heat sink," International Journal of Heat and Mass Transfer, 52(21–22), pp. 5173-5184.

[46] Kline, S. J., and McClintock, F., 1953, "Describing uncertainties in single-sample experiments," Mechanical engineering, 75(1), pp. 3-8.

[47] Steinke, M. E., and Kandlikar, S. G., 2004, "Control and effect of dissolved air in water during flow boiling in microchannels," International Journal of Heat and Mass Transfer, 47(8–9), pp. 1925-1935.

[48] Carey, V. P., Liquid-Vapor Phase-Change Phenomena, Taylor & Francis Group.

[49] Chisholm, D., and Laird, A., 1958, "Two-phase flow in rough tubes," Trans. ASME, 80(2), pp. 276-286.

[50] Lockhart, R., and Martinelli, R., 1949, "Proposed correlation of data for isothermal two-phase, two-component flow in pipes," Chem. Eng. Prog, 45(1), pp. 39-48.

[51] Chisholm, D., 1983, Two-phase flow in pipelines and heat exchangers, George Godwin London.

[52] Qu, W., and Mudawar, I., 2003, "Measurement and prediction of pressure drop in two-phase micro-channel heat sinks," International Journal of Heat and Mass Transfer, 46(15), pp. 2737-2753.

[53] Krishnamurthy, S., and Peles, Y., 2007, "Gas-liquid two-phase flow across a bank of micropillars," Physics of Fluids (1994-present), 19(4), p. 043302.

[54] Ledinegg, M., 1938, "Instability of flow during natural and forced circulation," Die Warme, 61(8), pp. 891-898.

[55] Tadrist, L., 2007, "Review on two-phase flow instabilities in narrow spaces," International Journal of Heat and Fluid Flow, 28(1), pp. 54-62.

[56] Ruspini, L. C., Marcel, C. P., and Clausse, A., 2014, "Two-phase flow instabilities: a review," International Journal of Heat and Mass Transfer, 71, pp. 521-548.

[57] Zhang, T., Tong, T., Chang, J.-Y., Peles, Y., Prasher, R., Jensen, M. K., Wen, J. T., and Phelan, P., 2009, "Ledinegg instability in microchannels," International Journal of Heat and Mass Transfer, 52(25–26), pp. 5661-5674.

[58] Kuo, C.-J., and Peles, Y., 2009, "Pressure effects on flow boiling instabilities in parallel microchannels," International Journal of Heat and Mass Transfer, 52(1), pp. 271-280.